5-2015

Parameterized Least-Squares Attitude History Estimation and Magnetic Field Observations of the Auroral Spatial Structures Probe

Ryan J. Martineau
Utah State University

PARAMETERIZED LEAST-SQUARES ATTITUDE HISTORY ESTIMATION AND MAGNETIC FIELD OBSERVATIONS OF THE AURORAL SPATIAL STRUCTURES PROBE

by

Ryan J. Martineau

A thesis submitted in partial fulfillment
of the requirements for the degree

of

MASTER OF SCIENCE

in

Mechanical Engineering

Approved:

Dr. Heng Ban Major Professor	Dr. Charles M. Swenson Committee Member
Dr. Rees R. Fullmer Committee Member	Dr. Mark R. McLellan Vice President for Research and Dean of the School of Graduate Studies

UTAH STATE UNIVERSITY
Logan, Utah

2015

Abstract

Parameterized Least-Squares Attitude History Estimation and Magnetic Field Observations of the Auroral Spatial Structures Probe

by

Ryan J. Martineau, Master of Science

Utah State University, 2015

Major Professor: Dr. Heng Ban
Department: Mechanical and Aerospace Engineering

Terrestrial auroras are visible-light events caused by charged particles trapped by the Earth's magnetic field precipitating into the atmosphere along magnetic field lines near the poles. Auroral events are very dynamic, changing rapidly in time and across large spatial scales. Better knowledge of the flow of energy during an aurora will improve understanding of the heating processes in the atmosphere during geomagnetic and solar storms.

The Auroral Spatial Structures Probe is a sounding rocket campaign to observe the middle-atmosphere plasma and electromagnetic environment during an auroral event with multipoint simultaneous measurements for fine temporal and spatial resolution. The auroral event in question occurred on January 28, 2015, with liftoff of the rocket at 10:41:01 UTC. The goal of this thesis is to produce clear observations of the magnetic field that may be used to model the current systems of the auroral event. To achieve this, the attitude of ASSP's 7 independent payloads must be estimated, and a new attitude determination method is attempted. The new solution uses nonlinear least-squares parameter estimation with a rigid-body dynamics simulation to determine attitude with an estimated accuracy of a few degrees. Observed magnetic field perturbations found using the new attitude solution are

presented, where structures of the perturbations are consistent with previous observations and electromagnetic theory.

(126 pages)

Public Abstract

Parameterized Least-Squares Attitude History Estimation and Magnetic Field Observations of the Auroral Spatial Structures Probe

by

Ryan J. Martineau, Master of Science

Utah State University, 2015

Major Professor: Dr. Heng Ban
Department: Mechanical and Aerospace Engineering

As charged particles from the Sun enter the Earth's atmosphere and create the aurora borealis (Northern lights) and aurora australis (Southern lights), energy is transferred to the atmosphere. In order to better understand the energy transfer processes, the Auroral Spatial Structures Probe rocket was launched to make measurements in the active aurora. Several payloads were deployed by the rocket, each with sensors to measure the magnetic field and the electric field so that the way they change over time and in different positions could be observed. The measurements require accurate knowledge of the spacecraft orientation, and to that end this thesis discusses the way in which the orientation was estimated. Using the magnetic and electric field measurements and comparing these to predictions made by mathematical models of the fields, a good estimate was obtained for some of the payloads. The result of this is a good measurement of the magnetic and electric fields that may be used to achieve the scientific goals of the mission.

Acknowledgments

The Auroral Spatial Structures Probe was funded by NASA award number NNX11AE23G. This work was funded by NASA award number NNX13AN20A.

Though it is my only experience in graduate school, I consider it rare and wonderful to have access to such wonderful teachers and mentors. I thank Dr. Heng Ban, my major professor, for playing a part in my decision to attend graduate school, and for his advice and encouragement on many occasions. Thanks also go to Dr. Charles Swenson for the opportunity to work on this project, and for consulting me on the details.

There are many individuals, too many to name, who have helped to spark my passion for research. Among them are teachers, project team members, space camp leaders, roommates, and friends. From these, I would like to acknowledge Chad Fish for his role in making me a part of this project, and giving me research challenges on several projects from our first meeting two years ago. The result of many interactions with these people over the years is not only this thesis, but a bright future doing what I love.

I thank the entire Auroral Spatial Structures Probe team who made it a success, many of whom have also answered my questions and helped to make my work better. Specific individuals who contributed supporting information directly related to this work include Patrick Mortola, Christopher Smith, Crystal Frazier, and Tim Neilsen.

Thanks to John Pratt for giving me a leg up several times in the course of this work.

A personal thanks to Troy Munro for his never-ending support in all of these things, and being the best peer mentor anyone could ever ask for, though I didn't even have to ask.

I thank my family, for being wonderful and helpful and supportive.

I thank my darling wife Nicole for not only enduring my ramblings, but truly seeking to understand my work and share in the excitement with me.

Finally, I thank God for tutoring and aid on this and all subjects, and for showing me what I can be.

Contents

List of Tables

List of Figures

Notation

Accents

$\vec{x}$ vector

$\hat{x}$ unit vector

$\tilde{x}$ estimate

$\dot{x}$ time derivative

Symbols

R_a^b rotation matrix from frame a to frame b

$\vec{B}$ magnetic field

$\vec{E}$ electric field

ϕ first Euler angle in 3-2-1 sequence

θ second Euler angle in 3-2-1 sequence

ψ third Euler angle in 3-2-1 sequence

$\vec{\omega}_a^b$ angular rate vector of frame a with respect to frame b

λ longitude

ϕ latitude, when appearing with λ

q quaternion

Coordinate Frames

b or body payload body frame

fg fluxgate magnetometer measurement frame

ENU local East-North-Up reference frame

NED local North-East-Down reference frame

ECEF Earth-Centered Earth-Fixed reference frame

ECI Earth-Centered Inertial reference frame

Chapter 1

Introduction

1.1 Topic Introduction

Energy transfer in Earth's upper atmosphere during auroral events is not completely understood, due to the difficulty of obtaining the necessary multi-point, in situ magnetic and electric field measurements required to map components of the energy transfer. Several sounding rocket missions such as 14.321 UE in 1969 [1], 18.112 UE in 1975 [2], and 29.007 UE in 1978 [3] have used magnetometers to observe the spatial structures of auroral currents, but the temporal and spatial resolution has been insufficient to completely understand the structures present in the extremely dynamic environment that is the aurora. The Auroral Spatial Structures Probe (ASSP) is a sounding rocket campaign to make in-situ magnetic and electric measurements in the aurora borealis with greater temporal and spatial resolution than previous missions, with the ultimate goal of understanding the energy flow by observing auroral currents and associated Joule heating. The mission consists of a total of seven rocket payloads: six deployable subpayloads and a larger main payload that controls the deployment. The payloads were deployed in such a way that multiple payloads passed through very nearly the same point at different times, allowing the temporal and spatial structures to be discerned from one another. Figure 1.3 shows the slightly different flight paths of the payloads. Each payload had a science sensor suite that included a magnetoresistive science magnetometer, electric field probes, and a Langmuir probe (figures 1.1 and 1.2). The main payload also had additional plasma probes and a fluxgate magnetometer.

ASSP's goal to observe detailed auroral plasma and electromagnetic structures requires an attitude solution for the observation segment of the flight, so that the observations can be rotated from the spacecraft body coordinate system into a more meaningful reference coordinate system. An attitude solution can be obtained in two ways: by inertial sensors

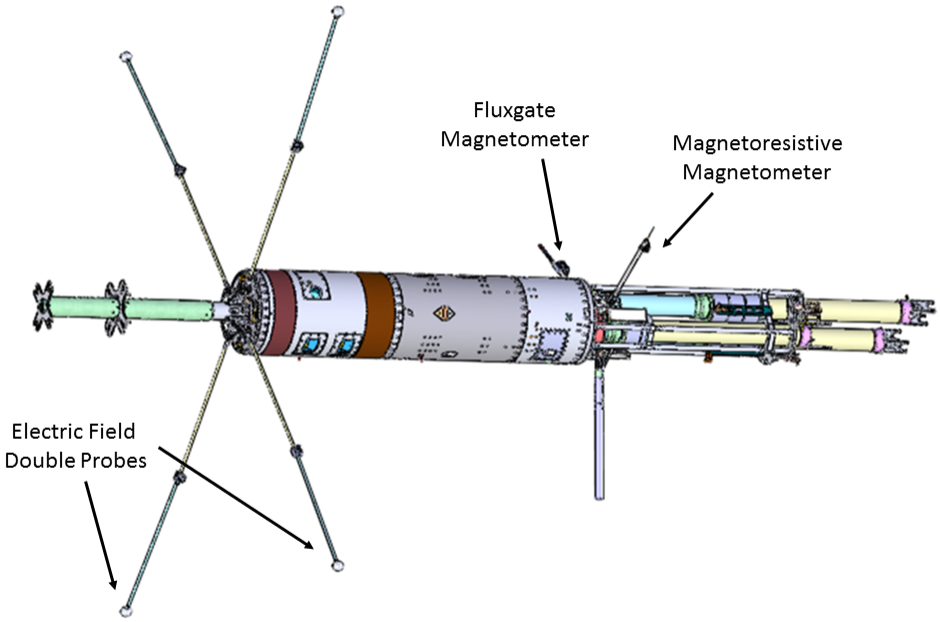

Fig. 1.1: ASSP main payload science instrumentation

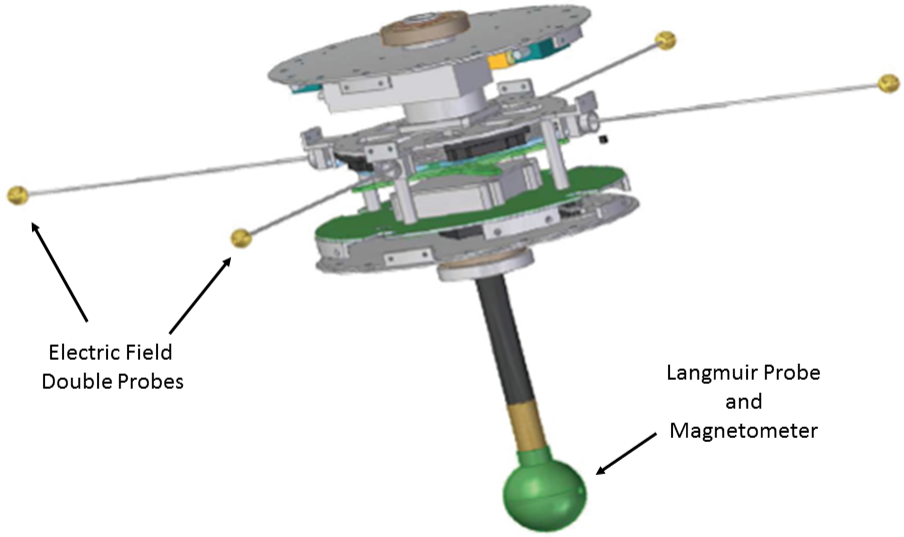

Fig. 1.2: ASSP subpayload science instrumentation

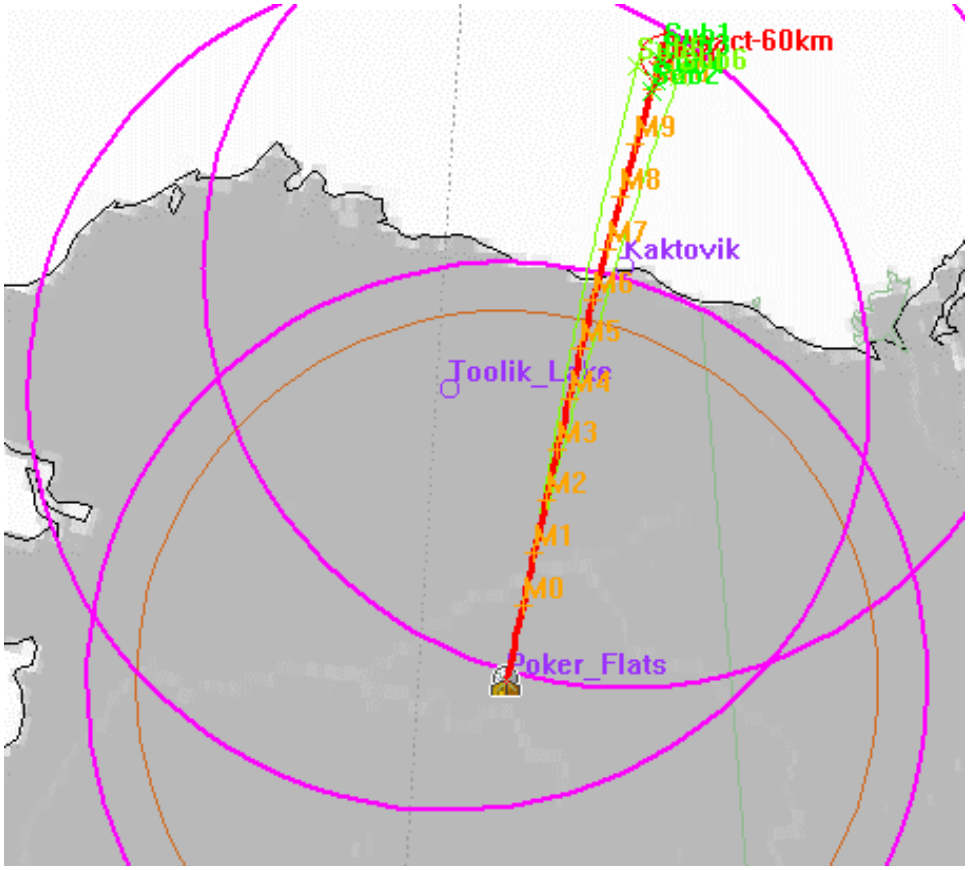

Fig. 1.3: ASSP flight paths

or by absolute vector measurements. Inertial sensors measure attitude relative to an initial, known attitude by integrating angular rate information from the gyroscopes to obtain angular position knowledge. An absolute attitude solution with respect to a general reference frame (as opposed to an earlier, known attitude) requires at least two independent vector measurements. Each subpayload was equipped with 3-axis gyroscopes, intended to provide a post-processed, inertial attitude solution. However, the spin-axis gyro on each of the subpayloads became saturated before the subpayload deployment, rendering inertial attitude estimation impossible with these sensors. As a result, an alternate attitude solution must be sought. Because two of the scientific sensors provide vector observations, these can be used to obtain an absolute estimate of the spacecraft attitude. Since the science measurements will be used to obtain the attitude solution, and the attitude solution subsequently used to meet the science goals, this is known as a "bootstrap" solution. No work was done preflight to develop estimation filters or algorithms utilizing the science vector measurements, and so a post-flight least-squares batch estimation method was conceived to be the most advantageous method under the circumstances. This approach would allow all of the vector measurements to be simultaneously considered in the estimation, thereby increasing accuracy, but the estimator is simpler to build and test than a Kalman Filter, albeit at the expense of computational efficiency.

The focus of this thesis is on the magnetometer observations of all payloads and their simultaneous measurements, for the purpose of making inferences about the structure of the auroral current system. Therefore, a large part of this work must necessarily focus on the attitude estimation of the payloads. The magnetometer and electric field probe data will be used to obtain the attitude history estimate. This work will be a small part of a significant effort to process the ASSP data. Additional tasks can be found in section 7.1.

1.2 Outcome and Significance

As stated in section 1.1, ASSP is far from the first sounding rocket attempt to detect the spatial structure of an auroral current system. However, by making multi-point simultaneous measurements, it is anticipated that ASSP's contributions to the understanding of these

structures will be greatly improved over other missions. First, by flying several payloads alongside one another, each set of observations can be used independently to determine current structures as has been done in the past [1] [3] [4]. These independent determinations may corroborate each other for an unprecedented level of certainty. Additionally, using the simultaneous measurements to observe the larger-scale magnetic vector field, the currents may be found by the curl of that field. This is a completely independent procedure which will verify the findings of using standalone methods. Improved understanding of the auroral system will lead to improved understanding of energy transfer mechanisms in Earth's atmosphere, advancing the science of terrestrial and upper-atmospheric weather and its dependence on solar activity. Both stated approaches to determining the current structures in the aurora depend on having accurate magnetic field observations in a useful frame, which is the goal of this thesis (see Chapter 3 for specific objectives).

Transforming the magnetometer measurements into a useful coordinate frame requires attitude knowledge. It was intended to obtain this by integrating inertial angular rate measurements, but the sensors on board the spacecraft failed. Using the two vector measurements made by each of the payloads using the science instruments, namely the magnetometers and electric field probes, a relatively simple-to-construct attitude estimation method can be developed. If successful, this method may be extended to other missions where inertial sensors fail, or potentially could introduce a new class of post-processed attitude solutions with advantages over traditional methods. Namely, unlike inertial attitude determination, initial conditions need not be precisely known. Also, a physical model, which would be required for the new method, may be as detailed as desired while still not requiring the measurement geometry information needed to build a Kalman Filter. The likelihood of this method becoming more generalized and applied to other missions is dependent on its specific mathematical properties, which are beyond the scope of this thesis to define.

It is anticipated that by using the new attitude estimation procedure, the magnetic field observations may be transformed to a useful frame with reasonable accuracy, allowing them to be further processed and used to make the desired inferences about the auroral

current system.

Chapter 2

Auroral Science and Attitude Determination Background

2.1 Auroral Electrodynamics

The visible aurora is caused by energetic charged particles (electrons and ions) originating from the sun trapped in the Earth's magnetic field precipitating into the atmosphere along magnetic field lines. As these particles enter the atmosphere, they collide with neutral particles, causing the neutral particles to emit photons and thus producing the bright lights of the aurora. This phenomenon is of interest because it can yield insight into the more complex dynamics of energy transfer from the Sun to the Earth. The movement of charged particles necessarily creates an electrical current, and since the aurora is an energetic event caused by the motion of charged particles, there are strong currents associated with the events, directed along the magnetic field lines. These field-aligned currents are known as Birkeland currents. Electrical currents induce magnetic fields perpendicular to the current by the right-hand rule, so these currents may be detected by measuring the magnetic field in the same region. It is for this reason that each ASSP payload was equipped with a vector magnetometer.

The scientific goals of the ASSP rocket campaign will require significant time and effort to achieve. The measurements and dynamics of the payloads are complex, and detailed scientific inferences about the auroral electrodynamic systems are beyond the scope of this thesis. It is the goal of this thesis, however, to show that some useful observations of the auroral current system can be made with the reduced magnetometer observations resolved by the methods described. To that end, we review literature on auroral electrodynamics from previous campaigns.

One of the earliest rocket campaigns that probed the aurora with a vector magnetometer was Park and Cloutier [1]. The authors used a biased scalar magnetometer, utilizing the spin of the rocket to effectively create a vector instrument. Using lunar aspect data, they first determined the portion of the flight over which the mechanical motion of the rocket was at steady-state, then found the rotation rate of the rocket body and the precession rate of the rotation axis, which were necessary to determine the direction of the magnetic field from the biased magnetometer observations. The authors took great effort to describe in detail the motion of the rocket, and how its spin and coning (rotation and precession) modulated the signal of the biased magnetometer. By determining these modulations, they were able to remove the effects of the mechanical motion from the measurements. This is a critical step in the data reduction, and this example highlights the importance of attitude determination for ASSP. The difference magnetic field $\Delta\vec{B}$ was found by subtracting a spherical harmonic expansion model of the Earth's magnetic field from the magnetometer measurements. By finding the best fit to the difference field data for models of Birkeland current sheets and horizontal electrojet currents, they were able to determine the existence of the sheets and their horizontal position relative to the launch site, as well as the magnitude of the auroral electrojet current.

Another experiment by Robinson et al. [3] used simultaneous ground-based radar and rocket-borne magnetometer measurements to observe current systems, aided by electric field sensors on the rocket. The equation used to find the cross-sectional current $J_\perp$ using electric field $\vec{E}$, magnetic field $\vec{B}$, neutral wind $\vec{U}$, and Pederson and Hall conductivities σ_P and σ_H, respectively over altitudes z_1 and z_2 is

$$\vec{J}_\perp = \int_{z_1}^{z_2} \sigma_P \mathrm{d}z (\vec{E} + \vec{U} \times \vec{B})_\perp + \int_{z_1}^{z_2} \sigma_H \mathrm{d}z \left(\frac{(\vec{E} + \vec{U} \times \vec{B})_\perp \times \vec{B}}{B} \right), \tag{2.1}$$

by which the importance of the magnetic field measurements in the determination of current structures can be seen. Also presented is a relationship between current intensity and the

rate of change of the azimuth angle ϕ_c of the magnetic field:

$$j_{\parallel} = k\frac{\Delta\phi_c}{\Delta t}\frac{\cos\beta}{\sin(\beta + I)}, \tag{2.2}$$

where I is the dip angle of the magnetic field and β is the angle between the velocity vector of the payload and the horizontal. The parameter k is a constant defined as

$$k = \frac{1}{\mu_0}\frac{B\cos(I - \alpha_c)}{v_H} \tag{2.3}$$

where μ_0 is the vacuum permeability, α_c is the angle between $\vec{B}$ and the mean spin axis of the payload, and v_H is the horizontal velocity of the payload. Without accurate knowledge of the attitude, the direction of the magnetic field and thus the nature of the current systems become very difficult to resolve. The authors used a star sensor for an accurate spin rate measurement. The magnetometer contained spin information as well, but Robinson noted in [5] that changes in the azimuth angle of the ambient magnetic field can be found in the differences between the measured spin rate of the magnetometer and the independent spin measurements by the star sensor. This shows the importance of attitude determination, and also some of the failings of bootstrap attitude estimation procedures. As with [1], $\Delta\vec{B}$ was found by subtracting a model field from the measured magnetic field vector. Currents measured by the electric field probes had fair agreement with those inferred by the magnetometers.

A multi-point measurement campaign similar to ASSP was performed in 2003 by Zheng et al. [4] Four free-flying magnetometers were ejected from a main payload. The magnetic difference field was found by digitally filtering the lowest frequencies representing the ambient field and the trajectory of the payloads. Current densities were calculated for each of the payloads treating the measurements as single-point measurements, and comparing these to a calculation of the curl of the difference field. Significant differences were found between the two calculations. Importantly for this thesis, Zheng et al. found attitude with an approach similar to that of [1], by using the magnetic field data to determine the rotation

and precession parameters to fit models and despin the measurements.

These few examples show how the desired measurements of electrical currents can be made using vector magnetometer observations. Each one also emphasizes the importance of attitude determination to resolve the direction of the magnetic field.

2.2 Attitude Determination

2.2.1 TRIAD Method

As mentioned in the previous section, attitude determination is critical for making sound observations of auroral current systems using rocket-borne magnetometers. The attitude estimation of the ASSP payloads as an integral part of the data reduction is a major point of this thesis. Attitude determination of satellites has been actively studied since the 1960s, when space launch capabilities first became significant and digital computers had developed enough for sophisticated estimation algorithms. One of the earliest and simplest general attitude solutions was developed by Black [6], and is now called the TRIAD algorithm. This method requires two independent vector measurements in both the body coordinate frame and the inertial frame and uses simple linear algebra to solve for the rotation matrix that represents the attitude. Given the column vectors $\vec{m}_1, \vec{m}_2$, representing sensor observations measured in the body frame, and the corresponding reference frame vectors $\vec{M}_1, \vec{M}_2$, where the two vector sets are ideally related by

$$\vec{M}_i = R\vec{m}_i, \tag{2.4}$$

we form the unit vectors

$$\hat{a} = \frac{\vec{m}_1}{|\vec{m}_1|}, \tag{2.5}$$

$$\hat{A} = \frac{\vec{M}_1}{|\vec{M}_1|}, \tag{2.6}$$

$$\hat{b} = \frac{\vec{m}_1 \times \vec{m}_2}{|\vec{m}_1 \times \vec{m}_2|}, \tag{2.7}$$

and

$$\hat{B} = \frac{\vec{M}_1 \times \vec{M}_2}{|\vec{M}_1 \times \vec{M}_2|}. \tag{2.8}$$

Then, we arrange the unit vectors into the following matrix equation:

$$\left[\hat{A} \quad \hat{B} \quad \hat{A} \times \hat{B}\right] = R \left[\hat{a} \quad \hat{b} \quad \hat{a} \times \hat{b}\right], \tag{2.9}$$

to which an estimate of the solution, and thus the spacecraft attitude, is

$$\tilde{R} = \left[\hat{A} \quad \hat{B} \quad \hat{A} \times \hat{B}\right] \left[\hat{a} \quad \hat{b} \quad \hat{a} \times \hat{b}\right]^T. \tag{2.10}$$

This method was once common on spacecraft, and is computationally inexpensive, though not necessarily an optimal solution. In [7], Markley discusses special cases in which the TRIAD method does produce the optimal solution. These cases include when the angles between the two measured vectors are the same in both coordinate frames, when the two vector observations are weighted equally, and when one vector observation is weighted much less than the other. These are important notes for ASSP, since at the time of this writing the magnetometer observations are better known than the electric field observations.

2.2.2 Wahba's Problem and Solutions

An early generalization of the attitude determination problem was by Grace Wahba in 1965 and is called Wahba's problem [8]. Wahba's problem seeks to minimize the function

$$\sum_{j=1}^{N} ||v_{j,b} - Rv_{j,I}||^2, \tag{2.11}$$

by finding R, which must be orthogonal and have $\det(R) = 1$, given measurements of some vectors v_j, $N \geq 2$ in an inertial coordinate frame I and simultaneously in the body frame b. Many solutions have been developed, focusing on optimality, robustness, and computational efficiency. Markley derived a singular value decomposition (SVD) method that produces a unique solution, as well as statistical information about the estimated attitude [9]. He

later implemented a computationally faster solution by determining the optimal attitude matrix via scalar parameters without expensive matrix decompositions [7]. In the later article [7], both of these methods are compared to each other and the quaternion-based QUEST algorithm for accuracy for several different test cases. The SVD method produced the lowest errors and greatest stability, but was the slowest algorithm tested. The major advantages of these methods over the simpler TRIAD algorithm are optimality and the ability to incorporate any number of simultaneous vector observations greater than the minimum of 2.

Wahba's problem has also been solved using attitude quaternions in place of an attitude matrix. According to Keat [10], Davenport derived a least-squares method to determine the attitude quaternion given a batch of simultaneous vector measurements, known as the q-method. This method has spawned derivatives, such as QUEST [11] and REQUEST [12]. All of these methods, while important to note, are based on reducing an attitude solution from more than two vector observations. Since ASSP has only two observations available on each payload, there is little advantage in discussing these methods in-depth. Additionally, they determine attitude via an intermediate quaternion, which has no practical advantage in the case of ASSP over a matrix method, since computational efficiency is not a concern.

Kalman filters are seen as the de facto standard attitude determination methods because they can be implemented in real-time, which is necessary for attitude control of spacecraft, and because they provide an optimal causal solution to Wahba's problem. The Kalman filter consists of a prediction step, where a physics model is used to predict a coming measurement from an attitude sensor. An update step follows which incorporates an actual measurement from the sensor. Choukroun [13] discusses Kalman filters in detail and presents novel implementations for attitude determination. Besides the fact that it can be employed in real-time, the Kalman filter is also advantageous because it allows for measurements from any number of sensors, it is robust to noisy measurements, and indeed uses the characteristics of measurement noise to improve the estimate. By doing so it provides an optimal estimate of the attitude at each moment in time. Some of these advantages are un-

fortunately not applicable to ASSP. Firstly, there are only two observing sensors, which are the minimum required for any absolute attitude determination, and thus the Kalman filter, which can take advantage of many measurements, will be wasted in this way. Secondly, the mission has flown and there is no need for a causal solution: non-causal data may be added for an improved estimation. For these reasons, a new technique will be attempted in place of a Kalman filter to estimate the attitude history for ASSP. Further discussion of the new technique and its potential advantages over a Kalman filter is had in section 4.4.

Chapter 3

Objectives

The goal of this work is to provide suitable observations of the magnetic field in a useful coordinate frame that may be used to infer current systems in the aurora. This goal will be achieved through the following objectives:

1. Develop a post-processed attitude estimation using the measurements made by the ASSP payloads
2. Determine the validity and accuracy of the attitude solution by comparison to alternate solutions and models of the magnetic field
3. Find the perturbations in the magnetic field in a useful reference frame that may correspond to passage through the aurora by filtering the high and low frequencies.
4. Compare the structures of the magnetic perturbations to previous measurement campaigns.

Chapter 4
Measurement Processing and Attitude Determination Methods

In order to observe magnetic field perturbations due to the auroral arc, an attitude solution must be obtained to resolve the measurements in an inertial coordinate frame. ASSP was equipped with rate gyros to obtain angular rate information throughout the flight, which would be integrated post-flight to determine the attitude history. However, it was discovered shortly after the flight that the gyros saturated in the spin axis, rendering them useless. An adequate attitude solution may still be obtained, however, since each payload was equipped with two vector instruments measuring independent quantities: the vector magnetometer and the electric field double-probes. The electric field probes only measure two components of the electric field vector, those that correspond to the body-x and body-y coordinates, which will affect the stability and accuracy of attitude determination methods.

4.1 Instrument Calibration

4.1.1 Magnetometer

A least-squares calibration was applied to the raw magnetometer data, calculating an optimal scale factor and bias for each vector component with the objective function being the difference between the magnitude of the in-flight measurements and calibration measurements made before the flight. This produced a good first estimate, though additional systematic error sources were identified, most importantly additional biases. As the spacecraft spins, the x- and y-axis magnetometer measurements should have means near zero, neglecting perturbations in the magnetic field which would not significantly shift the mean,

and corrected by adjusting the bias so that the mean was close to zero. This does not account for additional z-bias, so the bias term for this axis was adjusted to approximately match the magnitude of the z-axis component of the magnetic field measured by the flux-gate magnetometer on the main payload, which is a more trusted sensor with a better stock calibration. The magnitude of the z-component will change throughout the flight dependent on the individual payload since the spatial separation of the payloads is significant, so this adjustment is only approximate. An improved calibration may become available in the future, in which case it will be used in the attitude solution in lieu of the calibration described. The magnetic field data are filtered for high-frequency measurement noise using a zero-phase digital filter.

4.1.2 Electric Field Probes

Prior to the January flight, calibration tests were performed on the electric field probes, in which various voltages were applied and the analog-to-digital converter counts were observed. Least-squares regression was used to find a best-fit polynomial to convert the measurements to the applied voltage. This polynomial was used post-flight to find the actual voltage between the two probes to within 10 mV. No bias terms were calculated. Instead, the data are bandpass-filtered to allow only the frequencies corresponding to the mechanical motion of the spacecraft, thus removing offsets and slow changes. Using this type of probe, offsets are more indicative of differences in surface properties of the probes themselves than of an actual ambient electric field.

4.2 Coordinate Systems

4.2.1 Measurement Coordinate Frames

The body coordinate system for the main payload is shown in figure 4.1, and the subpayload coordinates are in figure 4.2. The main payload spins in the opposite direction with respect to its own body coordinates as the subpayloads with respect to their body coordinates. The electric field probe coordinate systems match the x- and y- components of

the body coordinate systems. Note that the vector magnetometer coordinate system of the subpayload is left-handed, with the z-axis flipped compared to the defined body coordinate system. This is due to an assembly error, and is corrected by flipping the sign of the calibrated z-component measurements. The fluxgate magnetometer of the main payload is rotated into the body coordinate frame b from its own frame fg using the following transformation:

$$B_b = \begin{bmatrix} 0 & \cos(210°) & -\sin(210°) \\ 0 & \sin(210°) & \cos(210°) \\ 1 & 0 & 0 \end{bmatrix} B_{fg} \tag{4.1}$$

The main payload had active attitude control with the goal of aligning the deployed subpayloads' spin axes to the magnetic field within 5°, and aligning its own spin axis to the magnetic field to within 3°. The initial alignment error of the main payload was small, but grew throughout the flight, so the actual maximum alignment error was not as good, nor were those of the subpayloads. Table 4.1 shows the peak alignment error in during the flight of each of the payloads. Using the calibrated magnetometer measurements, the actual errors α were calculated as the inverse cosine of the ratio of the magnitudes of the spin plane components and the total field, or

$$\alpha = \arccos\left(\frac{\sqrt{B_x^2 + B_y^2}}{\sqrt{B_x^2 + B_y^2 + B_z^2}}\right). \tag{4.2}$$

It is fair to say that the z-axis of the magnetometers is roughly aligned to the magnetic field. Since at this latitude, the field points mostly up, it is equally fair to say that the z-axis corresponds roughly to the up-axis in the local East-North-Up coordinate frame.

4.2.2 East, North, Up and North, East, Down

The East-North-Up (ENU) and North-East-Down (NED) are local coordinate systems that move with the spacecraft, in which the magnetic field measurements are considered most relevant and intuitive. The x-axis is East in ENU and North in NED, the y-axis is

Payload	Alignment Error Goal	Actual Alignment Error
Main	3°	12.2°
Sub 1	5°	7.9°
Sub 2	5°	6.8°
Sub 3	5°	12.1°
Sub 4	5°	9.4°
Sub 5	5°	10.3°
Sub 6	5°	10.8°

Table 4.1: Maximum magnetic field alignment errors

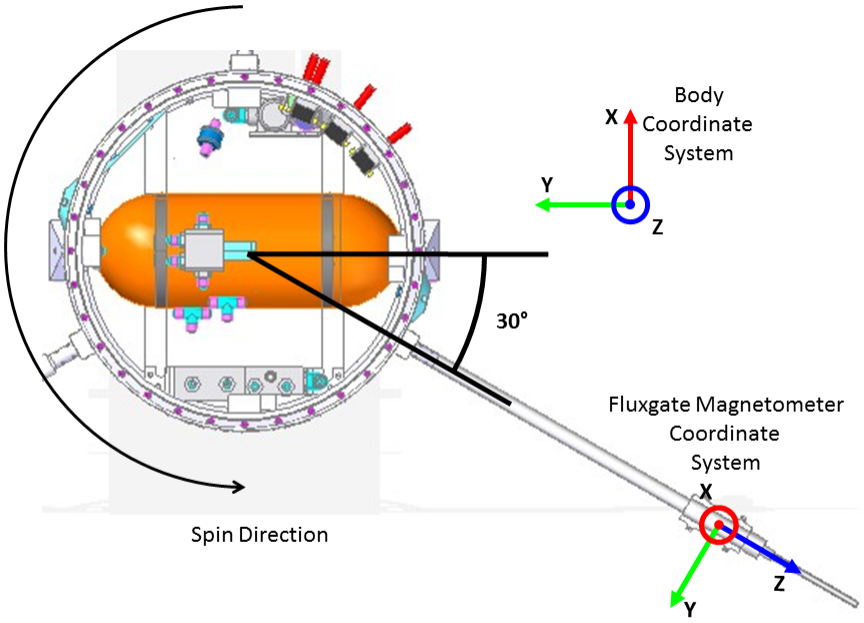

Fig. 4.1: Main payload body coordinate systems

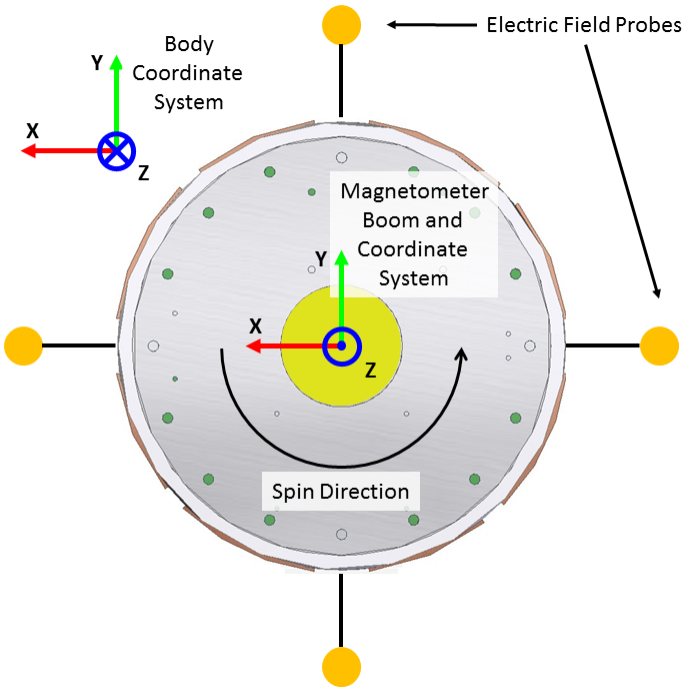

Fig. 4.2: Subpayload body coordinate systems

North in ENU and East in NED, and the z-axis is Up in ENU and Down in NED. Final measurements will be reported in ENU, but NED is required for some functions, such as the function used to produce IGRF comparison. A transformation between the two frames can be seen as a swap of the x- and y-axes, and a sign change in the z-axis, and when performed by a rotation matrix, the matrix is

$$R_{\text{ENU}}^{\text{NED}} = R_{\text{NED}}^{\text{ENU}} = \begin{bmatrix} 0 & 1 & 0 \\ 1 & 0 & 0 \\ 0 & 0 & -1 \end{bmatrix}. \tag{4.3}$$

4.2.3 Earth-Centered, Earth-Fixed

This frame is referenced in the equations used by the 6 DOF Simulink function. It is a non-inertial frame defined by the x-axis pointing from the center of the earth toward the prime meridian at the equator, the z-axis is aligned with the spin axis of the Earth, and

the y-axis is obtained by the right-hand rule. The local NED frame rotates with respect to this frame, and this is accounted for when determining the inertial rotation rates of the spacecraft. Rotations between this matrix and NED or ENU are well known and can be derived from information in [14]. The rotation matrix is

$$R_{\text{ENU}}^{\text{ECEF}} = (R_{\text{ECEF}}^{\text{ENU}})^T = \begin{bmatrix} -\sin\lambda & -\sin\phi\cos\lambda & \cos\phi\cos\lambda \\ \cos\lambda & -\sin\phi\sin\lambda & \cos\phi\sin\lambda \\ 0 & \cos\phi & \sin\lambda \end{bmatrix}, \tag{4.4}$$

where ϕ is the geodetic latitude and λ is the longitude of the spacecraft.

4.3 Physical Models

4.3.1 Rigid-Body Dynamics

Recognizing that the goal of the attitude estimation for ASSP is to achieve sufficient directional accuracy using methods that are simple to construct, we must build on the previous efforts of others. The MATLAB and Simulink software packages contain two tools that are key to the attitude determination method that will be pursued. The first is the six-degree-of-freedom dynamics model [15]. Although only the three degrees of freedom relating to the rigid-body kinematics are necessary, the model as a whole has been thoroughly vetted and proven external to this thesis, reducing the work required for the new method and strengthening the case for its use. The model refers to [16], [17], and [18]. By integrating quaternion-based equations of motion for a rigid body, the model simulates the rotation of the spacecraft. The capacity exists to include forces and moments, but these options will not be used. The fact that the equations of motion are quaternion-based is superfluous because it is not seen in the user interface. The advantages of quaternion-based equations are still realized: the model is free of singularities. The attitude is tracked by a direction cosine matrix output by the function relative to the local NED frame, accounting for rotation of the Earth. Locality is managed by the GPS data recorded by the spacecraft; this required

a minor change to the stock function, bypassing the integrated position and using direct inputs from the GPS instead.

The angular rates p, q, and r of the spacecraft relative to the NED coordinate system are expressed as a vector:

$$\vec{\omega}_b^{\text{NED}} = \begin{bmatrix} p \\ q \\ r \end{bmatrix}. \tag{4.5}$$

The angular rate of the Earth is

$$\vec{\omega}_E^I = \begin{bmatrix} 0 \\ 0 \\ \omega_E \end{bmatrix}, \tag{4.6}$$

and the rotation of the local NED frame relative to the ECEF coordinate frame is

$$\vec{\omega}_{\text{NED}}^{\text{ECEF}} = \begin{bmatrix} \dot{\lambda}\cos\phi \\ -\dot{\phi} \\ -\dot{\lambda}\sin\phi \end{bmatrix}. \tag{4.7}$$

The total angular rates of the spacecraft in the inertial frame are then

$$\vec{\omega}_b^I = \vec{\omega}_b^{\text{NED}} + R_{\text{ECEF}}^{\text{b}}\vec{\omega}_E^I + R_{\text{NED}}^b\vec{\omega}_{\text{NED}}^{\text{ECEF}}, \tag{4.8}$$

which are integrated by the quaternion equation

$$\begin{bmatrix} \dot{q}_0 \\ \dot{q}_1 \\ \dot{q}_2 \\ \dot{q}_3 \end{bmatrix} = -\frac{1}{2}\begin{bmatrix} 0 & \omega_b^I(1) & \omega_b^I(2) & \omega_b^I(3) \\ -\omega_b^I(1) & 0 & -\omega_b^I(3) & \omega_b^I(2) \\ -\omega_b^I(2) & \omega_b^I(3) & 0 & -\omega_b^I(1) \\ -\omega_b^I(3) & -\omega_b^I(2) & \omega_b^I(1) & 0 \end{bmatrix}\begin{bmatrix} q_0 \\ q_1 \\ q_2 \\ q_3 \end{bmatrix}. \tag{4.9}$$

In any physical system there are small perturbations present that remain unaccounted for in the mathematical model for purposes of simplifying the equations. This is indeed the case with ASSP. Most important of these physical effects recognized on the ASSP

payloads is that the deployed payloads attempted to deploy flexible wire booms with massive electrodes at the tips. The deployments were largely unsuccessful, and although this was unfortunate for the mission, as it makes using the measurements made by the electrodes more difficult (but not impossible), this fact improves the rigid-body assumption required for the physical model. Even so, the partial deployments observed do introduce perturbations associated with the independent motion of the electrodes and the energy dissipation by the short, flexible boom. Thus, it is not expected that the model will produce extremely accurate results, but that the output of the simulation will be sufficiently accurate to allow deconvolution of the measurements by attitude estimation.

4.3.2 Magnetic Field Model

Vector measurements must be obtained in an inertial reference frame as a comparison in order to determine attitude. The International Geomagnetic Reference Field (IGRF) will be used [19] with the latest (2015) coefficients. Note that the coefficients have changed since the latest update of [19]. The latest version of the MATLAB function by Drew Compston available at [20] will be used for all reference field calculations related to this work.

4.4 Nonlinear Least-Squares Attitude History Estimation

The Kalman filter is an accepted method for attitude estimation, but it is most appealing as an optimal solution when it can be applied in real-time. Since the ASSP mission has flown and data have been collected, a non-causal solution incorporating all measurements simultaneously may be advantageous, especially if its implementation is simpler than a Kalman filter. One such solution has been formulated using nonlinear least-squares to determine input parameters for a kinematic physical model of a rigid body. Of the literature surveyed, this approach is most similar to that of Zheng et al. [4], though it differs in that all kinematic parameters are estimated simultaneously, rather than sequentially, and relate to the spacecraft, its initial state and the sensors, rather than just its motion. The model will output estimates of the measurements at all relevant points in time which will be compared as a batch to the measured data. Additionally, this can be done without

deriving new equations or even building new computer simulations, since thoroughly tested and vetted procedures exist. In this new method, a nonlinear least-squares function that is built into MATLAB will be used with a 6 degree-of-freedom rigid-body dynamics model in Simulink. Both components require minor adjustments and additional facilitating code to implement with the ASSP data, but the most critical parts are already available for use.

4.4.1 Algorithm

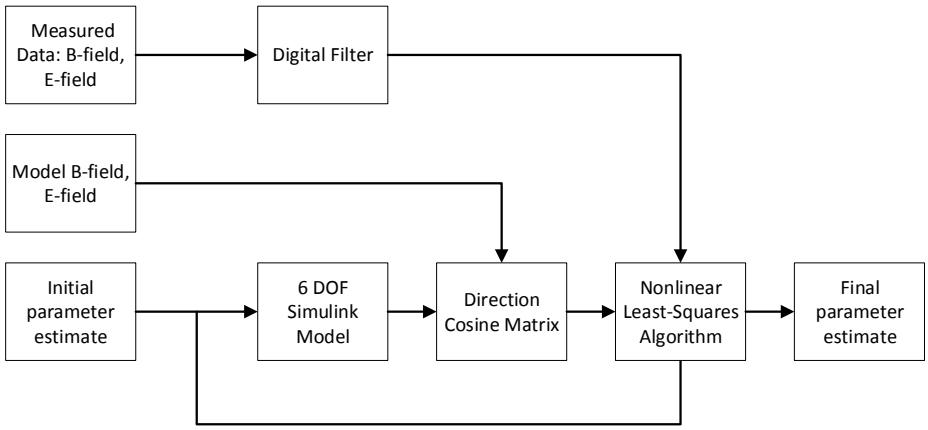

Fig. 4.3: Least-squares attitude estimation algorithm block diagram

The block diagram of the algorithm shows its flow. Significant perturbations to the electric field from the auroral arcs are filtered out by allowing only mechanical frequencies through the digital bandpass filter. The magnetometer data are only lowpass filtered just above the highest mechanical frequency, since the magnitude of each component of the magnetic field is critical to the method. This removes the high-frequency measurement noise. The measurement data are then input to the least-squares algorithm. Model B-field data are generated using the IGRF model, while the reference E-field is produced by crossing the velocity of the spacecraft as measured by GPS with the model B-field to obtain the $\vec{V} \times \vec{B}$ term of the electric field, which is the major contributor to the sensed field on the spacecraft. These are input to the 6 DOF physical model, of which only 3 degrees of freedom are actually utilized. The model outputs a direction cosine matrix that

represents the estimated attitude. The model data are rotated using this matrix to obtain the measurement model, which is compared to the actual measurements at each iteration of the least-squares algorithm. Since the simulation must be run multiple times each iteration, the method is computationally expensive, but the desired advantage is achieved in simplicity of implementation.

The relevant mechanical equations are given in section 4.3.1. At each timestep of the simulation, the model magnetic and electric fields are rotated into the spacecraft body frame by the equations

$$B_{\mathrm{IGRF,b}} = R^{\mathrm{b}}_{\mathrm{NED}} B_{\mathrm{IGRF,NED}} \tag{4.10}$$

and

$$E_{b,\mathrm{model}} = R^{\mathrm{b}}_{\mathrm{NED}} E_{\mathrm{NED,model}} \tag{4.11}$$

where R^{B}_{NED} is the direction cosine matrix transforming a vector from the local NED frame to the spacecraft body frame. Once the simulation is complete, the compensating bias term B_{bias} is added to the magnetic field:

$$B_{\mathrm{model,b}} = B_{\mathrm{IGRF,b}} + B_{\mathrm{bias}}. \tag{4.12}$$

No bias is added to the electric field, since the measured data are centered about zero post-filtering, as are the model data post-rotation. The actual measurements are then subtracted from the model measurements to obtain the total squared error:

$$S = \sum_i \sum_n (F(x_{i,n}, t_n) - y_{i,n})^2, \tag{4.13}$$

where x is a set of parameters defining the kinematic motion of the spacecraft (see section 4.4.2), y is the set of measurements (an $i \times n$ matrix), i being the number of measurement components or channels, and n being the number of observations in time. Using three magnetic field components and 2 electric field components, $i = 5$. The matrices are rectangular since the magnetic and electric field channels were sampled at the same rate on

each payload. The nonlinear least-squares algorithm used is the Trust-Region-Reflective algorithm [21] lsqnonlin with the interface lsqcurvefit, which are found in the MATLAB Optimization Toolbox [22] [23].

4.4.2 Estimated Parameters

Outputs of the least-squares algorithm include estimates for the following parameters that define the kinematic motion of the spacecraft:

1-3. Moments of inertia about the spacecraft body axes

4-6. Products of inertia relating to the spacecraft body axes

7-9. Initial Euler angles: roll, pitch, and yaw

10-12. Initial rates of change of the Euler angles

13-15. Magnetic bias term, covering calibration errors and the difference between the ambient field and the IGRF model.

In minimizing least-squares, situations may be encountered in which the differences in sensitivity between the parameters may cause some of them to cover more or less of the actual least-squares difference than they should. Another way to say this is that some less sensitive parameters may inappropriately "absorb" some of the least-squared difference that should be accounted for with another parameter. There are steps that can be taken to mitigate this. First, and most important, a watchful and experienced eye may recognize changes in parameters that may seem nonphysical. Secondly, the algorithm used allows for a relative step size to be implemented, so that larger steps may be taken for less sensitive parameters, lessening improper absorption by those parameters. In this case, the step sizes of the inertia elements were 1000 times smaller than the steps of the initial Euler angles and rates, while the magnetic bias steps were 100 times larger than the initial rotational state. Finally, bounds can be set on the various parameters that keep it within a certain range of the initial guess. The bounds used for the main and subpayloads are listed in tables 4.2 and 4.3.

Parameter	Bound	Units
I_{xx}	$\pm$ 5	$\mathrm{kg\,m^2}$
I_{yy}	$\pm$ 5	$\mathrm{kg\,m^2}$
I_{zz}	$\pm$ 5	$\mathrm{kg\,m^2}$
I_{xy}	$\pm$ 1	$\mathrm{kg\,m^2}$
I_{yz}	$\pm$ 1	$\mathrm{kg\,m^2}$
I_{zx}	$\pm$ 1	$\mathrm{kg\,m^2}$
ψ	$\pm$ 0.52	rad
θ	$\pm$ 0.52	rad
ϕ	$\pm$ 6.28	rad
$\dot{\psi}$	$\pm$ 1	$\mathrm{rad\,s^{-1}}$
$\dot{\theta}$	$\pm$ 1	$\mathrm{rad\,s^{-1}}$
$\dot{\phi}$	$\pm$ 0.002	$\mathrm{rad\,s^{-1}}$
c_x	0 $\pm$ 1000	nT
c_y	0 $\pm$ 1000	nT
c_z	0 $\pm$ 1000	nT

Table 4.2: Main payload parameter bounds

Parameter	Bound	Units
I_{xx}	$\pm$ 0.001	$\mathrm{kg\,m^2}$
I_{yy}	$\pm$ 0.001	$\mathrm{kg\,m^2}$
I_{zz}	$\pm$ 0.6	$\mathrm{kg\,m^2}$
I_{xy}	$\pm$ 0.0005	$\mathrm{kg\,m^2}$
I_{yz}	$\pm$ 0.0005	$\mathrm{kg\,m^2}$
I_{zx}	$\pm$ 0.0005	$\mathrm{kg\,m^2}$
ψ	$\pm$ 0.52	rad
θ	$\pm$ 0.52	rad
ϕ	$\pm$ 6.28	rad
$\dot{\psi}$	$\pm$ 2	$\mathrm{rad\,s^{-1}}$
$\dot{\theta}$	$\pm$ 2	$\mathrm{rad\,s^{-1}}$
$\dot{\phi}$	$\pm$ 0.1	$\mathrm{rad\,s^{-1}}$
c_x	varies	nT
c_y	varies	nT
c_z	varies	nT

Table 4.3: Subpayload parameter bounds

The bounds are set based on the expected magnitude of the quantity and how well the initial guess is known. The inertia bounds for the main payload are different from those used for the subpayloads because the magnitudes of the inertias were very different. The moments of inertia were measured for the main payload in its fully deployed state prior to launch, and it was assumed that these were sufficiently close to the principal moments of inertia that the products were initially guessed to be zero. The entire inertia tensor of the subpayloads was measured on the ground, but two issues prevent this from being a good initial guess. First, for the entire time interval of interest the electric field probes are in a deployed state, reducing the measured inertia to no more than a decent guess. Second, the repeatability of the measurements of the products of inertia was low. This led to an initial guess of zero for the subpayload products of inertia as well. Indeed, for both of these reasons, agreement to ground-based product of inertia measurements is poor, but expectedly so. Because the electric field probe deployed length was actually quite short except for subpayload #4, agreement is fair for the moments of inertia on the subpayloads. A final note on the inertia estimates is that the ratios of the different elements of the inertia tensor are what define the motion, and not their absolute magnitude. This must be considered if inertia estimates output by this method are intended for any other use.

The initial guess for the Euler angles and rates were completely unknown, except for the spin rate and the knowledge that the main payload attempted to align the z-axis of all payloads to the magnetic field, which was largely pointed in the Down direction. The unknowns were also set to zero at first, until a better guess was found that fit the measurements well, when a guess for all parameters was had. For this reason, the bounds were set high, relative to their magnitude. The sensitivity to the Euler angles and rates was also high: relatively small changes in these quantities could change a fair fit to measurements into a very poor one, so these bounds were found to be acceptable.

The simple bias term in the magnetometers was the least sensitive measurement, and most prone to "absorbing" the effects of other parameters, especially the initial rotational state. Being unknown, these were also first guessed to be zero, and iterated upon manually

until a better guess was found. The default bound was 1000 nanoteslas, but this bound had to be raised on some payloads if a reasonable converged solution could not be found otherwise, and only incremented very slowly at that point to ensure that the estimate did not run away with the bias terms. To explain why some bounds had to be expanded, we first recognize that they were chosen to be relatively tight (it would not be unexpected or inconsistent with previous measurements for the ambient field and the model to differ by several thousand nanoteslas), and that care was taken in expanding them to avoid the problems due to flexibility in this parameter. We also recognize that each payload had a unique (and imperfect) magnetometer calibration, and more calibration compensation may have been needed for some payloads.

In the next section, assumptions are covered that limit the applicability of this implementation of this method, but the discussion above already hints at the possibility that the solution found may be a local minimum, rather than the proper global minimum. With any physical model, some assumptions must be made, and the consequences of those assumptions accepted. In this case, deficiencies in the physical model may mean that the true global minimum of the cost function may not be verified, or that the true global minimum may be a poor fit to the data, and improper at that. Additionally, considering that the ratios of the inertia elements define the motion rather than their magnitudes, any number of equal minima may exist in this function space. Intelligent consideration of the results must accompany any application of this attitude history estimation method. If the convergence point found when applying this method is believed to be a local minimum, then expansion of the physical model is the recommended remedy.

4.4.3 Assumptions

The method makes the following assumptions:

1. The spacecraft body is rigid
2. The sensors are at the center of mass of the rotating body
3. Energy dissipation is negligible
4. The ambient magnetic field changes slowly compared to all mechanical frequencies of the spacecraft
5. A single bias term compensates for both calibration deficiencies and differences of the measured field from the model field.

Assumption 1 most accurately describes the main payload. It extends booms that can flex, but during the time interval of interest, the payload is no longer actively controlled, and plenty of time has passed to allow the vibration of the booms to dissipate. Out of necessity, the subpayloads have wire booms, rather than rigid booms. However, the deployed length for the booms was extremely short except on subpayload #4, and so the vibrations should damp out relatively quickly, and the spacecraft will follow the rigid-body assumption closely, since no moments are applied to the spacecraft. For subpayload #4, it is assumed that sufficient time is given for the damping of the vibrations, at which point the increased moment of inertia about the spin axis enables the system of the body and sensors to follow the rigid-body assumption closely.

Assumption 2 is nearly true for the electric field probes, since the measurement is already assumed to be halfway between the probes, which is near to the spacecraft center of mass. This assumption is less true for the magnetometer, which is placed on a boom to avoid magnetic contamination. However, the distance of the magnetometer from the center of mass is very small compared to the spatial scales required to make a noticeable change in the measurement, and since the booms are rigid the magnetometer will follow the rotations of the center of mass almost exactly.

Assumption 3 refers to the fact that the motion of the flexible booms will damp over time and the energy must be dissipated. It is assumed that the damping has largely occurred before the time interval of interest and remaining energy dissipation is negligible. The statement of this assumption and assumption 1 can be extended to a statement that the

physics model is complete. The same algorithm may be used with a more detailed physical model if this assumption proves untrue and the attitude estimation is insufficient as a result.

Assumption 4 must be true or changes in the magnetic field may be confused with changes in the rotation of the spacecraft. The assumption also must hold for both the reference magnetic field and the ambient field being measured. The reference field is certainly of no concern: the time derivatives in the spherical harmonic model reference months and years, changing over far longer time periods than the domain of seconds that covers the mechanical motion of the payloads. For knowledge of ambient field changes, we refer to Park et al. [1] whose plots of magnetic field appear to show disturbances that occur over about 10 seconds. The unsteadiness of the disturbances will likely prevent confusion with the very regular spin and precession of the payloads. Spatial motion is a much more significant effect for ASSP, as indicated by figure 4.4, but these changes are still very slow compared to the mechanical frequencies of the spacecraft, the slowest of which are on the order of tens of milliHertz, and correspond to the precession of the main payload. It is conceivable that some magnetic field perturbations may exist that change more rapidly than this, but the effects of these will be smaller much smaller in magnitude than effects due to changes in the spacecraft rotation, which will easily be compensated for by the least-squares fit.

Assumption 5 is a statement that the true ambient magnetic field is not known perfectly. The calibration on the magnetometers is imperfect, and the IGRF model field which is used as a reference has significant differences due to the large currents flowing in measurement region. These differences will be addressed by an additive bias for each component of the measurement, and will be found as a parameter in the least-squares solution. A higher-order model could be used, but increases the number of parameters estimated by the least-squares algorithm.

4.4.4 Time Interval of Interest

The reference time t_0 is an arbitrarily chosen moment close to the ignition of the motors to which all data are referenced. The beginning of the time interval for which the attitude solution will be attempted is defined by the ejection and deployment sequences

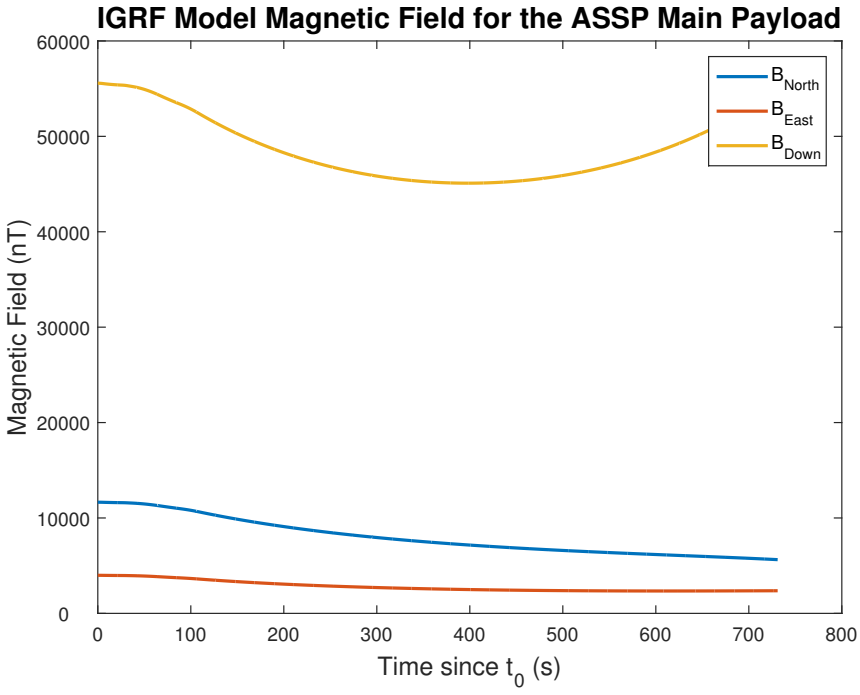

Fig. 4.4: IGRF components for the main payload trajectory

of the subpayloads and the final pointing of the main payload, which are all complete by approximately 215 seconds past t_0. Subpayload #1 suffered a downlink glitch from about 648 seconds to about 656 seconds. Since the scientific goals of the campaign are best served by comparing data from all payloads, and since this glitch complicates attempts at digital filtering but was not encountered on the other payloads, this point defines the end of the time interval, trimmed to 646 seconds. By 646 seconds, the rocket has passed through the dynamic aurora and most of the signal of interest has already been obtained. Further time is removed to account for the boundary effects of the digital filters used, so the time interval becomes 250 seconds to 646 seconds. The end time does not change because the filtering can be performed on data beyond 646 seconds and trimmed to that value.

4.5 Comparison Methodology

There is no evidence in published literature that an attitude solution similar to this has been attempted before. It is important to note that this is not a solution to Wahba's

problem. Those solutions determine an optimal attitude matrix for a given instant in time, while the new method calculates the entire time history simultaneously by calculating a set of parameters relating to a physical model. There is confidence in the components of the method, but the new algorithm as a whole is unproven for attitude determination. A detailed mathematical analysis is beyond the scope of this thesis, but appropriate qualitative and quantitative comparisons will be made to proven methods to ensure that the desired results have been achieved. The comparisons made include:

1. Qualitative trend agreement
2. Euler angle comparison
3. Spherical angle differences

A qualitative trend agreement is important, because the payloads, though in different locations, should experience largely the same magnetic and electric fields. Trends can also be compared in the expected measurements: rotating the model fields into the body coordinate frame may yield additional insight into the workings of each method. Comparing Euler angles will allow for a qualitative and quantitative measure of the two methods in which the actual rotations themselves are represented. Finally, a comparison of the spherical angles (azimuth and elevation) will quantify the differences in vector direction in the rotated product. The comparison will be made between the attitude solution and the model field. Previous campaigns [3] and [1] found that the variations in the spherical angles through the flight was less than 1°, as were the differences between the angles measurement and the model. For the scientific goals of ASSP, it is desired to resolve the direction of the vectors to an accuracy of less than 5°, with up to 10° being acceptable. For each comparison, the rotated measurements will be filtered to remove remnants of mechanical frequencies (the unfiltered, rotated measurements will also be shown). The comparison sources are the model fields, attitude from inertial sensors, and the TRIAD algorithm. Each comparison source and each different applicable measure will be plotted and analyzed.

4.5.1 Model Fields

The qualitative trend agreement is the first check for each attitude solution, comparing rotated data with the model field. The model magnetic field changes by only a few percent by any measure given the spatial differences of the payloads during the flight, and past experiments have shown that the model agrees well with in situ measurements [3]. The small spatial- and temporal-scale structures of the perturbations in the magnetic field are not well known, hence the goals of the rocket campaign, but the large-scale deviations from the IGRF model are known to be slow compared to ASSP measurement timescales. The model and the measurements will not likely differ by more than a several hundred to a few thousand nanoteslas in magnitude. The overall trends of the rotated measurements should agree with the trends predicted by the IGRF, and so this agreement will be an initial confirmation that the attitude solution has some level of validity.

4.5.2 Inertial Sensors

As stated, the inertial sensors on the subpayloads did not provide the necessary measurements for an inertial attitude solution. However, the main payload used a different inertial sensor system, and the measurements were professionally reduced to obtain an attitude solution for the main payload. The estimated accuracy of the inertial attitude solution is 1° everywhere. This will provide a useful comparison to ensure that the new method estimates a reasonable attitude history before applying it to the subpayloads.

4.5.3 TRIAD Method

As discussed in chapter 2, there are several methods that seek the optimal attitude matrix, most of which are not difficult to implement. However, the lack of a body-z axis measurement of the electric field introduces a deficiency that weakens the usefulness of all of these methods. The true attitude matrix likely differs considerably from that calculated by these methods, as each attempts to match the two vector measurements to their counterparts in the reference frame, and so any attitude matrix produced will favor a hypothetical electric field vector more fully in the body x-y plane than the actual electric field vector. It

is hoped, however, that using one of these methods will at least share similar trends and/or magnitudes of the Euler angles in the solutions as a true solution. The TRIAD method, SVD method, q-method, and other solutions to Wahba's problem share in common that they solve for the attitude at each moment in time independently. This fact, though a weakness in most practical applications, aids in their use as potential comparisons. Any angles solved for should not vary drastically from one timestep to the next; in other words, the angular rates should appear to conform to some reasonable physics. Considering this, invalid portions of an attitude solution obtained by these methods should be easily identifiable, even if the absolute validity of other portions can not be confirmed. This uncertainty leads to the rational decision that only the simplest of the methods previously discussed should be tried at first: the TRIAD method. The TRIAD method, using the magnetic and electric field measurements, will be applied with the magnetic field as the first measurement in the algorithm. In this application, the body-z component of the electric field will be set to zero. This will cause the expected inaccuracies, but clues and consistencies in the trends should provide a comparison for the new method concerning the subpayload attitude solutions, at least during some portion of the flight. As Markley notes in [7], this usage may still produce an optimal attitude estimation for each moment in time if the two vectors are appropriately weighted. It must be emphasized that this is still an insufficient attitude determination method because the attitude matrix that provides an optimal fit to the vector observations may imply rates of change of the Euler angles that are not physically plausible for these spacecraft, hence this method is used only for comparison.

4.6 Data Reduction

With the attitude solution for each payload, the calibrated, unfiltered magnetic field data are rotated into the ENU frame in two steps:

$$B_{\mathrm{ENU}} = R_{\mathrm{NED}}^{\mathrm{ENU}} R_b^{\mathrm{NED}} B_b. \tag{4.14}$$

This greatly reduces the strength of the mechanical frequencies in the result (see figure 4.5),

but artifacts of the motion remain. A lowpass filter is again applied to sufficiently remove these artifacts. Seeking perturbations in the measurements, a low-order polynomial fit of the measurements is subtracted to leave only perturbations of the magnetic field in the observations in each component of the ENU frame (figure 4.6).

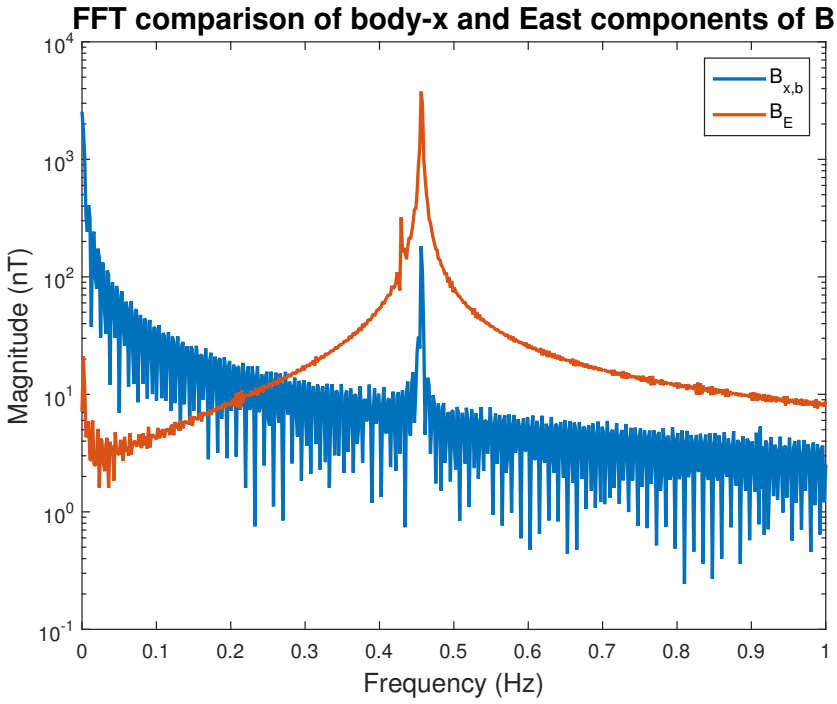

Fig. 4.5: Partial frequency spectrum of main payload before and after rotation

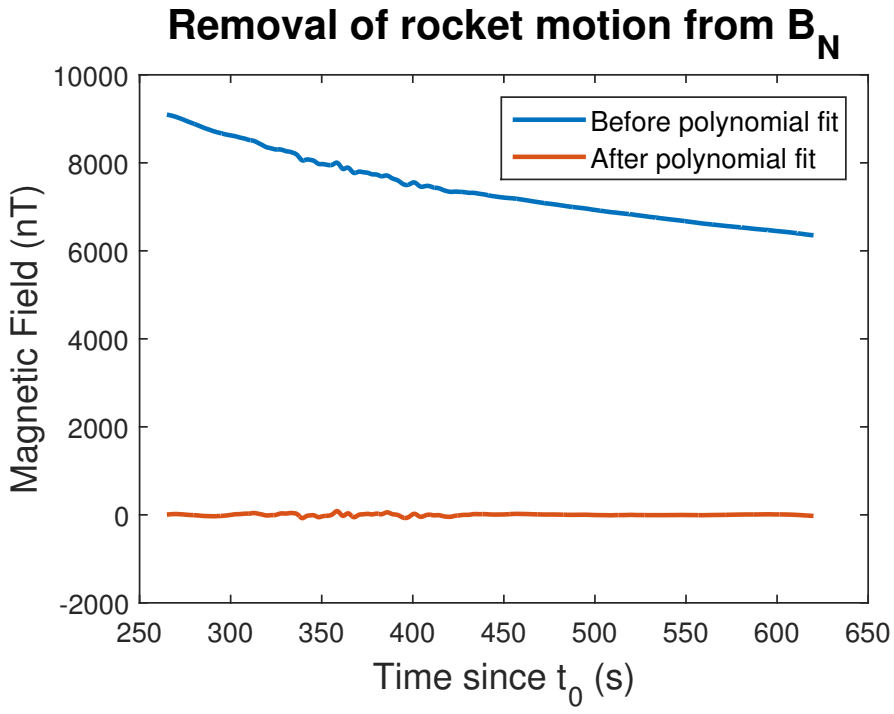

Fig. 4.6: Main payload North component observations before and after polynomial fit

Chapter 5

Attitude Estimation Results

The main payload and subpayloads are not only mechanically very different from each other, the attitude estimation technique behaved very differently when applied to each group, so the results will be presented separately.

5.1 Sensitivity to Initial Guess

The attitude estimation is based in least-squares, and so the algorithm may not converge if the initial guess is not sufficiently close to truth, or it may converge to a local minimum that does not represent the true solution. The initial guess was obtained by taking a small number of measurements at the beginning of the time interval and changing the parameters in the initial guess until the trend of the simulation output was qualitatively similar to the actual measurement behavior. Then the algorithm was run with this rough guess, resulting in outputs that were quantitatively very close to the actual measurements, and an improved initial guess. At this point, the time interval did not yet encompass several full rotations or precession periods, so the solution was not unique. To address this, the time interval was extended forward in time a small amount to improve upon the guess, then the algorithm was run again. Several of these manual iterations were performed until the algorithm could converge automatically for the full time interval. Intuitively, this could bias the results towards matching the beginning of the flight. In practice on the subpayloads, this was seen to be the case for smaller time intervals, but when a large enough time interval was input, the least-squared error was large enough later on that the algorithm sought a better fit to all of the data, rather than just the early parts of the flight.

5.2 Nonlinear Least-Squares Results

Using the results obtained by iterating on the algorithm, we first compare the transformed measurements to the model field to observe whether the solution is sensible (figure 5.1). We immediately see that the large-scale trends and magnitudes agree very well with the IGRF. Some difference in magnitude is expected. Importantly, without any further processing some perturbations are already visible in the East and North components, between about 300 and 450 seconds. This means that while this is clearly not a finished product, the rotation is effective as a means to resolve the scientific observations of interest. However, the transformed vectors still reflect the mechanical motion of the spacecraft more strongly than expected. To investigate this, we must determine whether it is an artifact of the new solution or another factor, so we next compare to the gyro-provided solution.

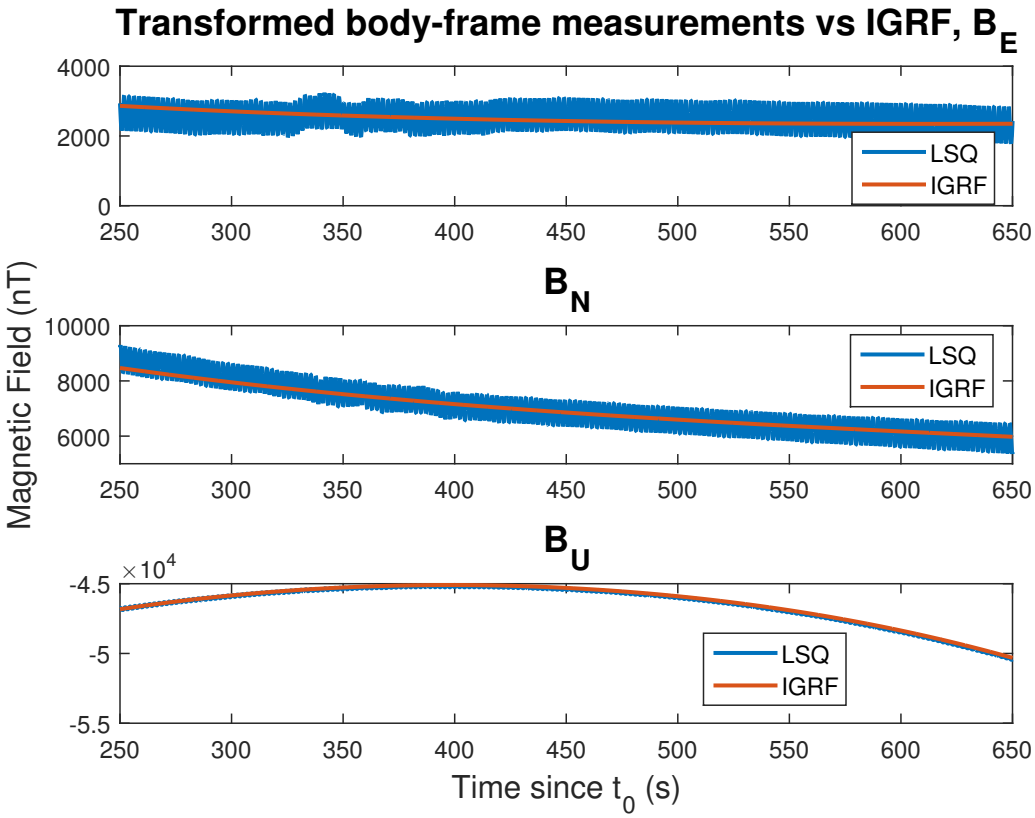

Fig. 5.1: Main payload transformed magnetometer measurements

5.2.1 Main Payload: Comparison to Inertial Attitude Determination

As stated in 4.5.2, the method was first tested on the main payload because an accurate alternate solution already exists from inertial sensors. The two attitude history estimates were compared by using the rotation matrices provided by each to rotate the fluxgate magnetometer measurements into the ENU frame. Both solutions were simultaneously compared to the IGRF model (figure 5.2). In this comparison we see that the differences are not insignificant, but also not very large, and that each component is different in its own way. The East component matches better later in the flight, while the North component is a better match earlier. We must also compare the electric field trends (figure 5.3). The model is very simplistic, and the actual field is not as steady as the model field, in addition to missing a measurement component. However, the components have the correct sign and magnitude, so we maintain that the attitude solution is valid.

There is still a significant waveform at the mechanical frequencies. We zoom in to the magnetic field plot to better see the remaining structure in the measurement (figure 5.4). This reveals that the two waveforms are in phase with each other, and have similar magnitudes, but the match is not exact for each component at all times. At the first peak, the difference in the East components is about 814 nT. At about the same time, the measured field magnitude is 47,674 nT. By the trigonometric relation

$$\alpha = \arcsin\left(\frac{|B_{E,\mathrm{LSQ}} - B_{E,\mathrm{Gyro}}|}{|B|}\right), \tag{5.1}$$

we estimate that the resulting vector has an East component pointing difference of about 0.98°. Applying the same relation to the last peak in the interval, for the North component, we see an angular difference of about 0.65°. Finally, for the Up component, near the beginning of the time period, the maximum angular difference is about 0.1°. Applying this method to the whole time interval, we achieve figure 5.5. The expected accuracy of the alternate solution is 1°, (see report by Smith [24]) so the two solutions are in agreement.

To address the reason that the mechanical frequencies remain so strongly visible after transformation, we consider the measurements of another magnetometer on board the

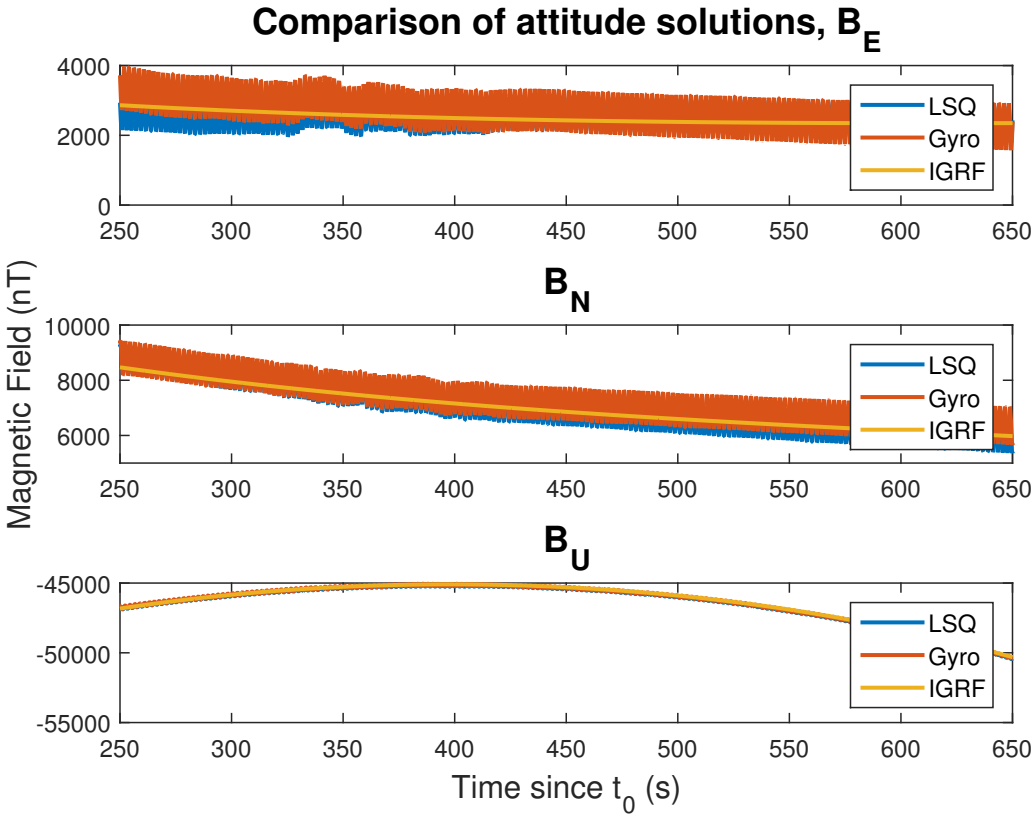

Fig. 5.2: Main payload attitude solution comparison: B-field

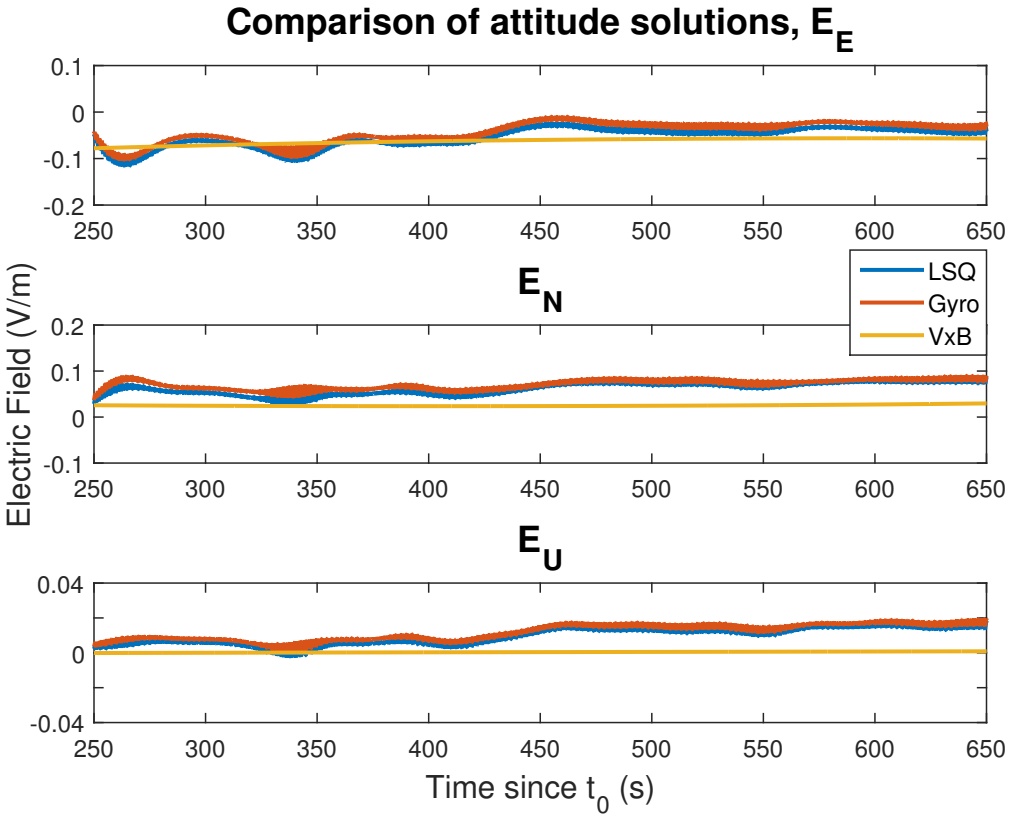

Fig. 5.3: Main payload attitude solution comparison: E-field

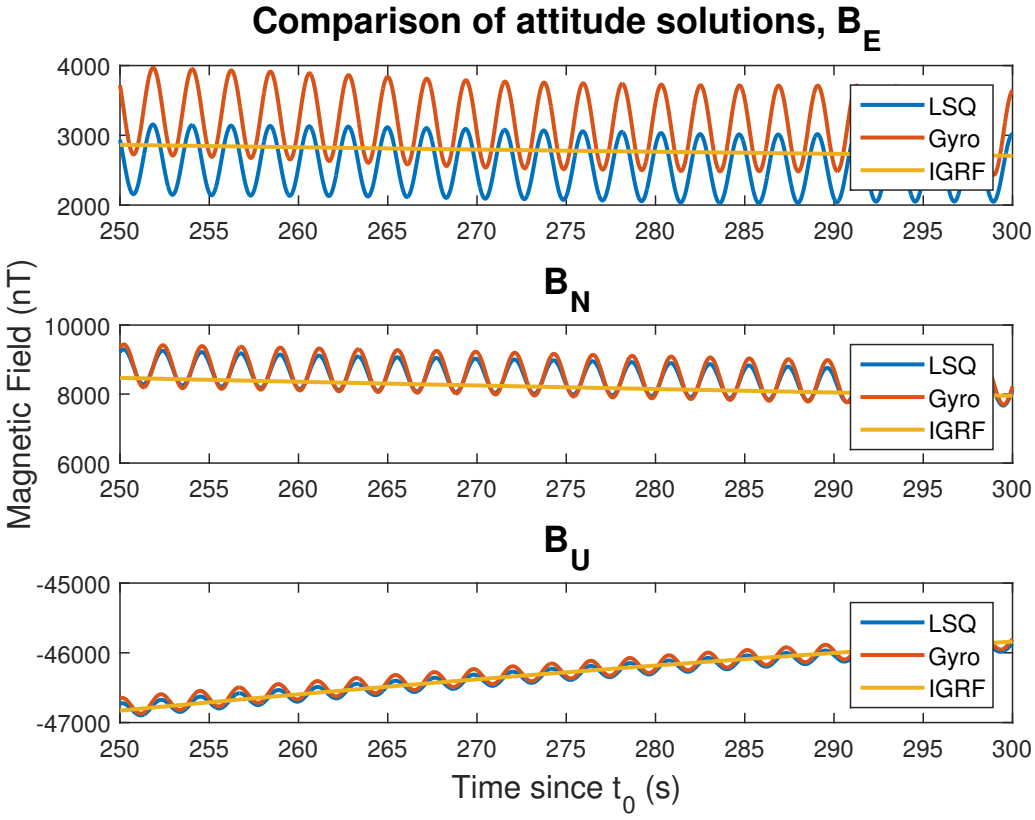

Fig. 5.4: Main payload attitude solution comparison - zoom

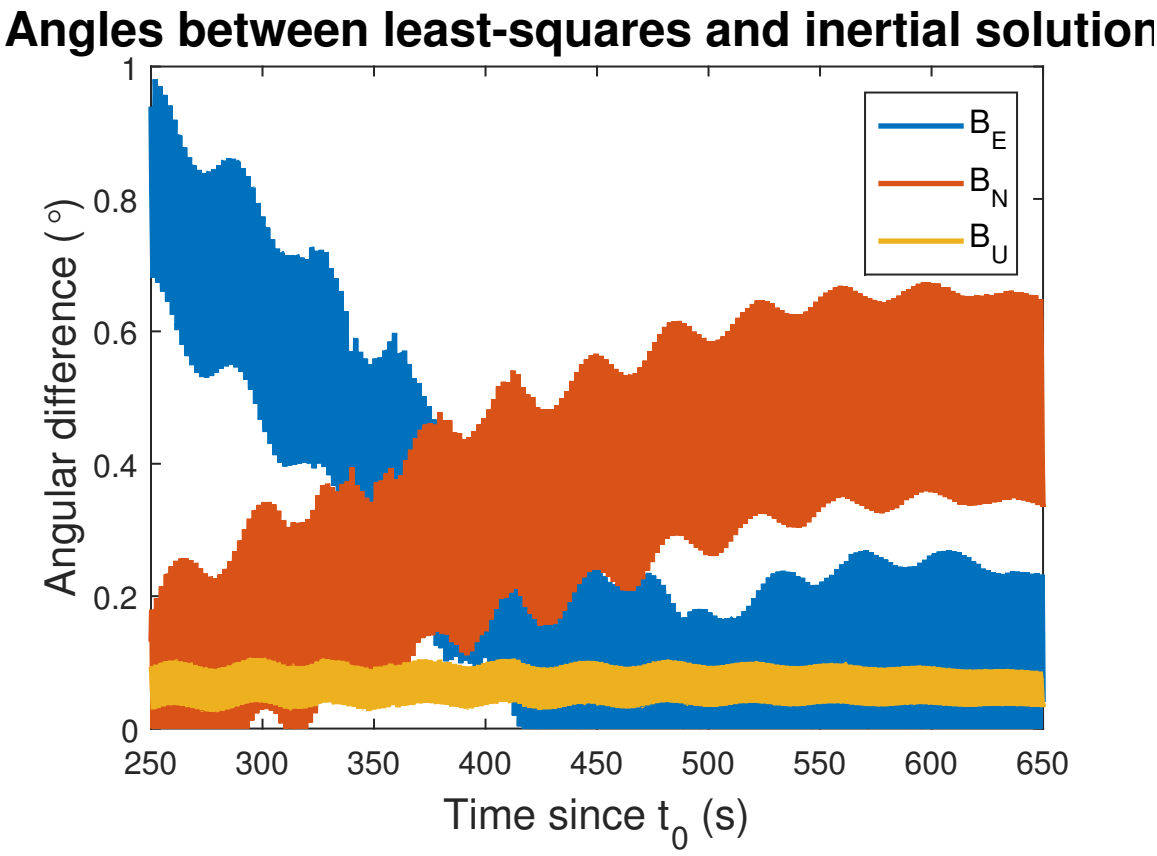

Fig. 5.5: Angular differences in main payload attitude solution

payload. This was also a well-calibrated fluxgate device, but not intended for science, and was part of the attitude determination subsystem. We compare the transformed measurements from this instrument using the attitude solution provided by the gyros to the fluxgate measurements transformed by the same attitude matrix. This yields figure 5.6, from which we see that the same artifacts exist in equal strength, neglecting the slight differences in trend between the two instruments. Two different attitude solutions by two independent methods have been used to compare observations in a useful frame from two separate instruments, and the results agree. By these indications, we deduce that there must have been some magnetic moment produced by the spacecraft that was not accounted for in the magnetometer calibration.

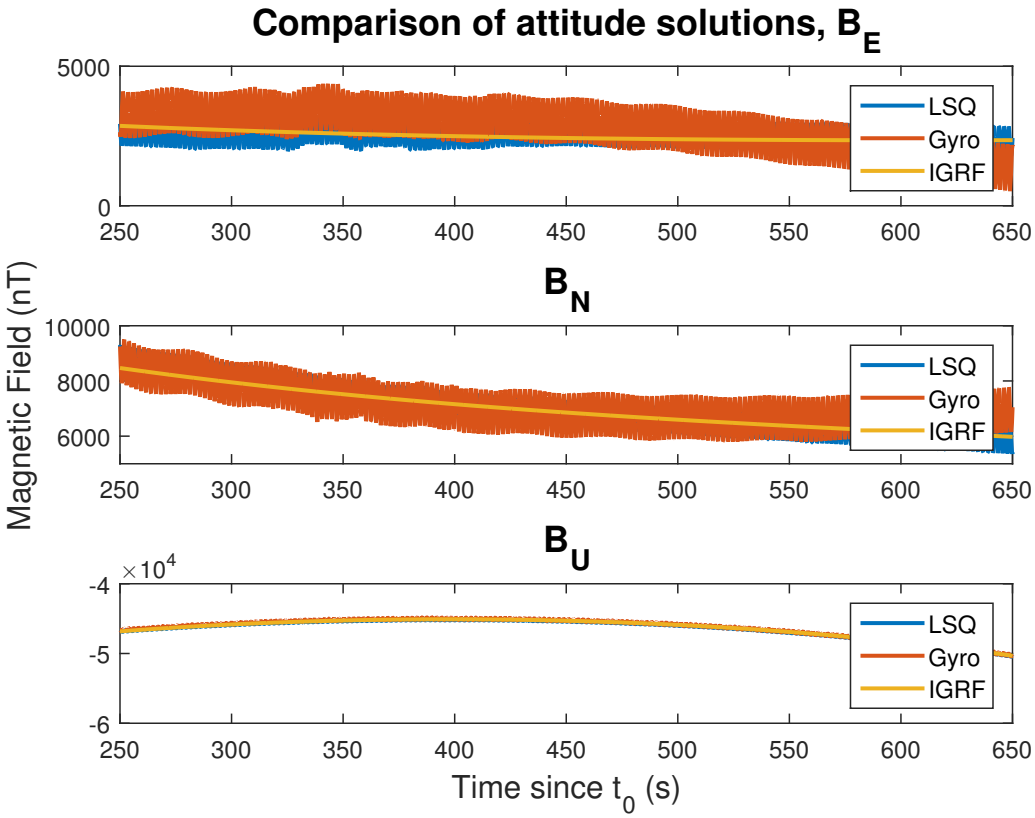

Fig. 5.6: Main payload attitude solution comparison

For a complete comparison, we also look at Euler angles from the two solutions, which

are expected to be similar. This will be another measure of the pointing error (figure 5.7). The Euler rotation assumed is 3-2-1. Note that the ϕ angle plot in figure 5.7 has a smaller time interval to better show the agreement between the two solutions. At first glance, the agreement is generally good, with a less than 1° separation in the second and third Euler angles. We then see that the first Euler angles of the two solutions are out of phase with each other by about 9.2°. Because the other comparisons do not show this as a vector pointing error in the transformed measurement, this is most likely due to axis misalignments between the two sets of coordinate axes for the sensors used to derive the two solutions. There are several places such misalignment could be included: in the sensor axes themselves, the sensor mounting the rocket body, the placement of the boom used to extend the science magnetometer away from the rocket body, and the definition of the body coordinate frame.

To get a better idea of the magnitude of the pointing errors, we transform the vectors to spherical coordinates and compare the observed azimuth and elevation (with respect to the local ENU frame) to that of the model field (figure 5.8). The differences between the measurement and the model should be small, as seen by previous similar rocket campaigns. We see that this is indeed the case. Acknowledging that the true field is an unknown and the calibrated magnetometers are the best attempt at measuring it, we notice that the new least-squares solution follows the trend of the model field somewhat better than the gyro solution. To be sure, the new solution provides adequate attitude estimation for the main payload, so we proceed to compare to TRIAD and then to apply the new method to the subpayloads.

5.3 Comparison to TRIAD

A comparison of the new method to the inertial solution is probably sufficient for the main payload for the purposes of this work. However, the subpayloads will only have a TRIAD method attitude estimate to compare to. Indeed, the TRIAD method is expected to perform the best for the main payload, given the improved quality of the electric field data, so we compare here to see what agreement can be expected (figures 5.9 and 5.10).

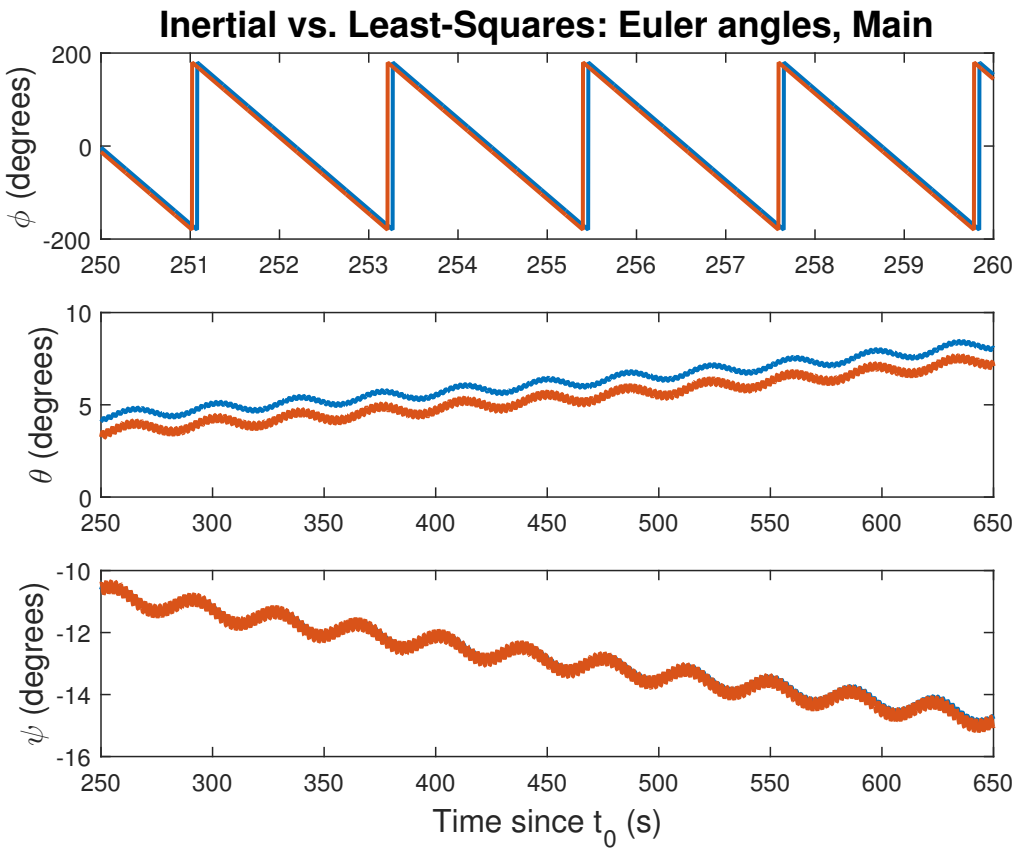

Fig. 5.7: Main payload Euler angle comparison

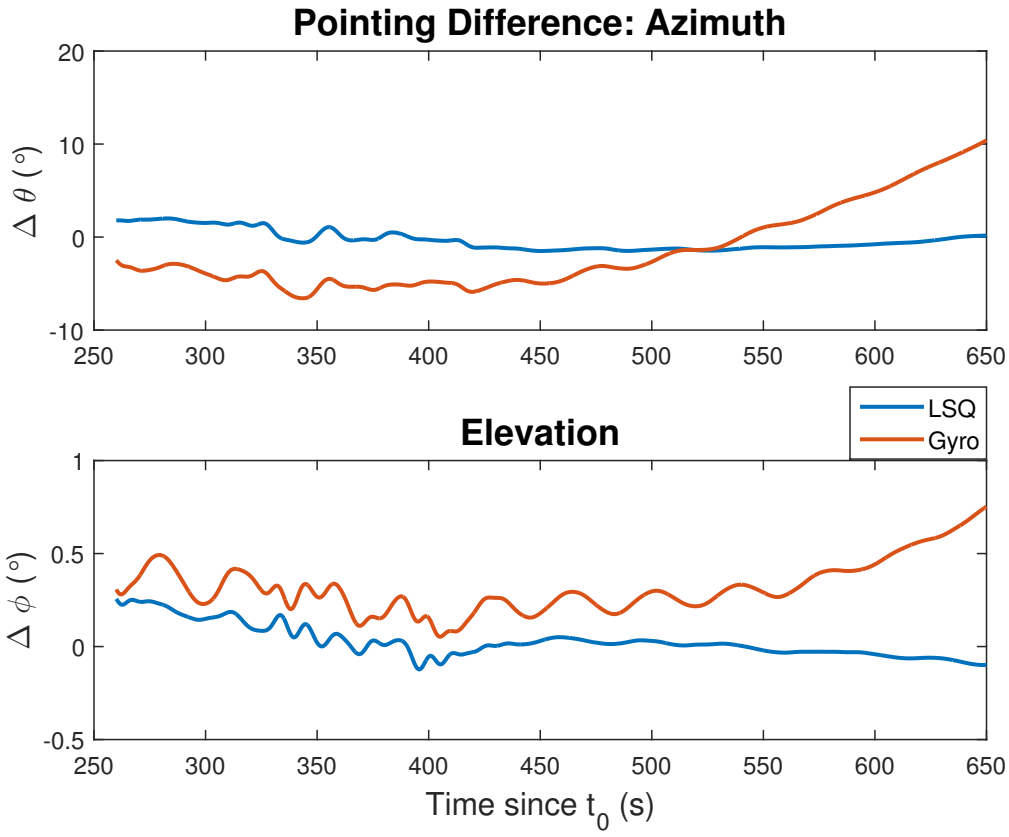

Fig. 5.8: Main payload pointing differences

From these figures, the TRIAD estimate appears to be a much better solution, but recalling that two independent magnetometers measured some bias field that remained after the application of the attitude solution, we see this is completely missed in TRIAD. This same effect would also change or remove signals of scientific interest from the measurements, which is problematic.

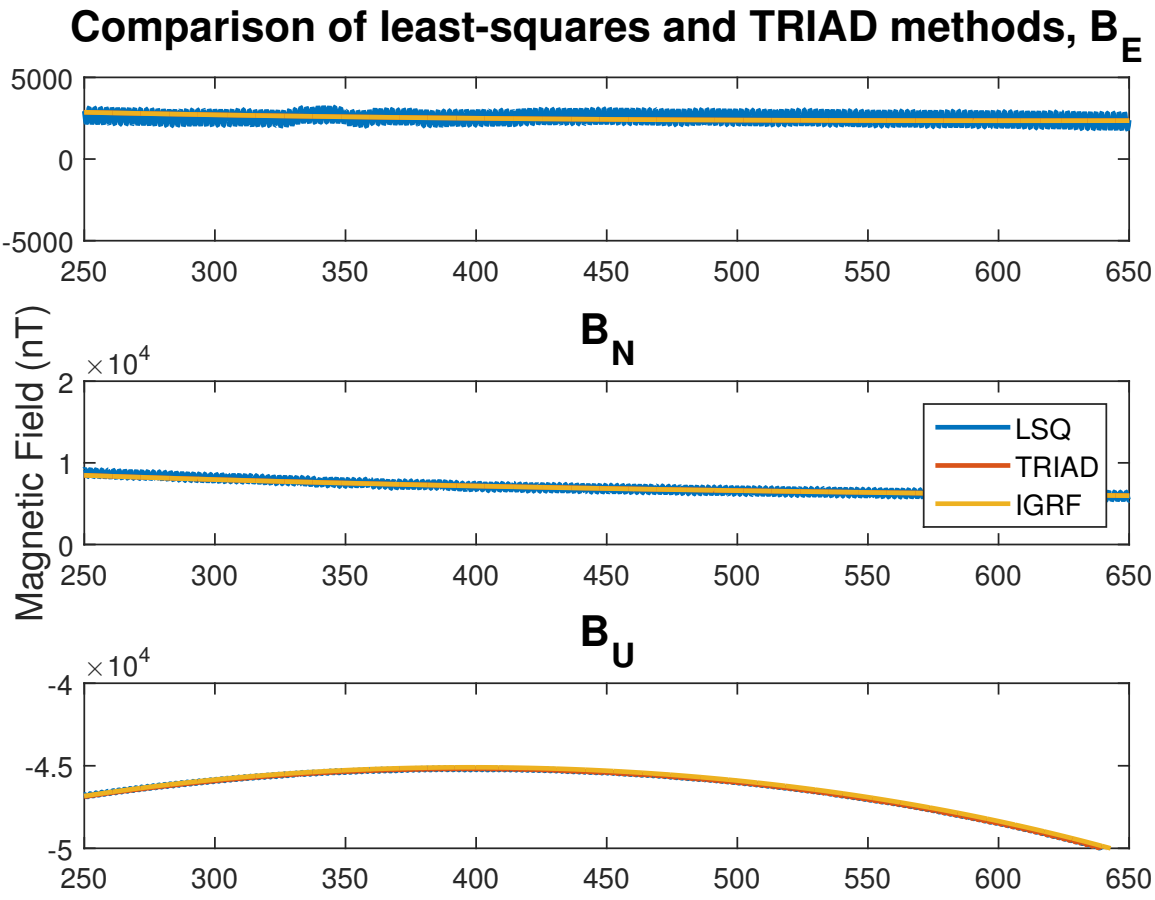

Fig. 5.9: Main payload TRIAD method comparison: B-field

In figure 5.11 the Euler angles of the main payload TRIAD solution are compared. We again see a slight phase difference in ϕ, which must be due to a difference in the estimation method rather than any physical effect, since the same measurements were used in both methods. We see differences in the θ angle, showing an offset of about 7° at the worst. The trend of θ is quite telling: TRIAD may produce a rotation that matches the measurements to

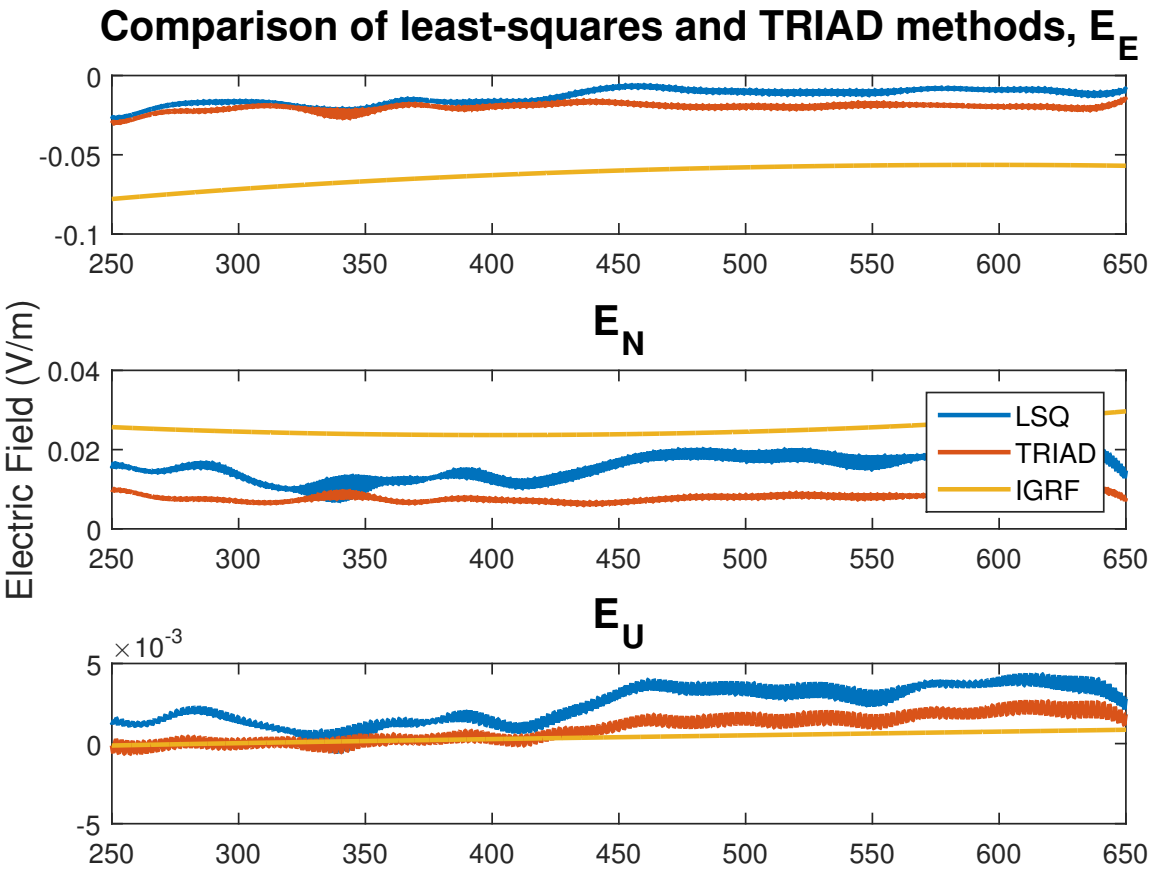

Fig. 5.10: Main payload TRIAD method comparison: E-field

the models, but it does so in a way that does not represent physical motion with time. The other solutions are defined such that they must represent physical motion, hence another weakness of TRIAD.

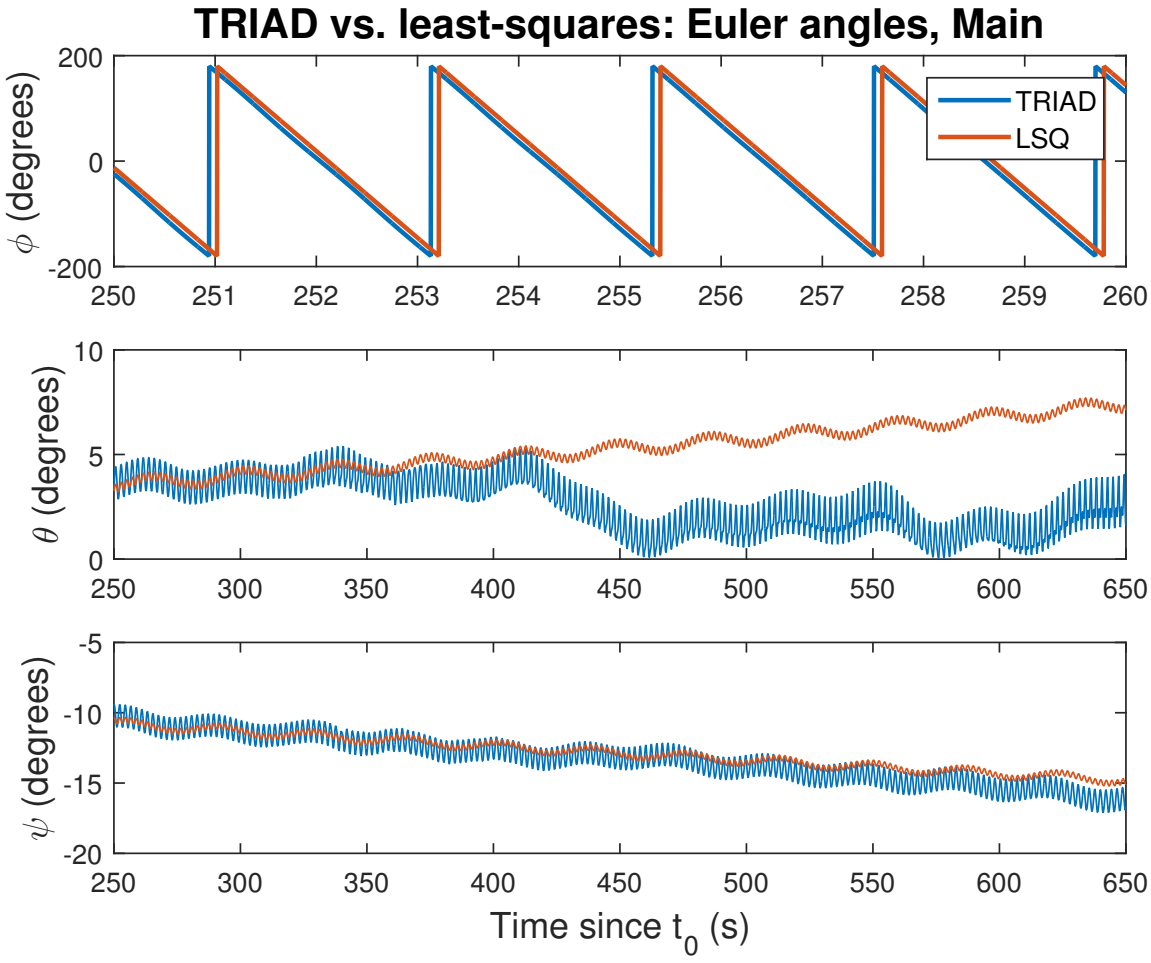

Fig. 5.11: Main payload TRIAD method angle comparison

When viewing plots of the electric field from the subpayloads, it should be noted that the magnitude of the electric field measured is a function of the distance between the two probes of the instrument. This distance is not well known on the subpayloads, and so only the sign and trend are good for comparison, and not the magnitude, since the magnitude scale was adjusted simply to make a close match on the plots.

Subpayload #4 had the highest quality electric field data, and so we begin our application of the new method and the TRIAD method there (figures 5.12 and 5.13). TRIAD finds a rotation matrix that best maps one set of vector measurements to another. As Markley states [7], this rotation matrix is optimal in terms of Wahba's problem if the measurement weights in the formulation of Wahba's problem would make the influence of one vector small compared to the other. This would likely be the case for ASSP in a sensible formulation of the problem, since a component is missing from the measurement, and so this may very well be the optimal matrix. This was insufficient for the main payload, but appears to work well for subpayload #4. The TRIAD trends follow very closely those of the model fields, more so than the least-squares solution does. However, as shown with the main payload, this does not necessarily make it a more appropriate estimate of the attitude history. The Euler angles compared in figure 5.14 for subpayload #4 show similarity, but there is not yet a sign that the scientific signal of interest was preserved.

Robinson, et al. [3] showed that perturbations due to auroral activity can be observed in the spherical angles of vector magnetometer measurements, and that the changes in the angle of the field are relatively small. These observations are confirmed in figure 5.8. Presented below are the residual angles between the model field and the measured, rotated field. Figure 5.15 shows the residuals when using the nonlinear least-squares method, and figure 5.16 shows the same for TRIAD, both displaying measurements by all payloads. We see clear pointing errors when applying the least-squares method, but we see nothing but filtering artifacts when applying the TRIAD.

Complete figure sets can be found in appendix A, covering the rest of the subpayloads. Figure 5.15 shows that varying levels of success were had applying the new method. It was desired that the attitude would be determined within 5°, with an acceptance threshold at 10°. We must therefore accept only the attitude solutions of the main payload and subpayloads #2 and #4, and recognize that the new solution is inadequate for the rest of the payloads.

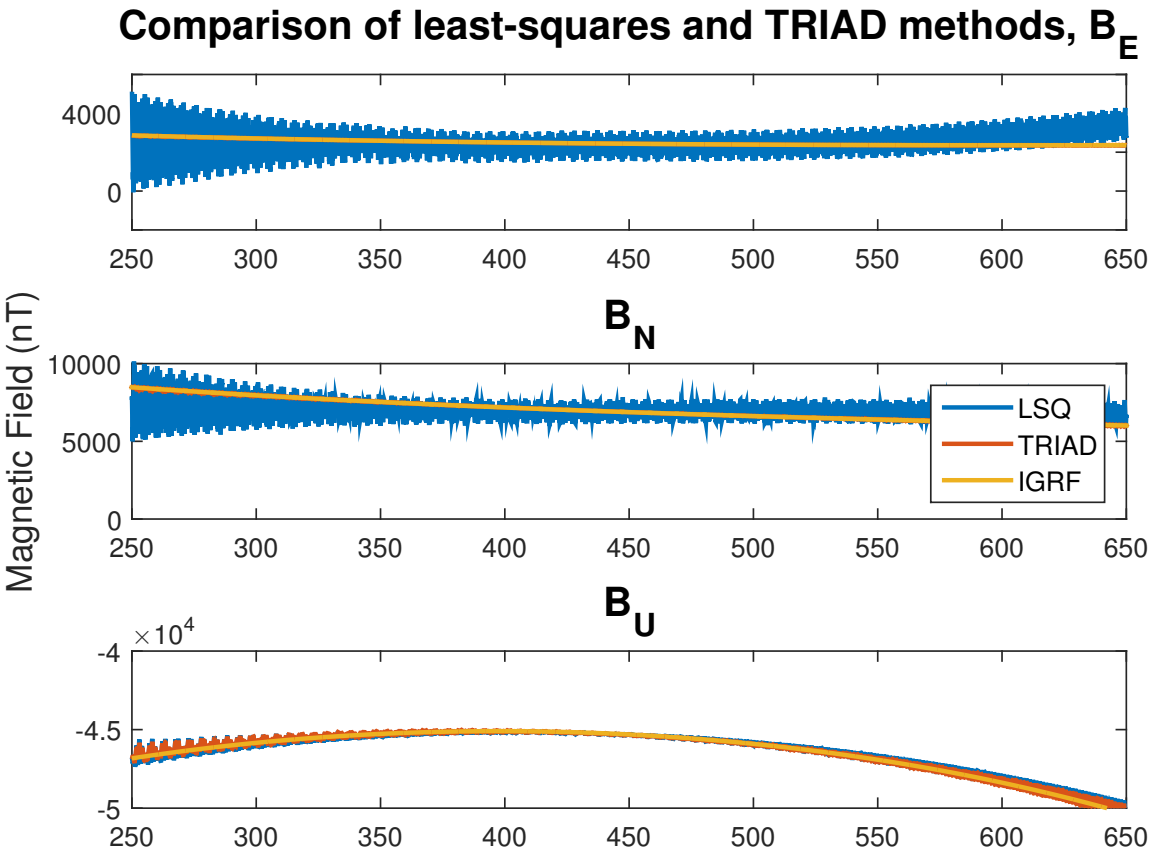

Fig. 5.12: Subpayload #4 TRIAD method comparison: B-field

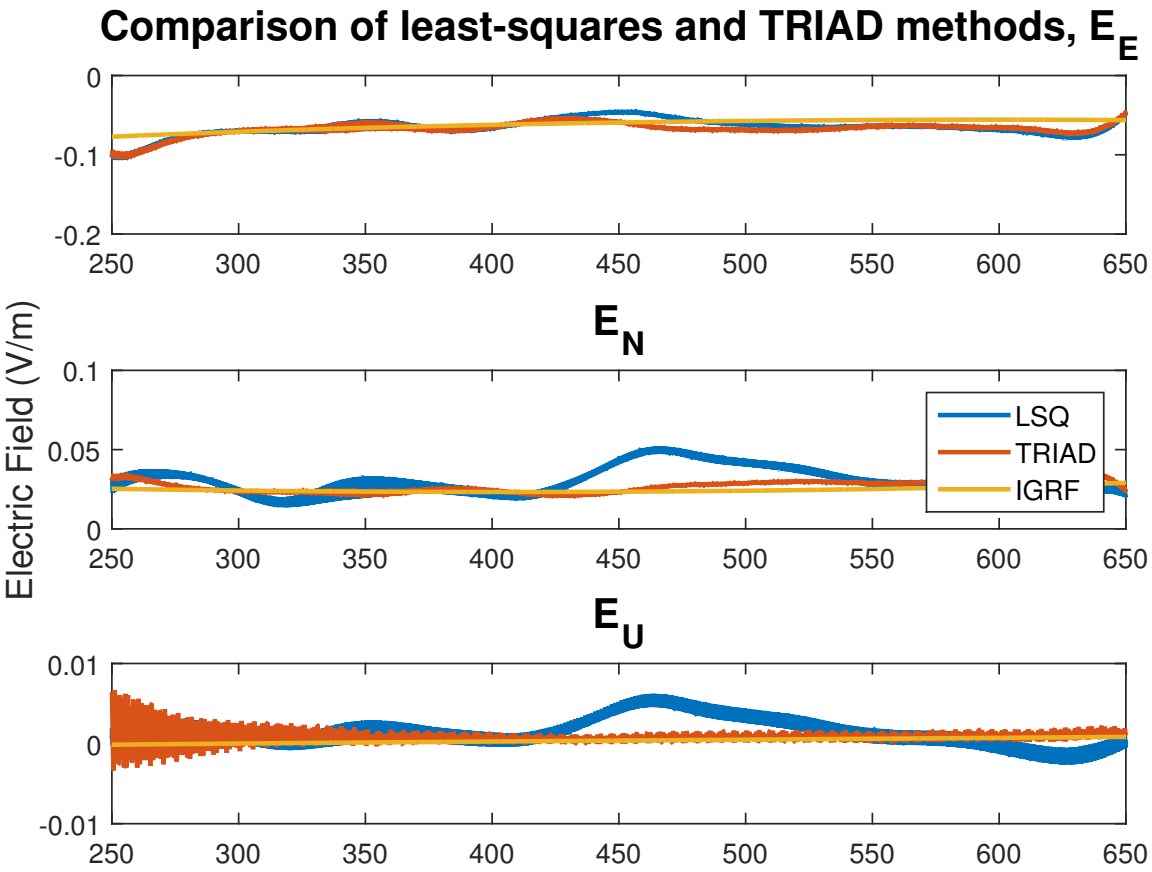

Fig. 5.13: Subpayload #4 TRIAD method comparison: E-field

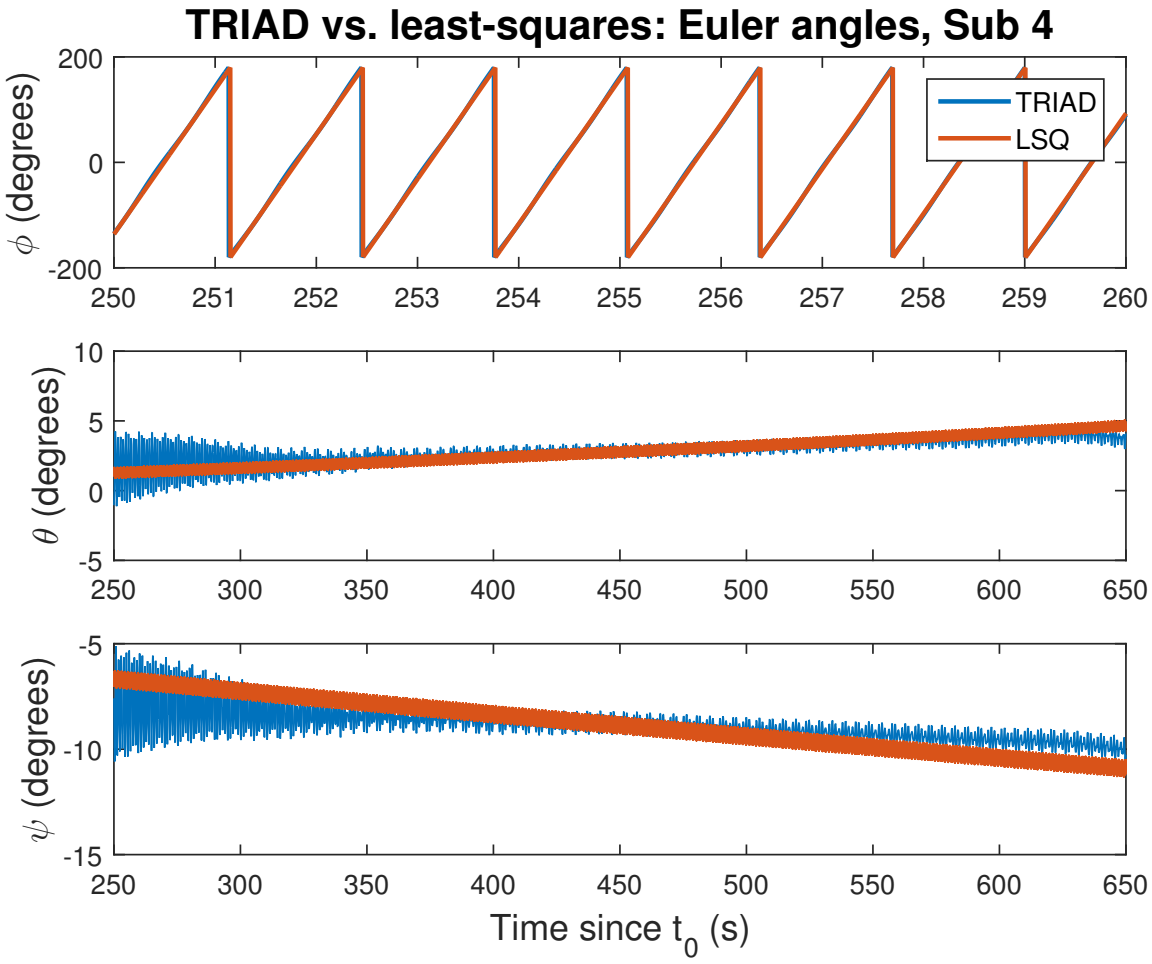

Fig. 5.14: Main payload TRIAD method angle comparison

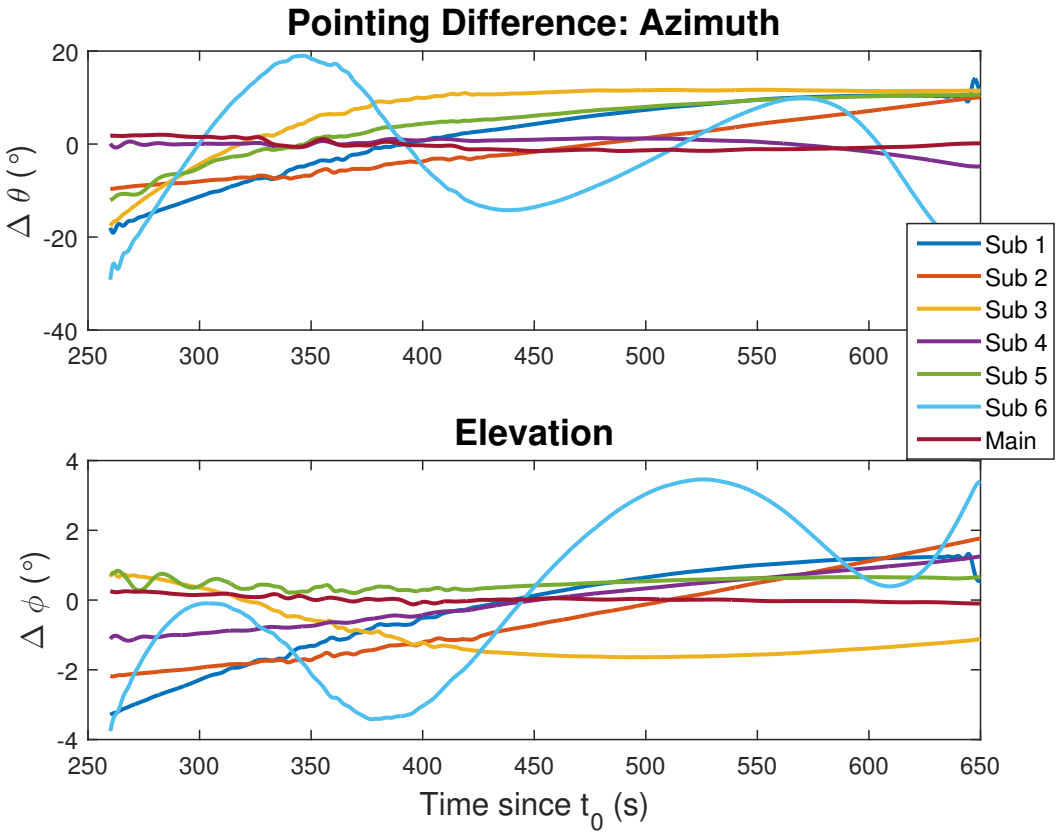

Fig. 5.15: Magnetic field pointing differences: least-squares

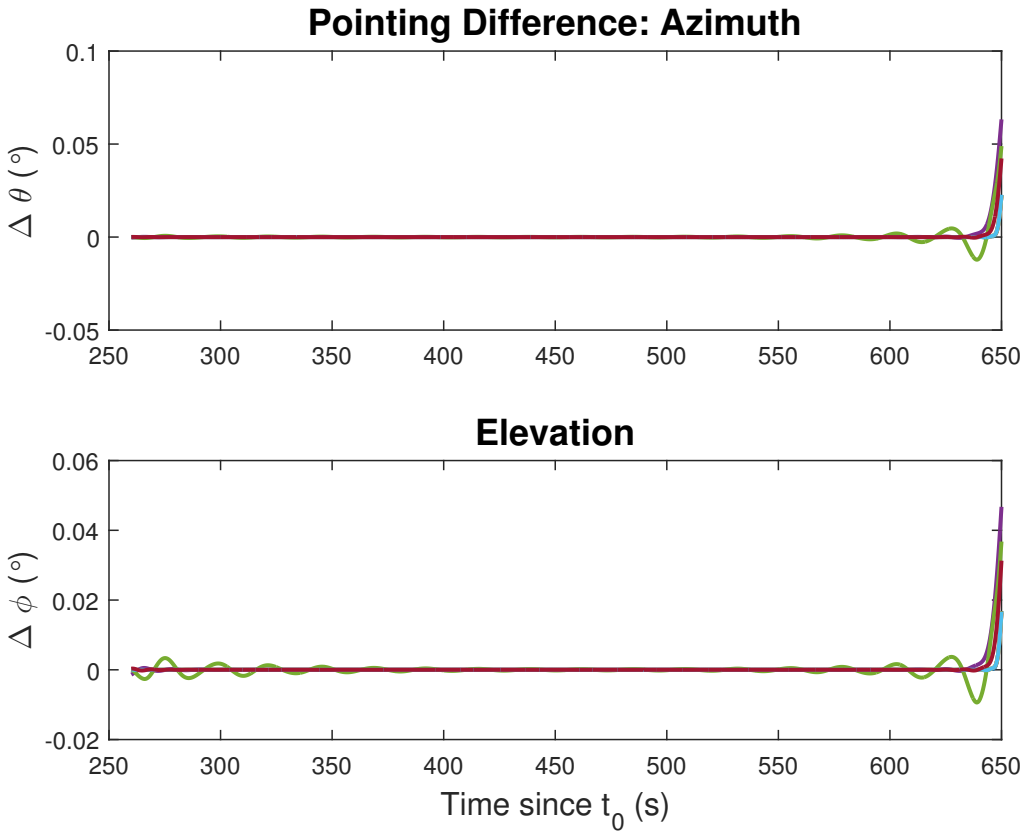

Fig. 5.16: Magnetic field pointing differences: TRIAD

5.4 Discussion on Results

Overall, the TRIAD method fit the subpayloads much better than the main payload. However, neither the new method nor TRIAD performed as well for any of the subpayloads as the new method did for the main payload. There are several hypotheses that may explain part or all of this result:

1. physical model inadequacies
2. increased calibration error for the subpayloads
3. subpayload alignment with the magnetic field
4. magnetic moment present on the spacecraft.

These are discussed in the sections below. Regardless of the results, pointing errors will be found in each direction using filtered, transformed measurements and the IGRF model as truth, which will indicate the magnitude of plausible errors (though not the true error, since the model field is not an adequate truth model). If the errors are sufficiently small ($< 5^\circ$ is desired, $< 10^\circ$ is acceptable for the ASSP science goals), then the attitude solution is acceptable, and by inference, a magnetic moment at least contributes to the existence of strong mechanical frequencies in the transformed measurements.

5.4.1 Physical Model Inadequacies

Simplifying assumptions were made in the construction of the physical model. The assumption was made that the shortness of the flexible wire booms and the time allotted to allow damping was sufficient to make a rigid-body assumption of the spacecraft. This may simply not be true. However, further investigation through ground-based experiments would be required to verify the validity of this assumption. The effects of this would not necessarily be a failing of the new method itself, since it will allow any desired physical model and estimate the relevant input parameters.

Perhaps a more important failing of the physical model in this usage is the modeling of the electric field. The magnetic field can be sufficiently modeled for the purposes of the attitude estimation, but only the velocity-induced term of the measured electric field can

be modeled with current knowledge. As ASSP flew through the plasma environment, the electrons and ions formed a plasma sheath around the payload and left a wake in its trail. It was intended that the electric field probe booms would extend far enough that the effects of the plasma sheath and wake would not be significant (figure 5.17), but the observed condition is that the booms were so short as to leave the electric field probes within the plasma sheath (see figure 5.18), except in the case of the main payload, subpayload #4 and perhaps subpayload #2.

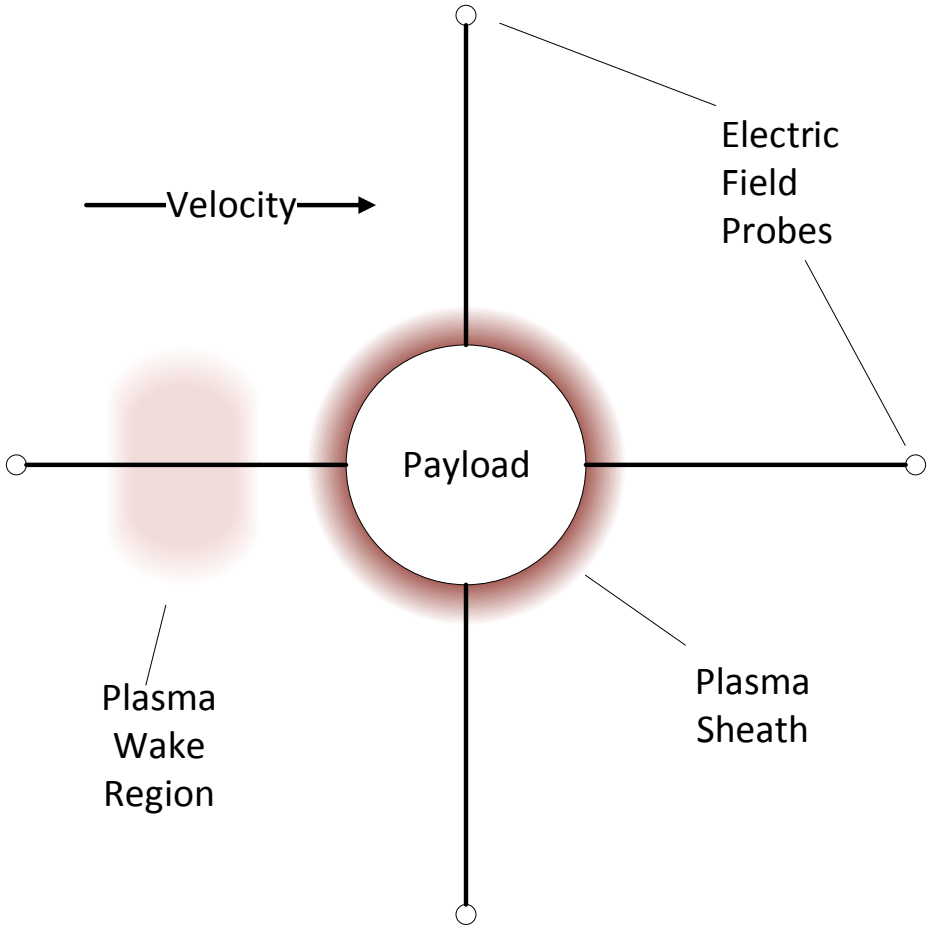

Fig. 5.17: Intended condition of deployed probes

As the payload spins, the effects of the plasma sheath and wake modulate the signal in addition to the modulation imposed by the spin alone. The digital filtering was an

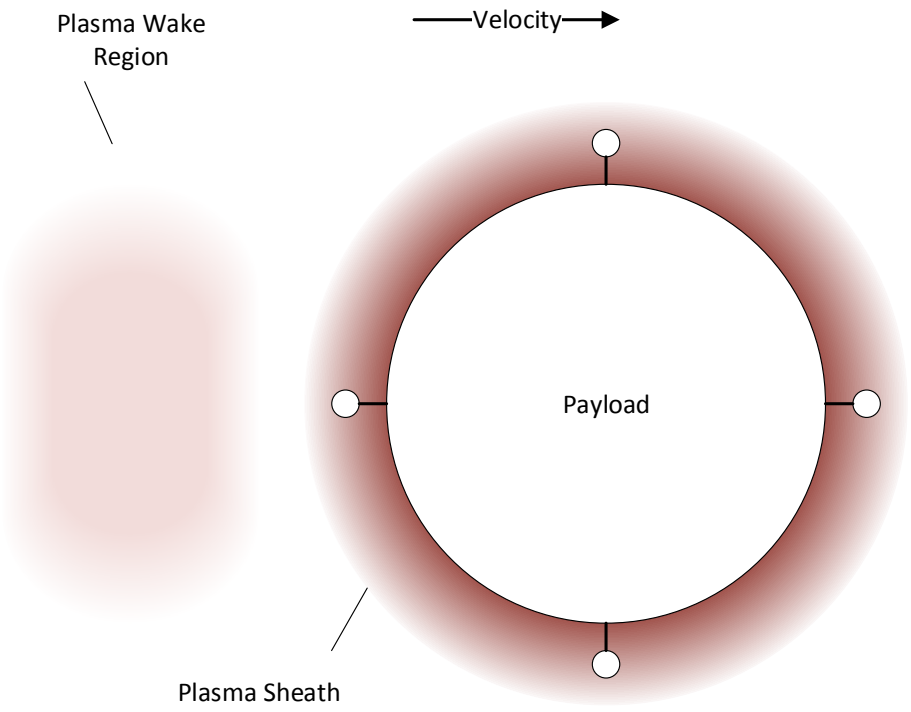

Fig. 5.18: Observed condition of deployed probes

effort to remove these effects and may have been largely successful, but it appears that the modulation of the measured electric field is different on the upleg of the flight than it is on the downleg. This caused an apparent change in phase, which offsets the azimuth dramatically for those payloads with shorter boom lengths, and are thus most strongly affected by the plasma sheath. The Langmuir probes on each payload could help characterize the plasma sheath, but such a study is itself another research topic, and is suggested as a future task in section 7.1.

Some evidence that supports this conclusion is found in comparing the waveforms of the predicted electric field measurements from the attitude solution for subpayload #1 and the actual, filtered measurements against which they were compared. Figure 5.19 shows these signals early in the flight, and figure 5.20 is the same from later in the flight. Focusing on the differences in phase rather than magnitude, we see that while early on the signals are well-matched in phase, later there is a shift, with the measurements now significantly leading the predictions. Since the electric field component measured is horizontal with respect to the ENU frame (see section 4.2.1), this may indeed correspond to change in azimuth angle seen in figure 5.15, though certainty in this conclusion would be difficult to obtain when considering all variables.

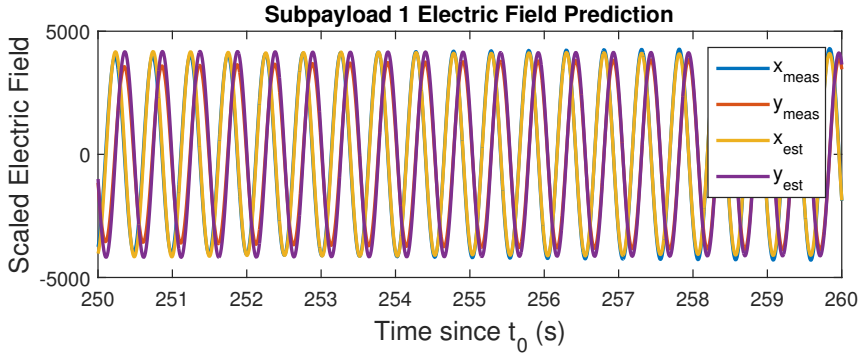

Fig. 5.19: Early E-field waveforms

5.4.2 Calibration Errors

With calibration, the electric field is known to within 10 mV (about 2%), which is

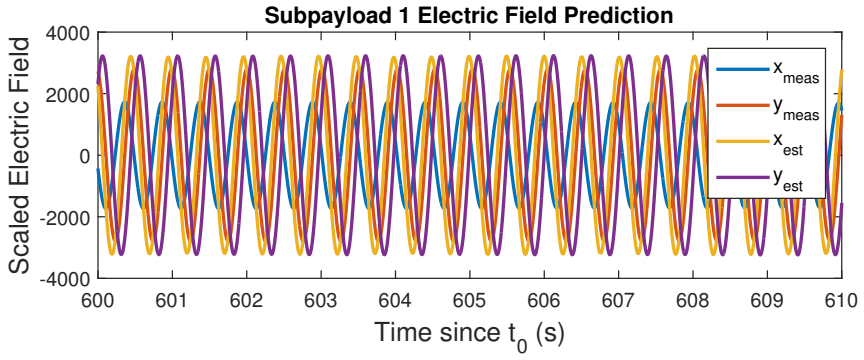

Fig. 5.20: Late E-field waveforms

probably sufficient. The magnetometic field has significantly higher calibration residuals, however: up to 2000 nT, depending on the payload. This may lead to significant errors in the attitude estimation regardless of method. A single bias term attempted to compensate for this, but is probably not sufficient to alleviate all errors in the attitude solution flowing from higher-order calibration errors. Improved calibration may be required for any improvement in attitude estimation.

5.4.3 Magnetic Field Alignment

In seeking differences between the main payload and the subpayloads, we see very different magnetometer trends through the flight (see figures B.1 and B.3). The spin-plane components of the magnetic field decrease in magnitude until they are nearly zero, then begin to increase again. This indicates an alignment of the payload with the magnetic field vector. The main payload is initially very well aligned, then slowly drifts away from alignment throughout the flight. In these two cases, differences in the model field may have very different effects when estimating the attitude of the payload, especially at a point of close alignment to the actual ambient field. This could explain why the new method converged to a less representative estimate of attitude.

5.4.4 Magnetic Moments

There is evidence that a magnetic moment biased the magnetometer measurements on

board the main payload. The same phenomenon may have occurred on the subpayloads, despite efforts taken to separate the magnetometer from the rest of the spacecraft with a boom. If this is the case, then the mechanical frequencies of each payload will remain present in the transformed magnetometer measurements, regardless of the accuracy of the attitude solution. This is a likely case; however, the varying qualities of the attitude history estimates of the payloads indicates that it is not likely that magnetic moments can account for all of the artifacts seen in the transformed measurements.

Chapter 6

Magnetic Field Observations

As with the attitude estimation results, there is a large number of descriptive figures, and the entire set can be found in appendix B, while a selection will accompany the text.

6.1 IGRF Comparison

The difference field (figure 6.1) shows some agreement between the payloads in trend and magnitude, but to infer more detailed information about the low-frequency electromagnetic structure than has been done in the past (see section 2.1), better agreement must be had. The larger-than-expected differences are likely due to calibration errors. We also see that subpayload #6 has a poor trend compared to the rest due to errors in its attitude history estimate. If an improved calibration is obtained, then a study of the differences between the payloads can reveal more detailed information about the low-frequency electromagnetic structures in the aurora.

6.2 Magnetic Perturbations

Following the process described in 4.6, the measurements from each of the subpayloads were processed, and the perturbation field is plotted in figure 6.2. We immediately see the effects of the inaccuracies of the attitude estimate for subpayload #6. This must be corrected before the measurements for that payload can be used to make detailed inferences about the auroral electromagnetic environment. Similar non-physical structure is seen in the Up component for subpayload #1.

For the rest of the payloads and components, we see that they are qualitatively very similar in structure. As the payloads pass through the auroral arc at slightly different points, the local magnetic field is also perturbed in slightly different ways. Treating the

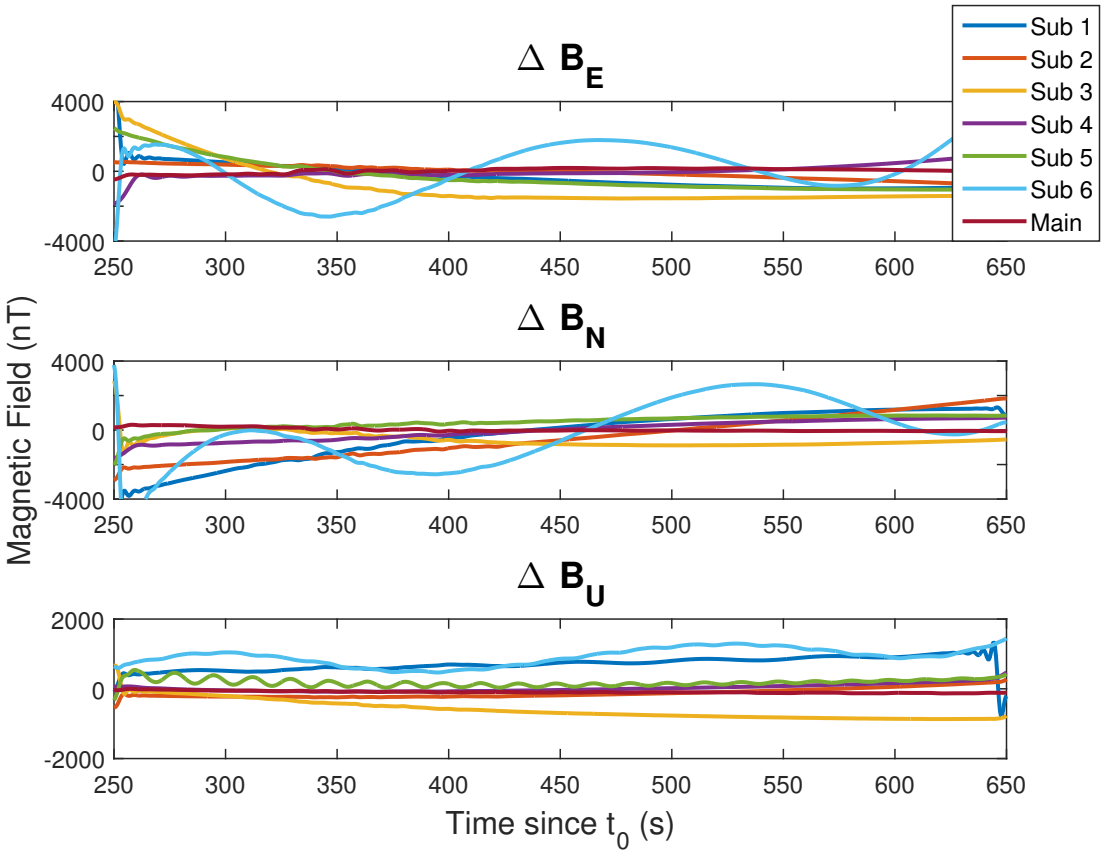

Fig. 6.1: Magnetic difference field

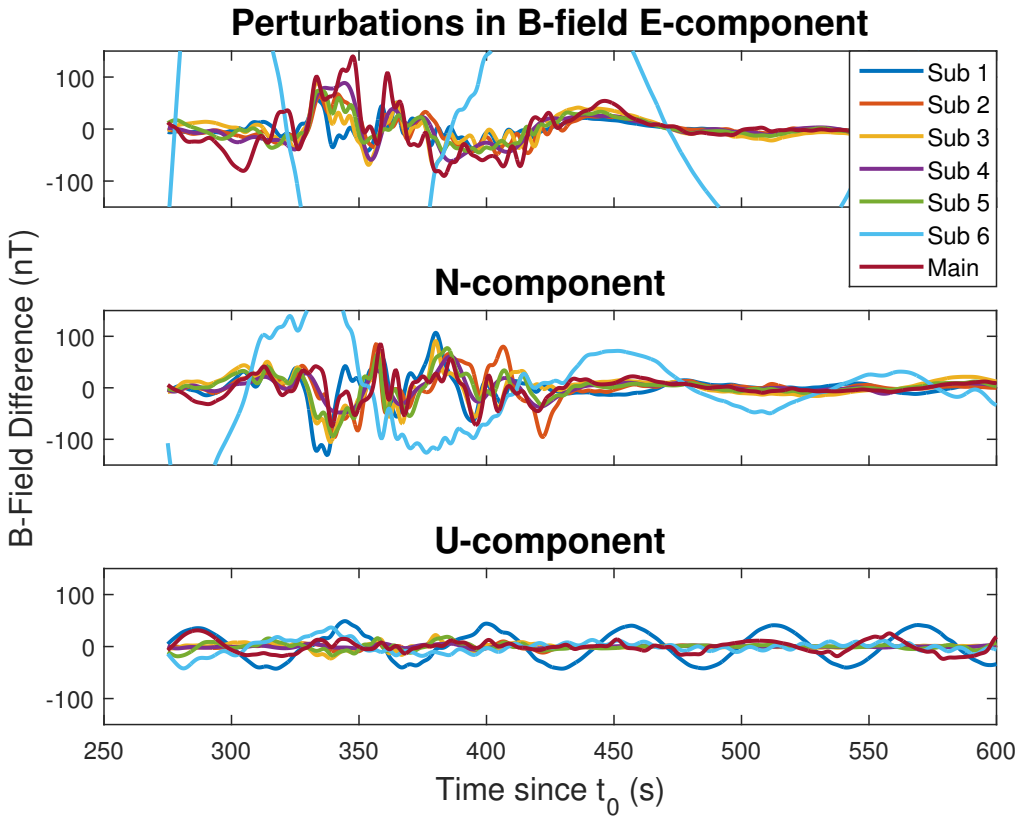

Fig. 6.2: Perturbations in the magnetic field

measurement of each payload individually or as a whole, the structures are very similar to those seen in [4]. We see that most of the magnetic perturbations are in the East and North directions, which agrees with a simple Birkeland current model of a field-aligned current. Judging by the latter part of the flight when perturbations have largely ceased, the noise floor is about 10 nT. Subpayloads #2 and #4a and the main payload have acceptable attitude solutions, and their measurements should be usable in a detailed scientific study of the aurora, which meets the objective of this thesis. Measurements from the other payloads may use their respective attitude solutions for qualitative science, or they may be suitable for single-point current models.

Chapter 7

Conclusions

A unique method to estimate the attitude history of a spacecraft has been developed using nonlinear least-squares to determine parameter inputs to a kinematic physical model, which defines the possible motions of the spacecraft. This method has been shown to be capable of producing an attitude history estimate as accurate as that provided by inertial sensors when applied to the main ASSP payload. This attitude solution was used to determine the attitude of all of the deployed payloads for ASSP, proving to be more appropriate than the TRIAD method and scientifically sufficient in the case of the main payload and subpayloads #2 and #4 The limiting factors of the method in this case are most likely modeling errors (which could alternatively be considered a measurement quality issue, since the additional modeling terms should have been unnecessary), and instrument calibration.

Using the attitude solution and additional signal processing, the high- and low-frequency magnetic difference fields have been obtained. The result of this is a sensitive multi-point simultaneous sampling of the magnetic field from which inferences may be made concerning the auroral current structures and energy flow. Structures in the difference fields are observed to have similar features to difference fields obtained by other measurement campaigns [1] [4].

7.1 Future Work

The breadth and depth of possibilities derived from this work are vast. Some of the most potentially impactful tasks that could further the pursuits of this work are listed below:

1. Compare the attitude solution to that produced by a Kalman Filter
2. Determine the mathematical properties of the attitude estimation method for comparison to other optimal estimation methods
3. Characterize magnetic moments on each of the payloads to improve measurement accuracy
4. Use Langmuir probe observations to characterize the plasma sheath and improve vector measurements
4. Model the current structures in the aurora using the magnetic field observations
5. Test the new attitude estimation method on other spacecraft
6. Improve the calibration of the ASSP magnetometers

References

[1] Park, R. J. and Cloutier, P. A., "Rocket-Based Measurement of Birkeland Currents Related to an Auroral Arc and Electrojet," *Journal of Geophysical Research*, Vol. 76, 1971, pp. 7714–7732.

[2] Yasuhara, F., Kamide, Y., and Akasofu, S. I., "Field-Aligned and Ionospheric Currents," *Planetary and Space Sciences*, Vol. 23, 1975, pp. 1355–1368.

[3] Robinson, R. M., Bering, E. A., Vondrak, R. R., Anderson, H. R., and Cloutier, P. A., "Simultaneous Rocket and Radar Measurements of Currents in an Auroral Arc," *Journal of Geophysical Research*, Vol. 86, 1981, pp. 7703–7717.

[4] Zheng, Y., Lynch, K. A., Boehm, M., Goldstein, R., Javadi, H., Schuck, P., Arnoldy, R. L., and Kintner, P. M., "Multipoint measurements of field-aligned current density in the auroral zone," *Journal of Geophysical Research*, Vol. 108, 2003, pp. 1217–1236.

[5] Robinson, R. M., *Simultaneous ground and rocket based measurements of electric fields and currents in an auroral arc*, Ph.D. thesis, Rice University, Houston, TX, 1980.

[6] Black, H. D., "A Passive System for Determining the Attitude of a Satellite," *AIAA Journal*, Vol. 2, 1964, pp. 1350–1351.

[7] Markley, F. L., "Attitude Determination Using Vector Observations: A Fast Optimal Matrix Algorithm," *The Journal of the Astronautical Sciences*, Vol. 41, 1993, pp. 261–280.

[8] Wahba, G., "A Least-Squares Estimate of Spacecraft Attitude," *SIAM Review*, Vol. 7, 1965, pp. 409.

[9] Markley, F. L., "Attitude Determination Using Vector Observations and the Singular Value Decomposition," *The Journal of the Astronautical Sciences*, Vol. 38, 1988, pp. 245–248.

[10] Keat, J. E., "Analyisis of Least-Squares Attitude Determination Routine DOAOP," Feb. 1977, Official Report.

[11] Shuster, M. D. and Oh, S. D., "Three-Axis Attitude Determination from Vector Observations," *Journal of Guidance and Control*, Vol. 4, 1981, pp. 70–77.

[12] Bar-Itzhack, I. Y., "REQUEST: a Recursive QUEST Algorithm for Sequential Attitude Determination," *Journal of Guidance, Control, and Dynamics*, Vol. 19, 1996, pp. 1034–1038.

[13] Choukroun, D., *Novel Methods for Attitude Determination Using Vector Observations*, Ph.D. thesis, Technion - Israel Institute of Technology, Haifa, Israel, 2003.

[14] Curtis, H. D., *Orbital Mechanics for Engineering Students*, Butterworth-Heinemann, Waltham, MA, 2009.

[15] "6DOF ECEF (Quaternion): Implement quaternion representation of six-degrees-of-freedom equations of motion in Earth-centered Earth-fixed (ECEF) coordinates," *MATLAB* Help File.

[16] Stevens, B. L. and Lewis, F. L., *Aircraft Control and Simulation*, John Wiley & Sons, Hoboken, NJ, 2003.

[17] McFarland, R. E., "A Standard Kinematic Model for Flight Simulation at NASA-AMES," Jan. 1975, Official Report.

[18] "Supplement To Department of Defense World Geodetic System 1984 Technical Report Methods, Techniques, and Data Used in WGS 84 Development," Dec. 1987, Official Report.

[19] Macmillan, S., "IGRF10 Model Coefficients for 1945-2010," 2005.

[20] Compston, D., "International Geomagnetic Reference Field (IGRF) Model," 2011.

[21] Coleman, T. F. and Li, Y., "An Interior, Trust Region Approach for Nonlinear Minimization Subject to Bounds," *SIAM Journal on Optimization*, Vol. 6, 1996, pp. 418–445.

[22] "lsqnonlin: Solve nonlinear least-squares (nonlinear data-fitting) problems," *MATLAB* Help File.

[23] "lsqcurvefit: Solve nonlinear curve-fitting (data-fitting) problems in least-squares sense," *MATLAB* Help File.

[24] Smith, C., "Postflight Attitdue Determination Talos-Terrier-Oriole-Nihka 49.002 (Swenson, PFRR)," April 2015, Official Report.

Appendices

Appendix A

Complete Attitude Estimation Results

A.1 Unfiltered Trend Comparisons

Magnetic Field

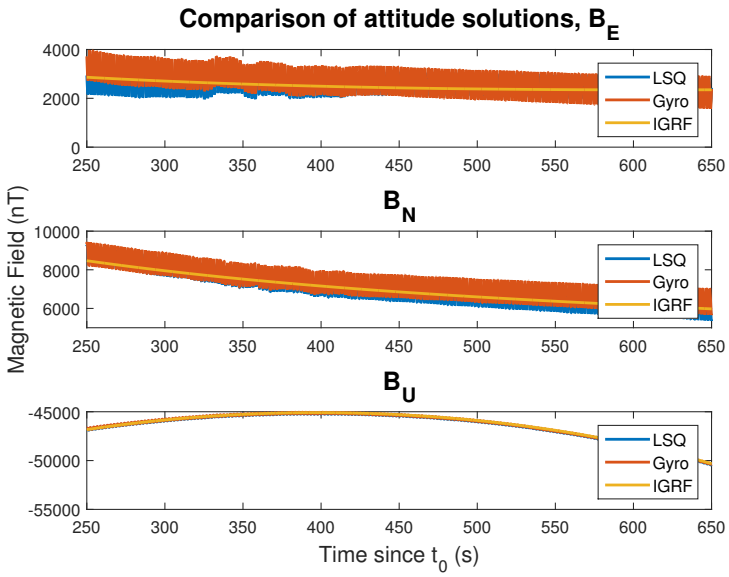

Fig. A.1: Main payload inertial attitude solution comparison

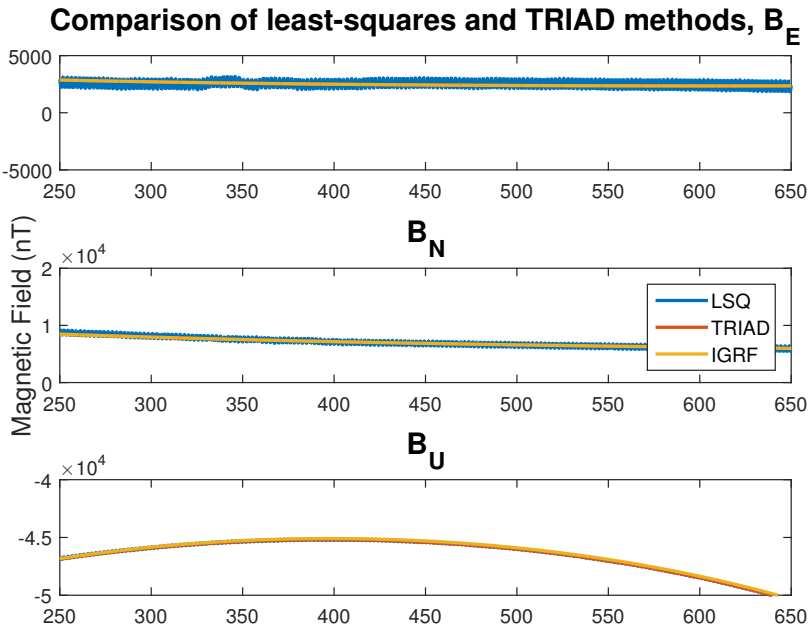

Fig. A.2: Main payload TRIAD method comparison

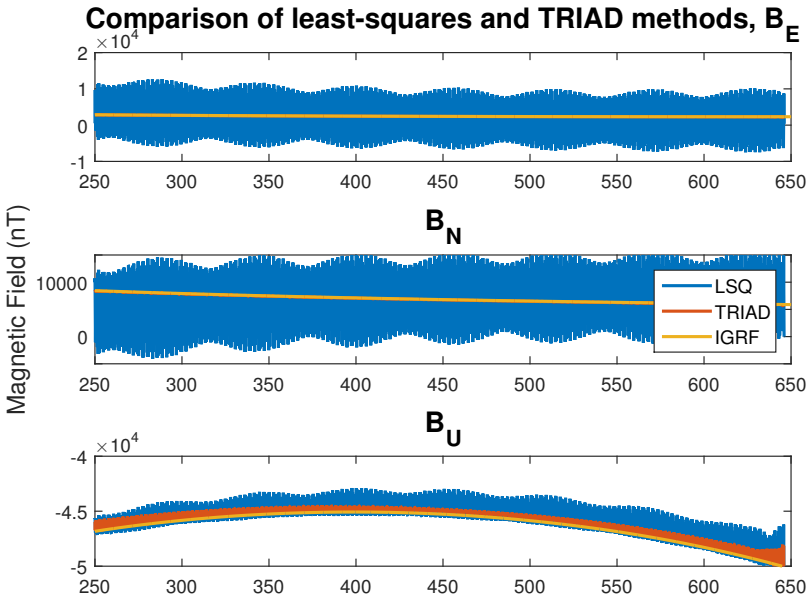

Fig. A.3: Subpayload #1 payload TRIAD method comparison

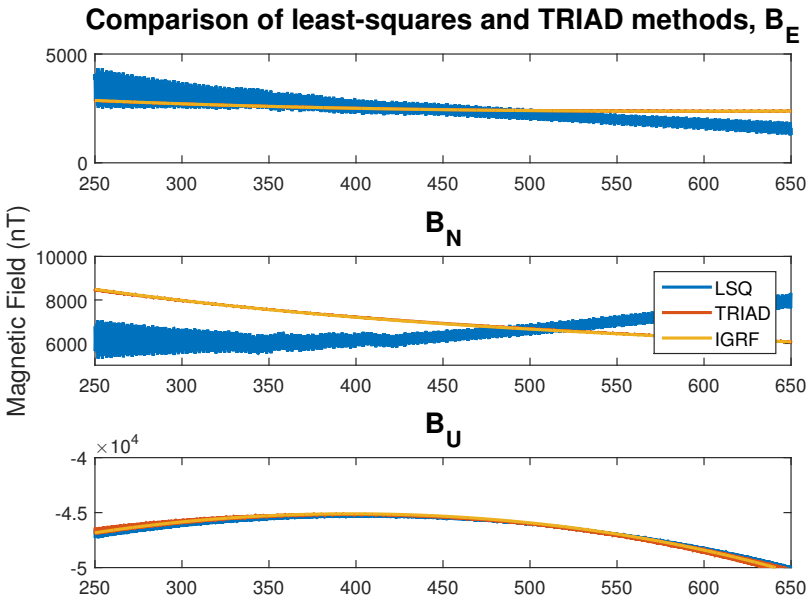

Fig. A.4: Subpayload #2 payload TRIAD method comparison

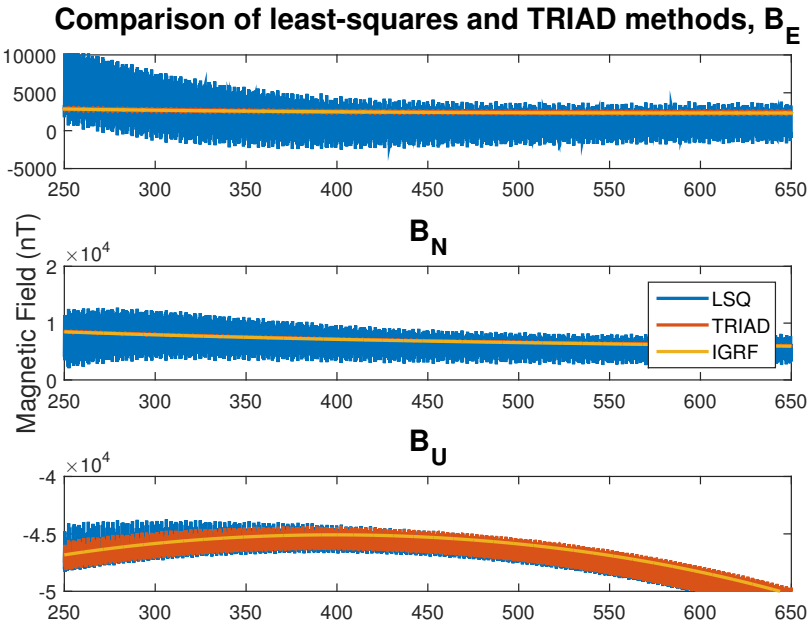

Fig. A.5: Subpayload #3 payload TRIAD method comparison

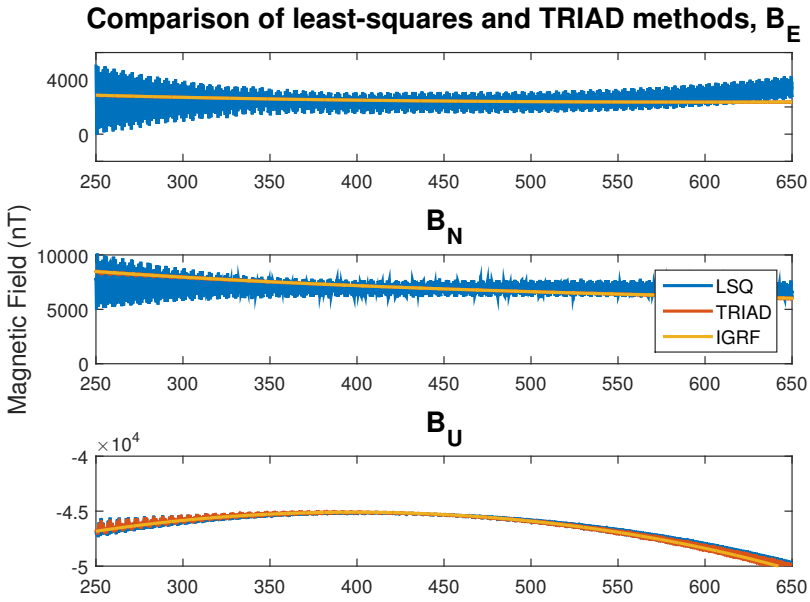

Fig. A.6: Subpayload #4 payload TRIAD method comparison

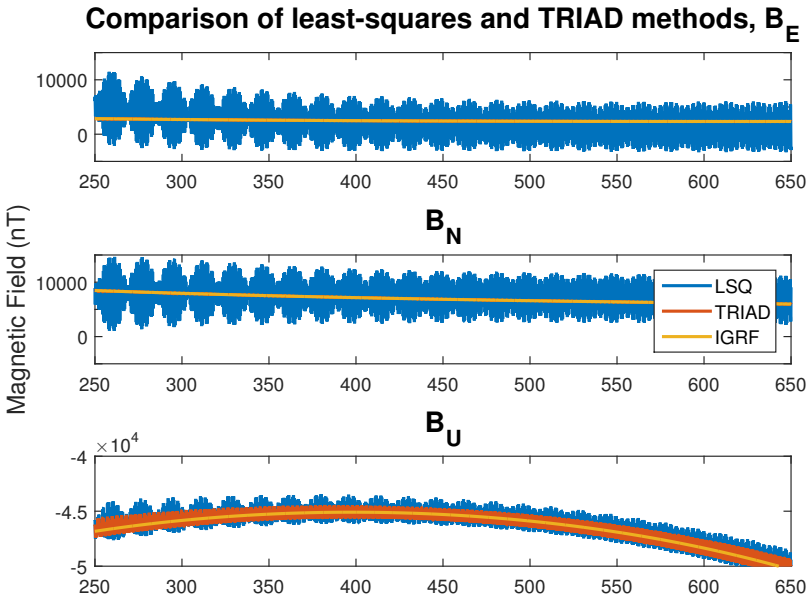

Fig. A.7: Subpayload #5 payload TRIAD method comparison

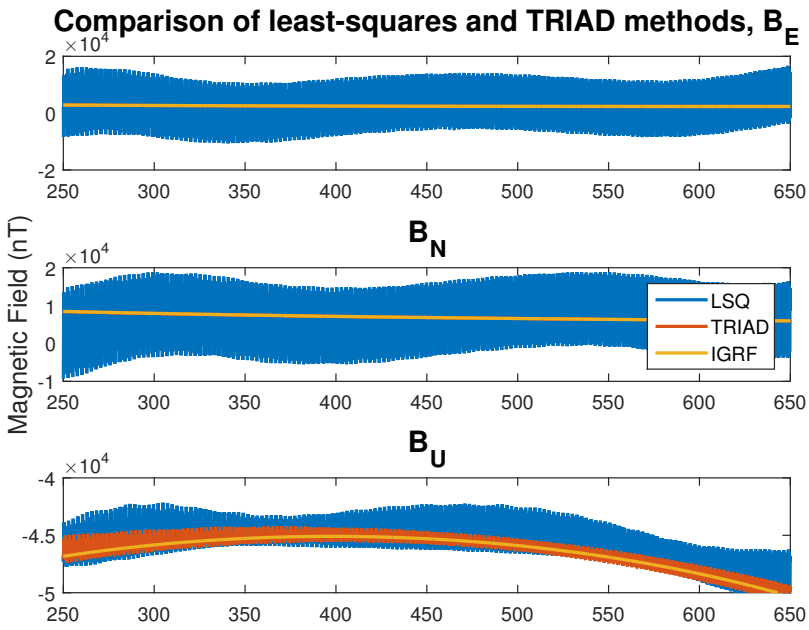

Fig. A.8: Subpayload #6 payload TRIAD method comparison

Electric Field

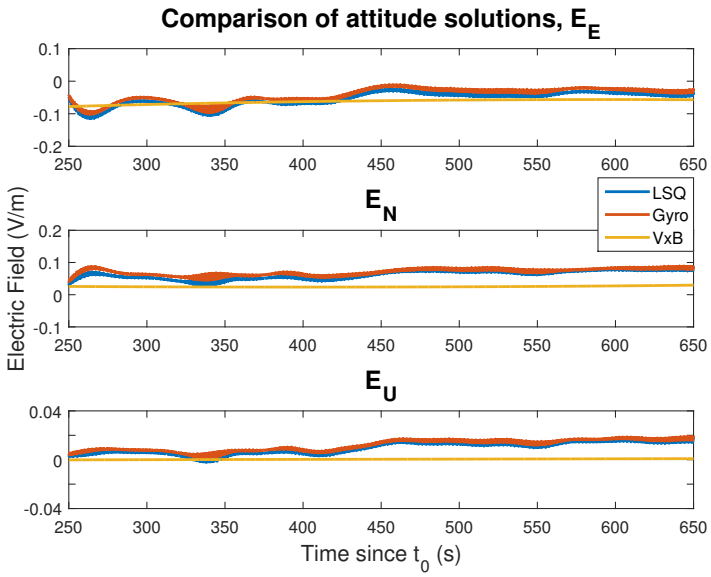

Fig. A.9: Main payload inertial attitude solution comparison

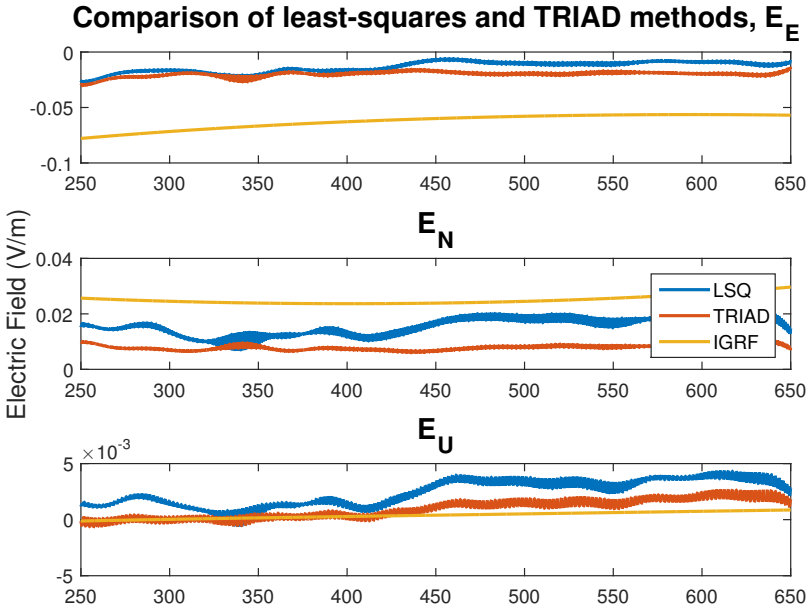

Fig. A.10: Main payload TRIAD method comparison

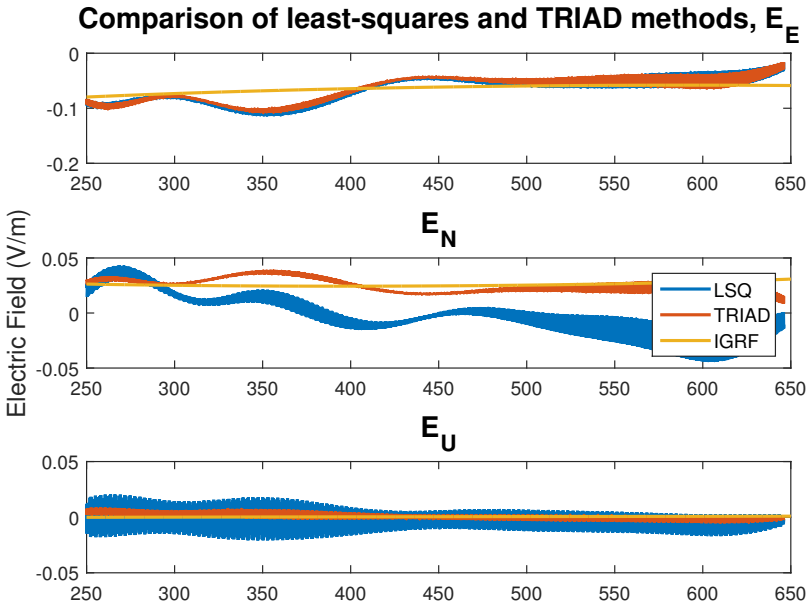

Fig. A.11: Subpayload #1 payload TRIAD method comparison

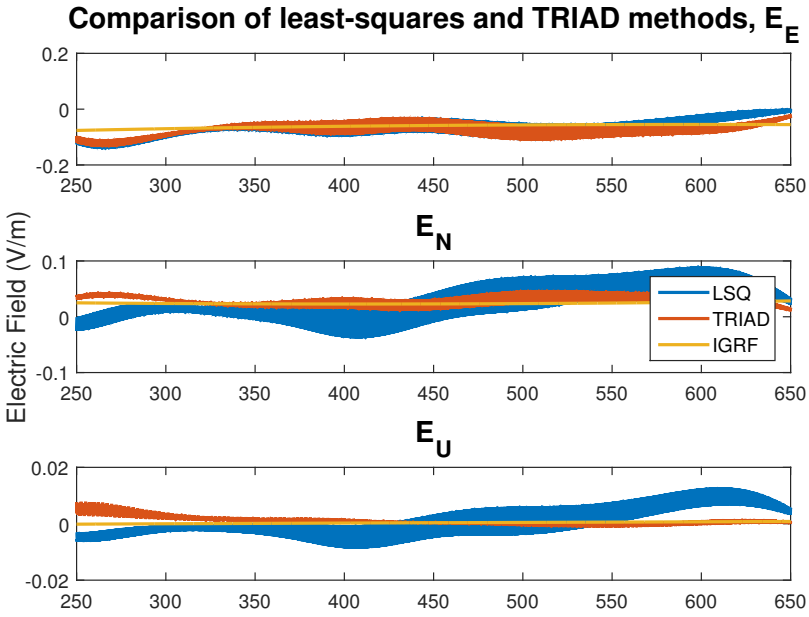

Fig. A.12: Subpayload #2 payload TRIAD method comparison

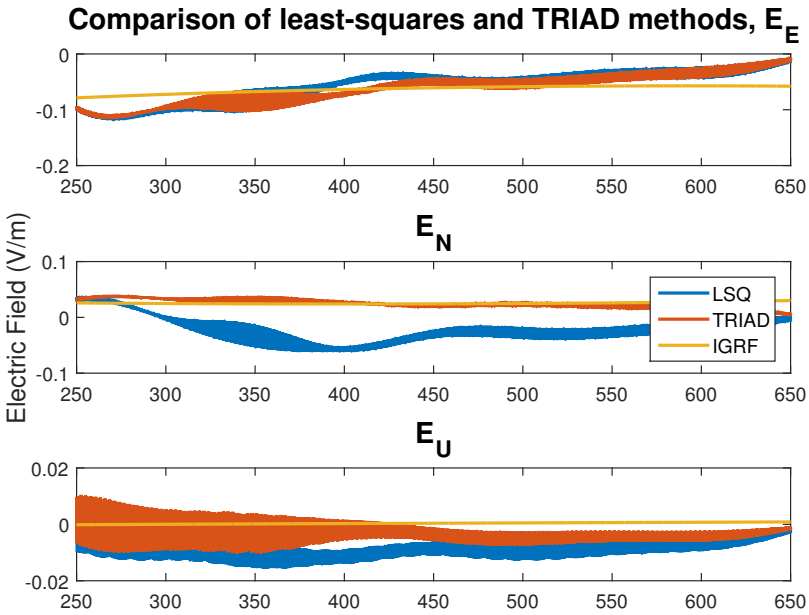

Fig. A.13: Subpayload #3 payload TRIAD method comparison

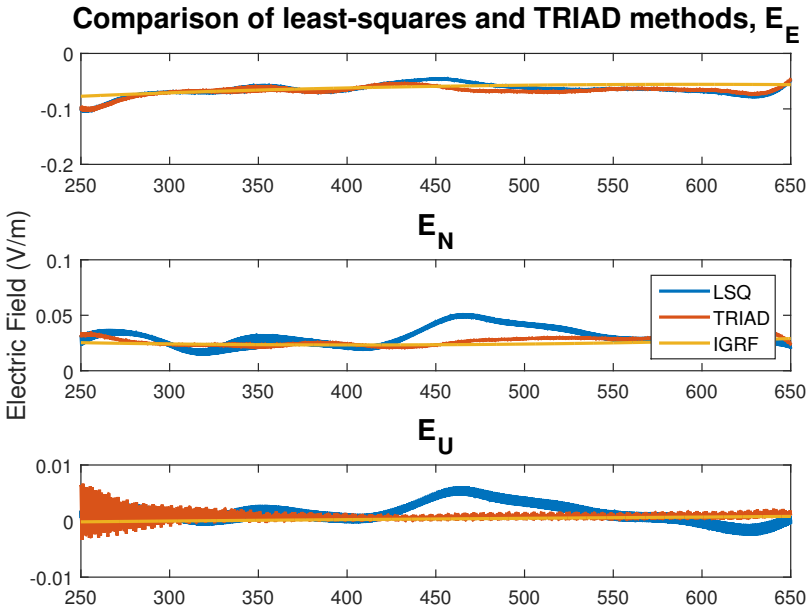

Fig. A.14: Subpayload #4 payload TRIAD method comparison

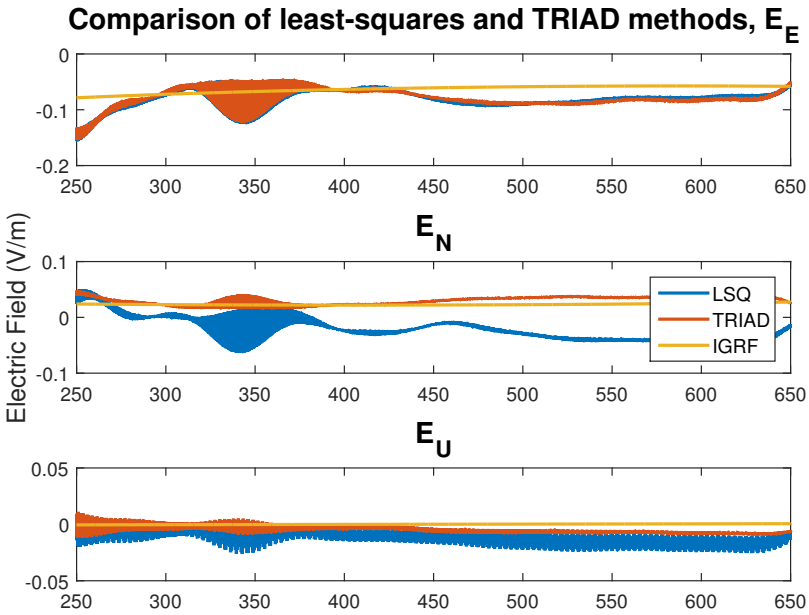

Fig. A.15: Subpayload #5 payload TRIAD method comparison

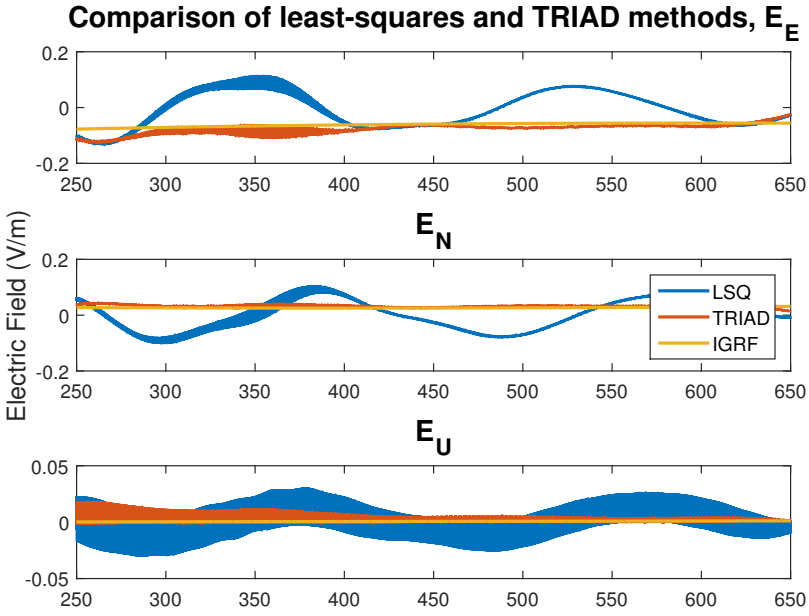

Fig. A.16: Subpayload #6 payload TRIAD method comparison

A.2 Filtered Trend Comparisons

Magnetic Field

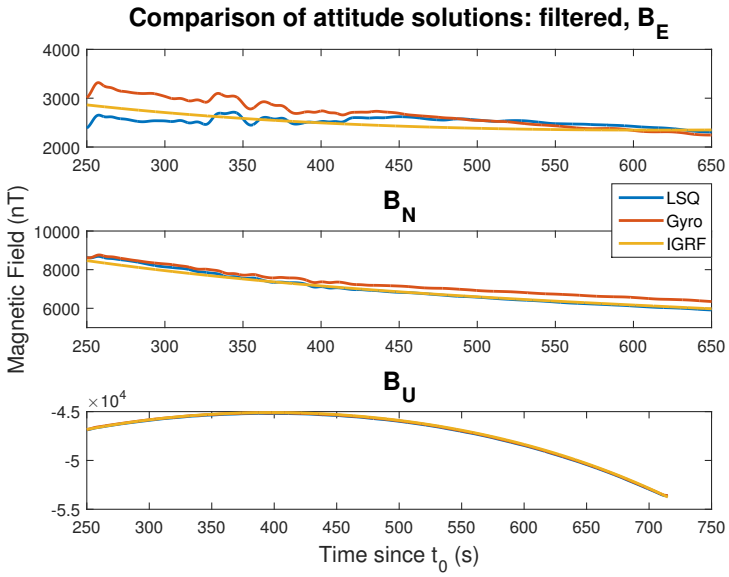

Fig. A.17: Main payload inertial attitude solution comparison

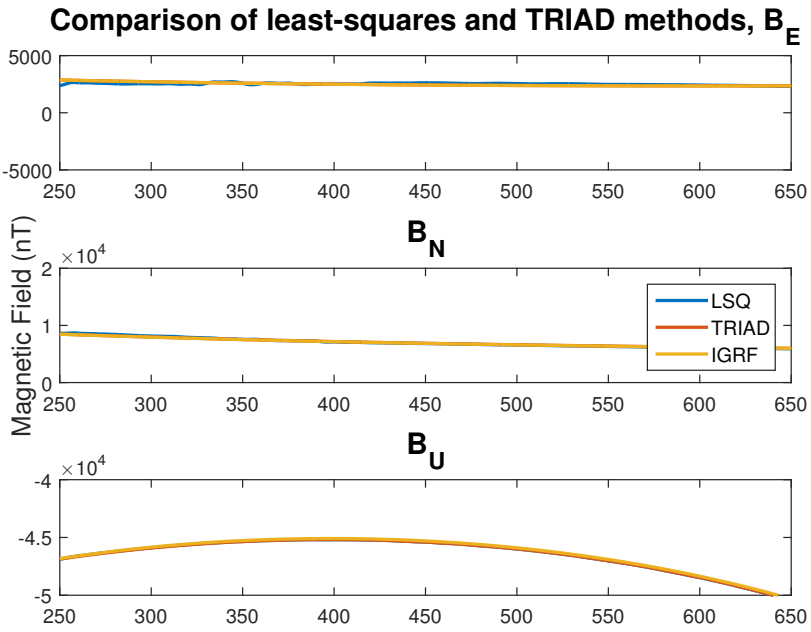

Fig. A.18: Main payload TRIAD method comparison

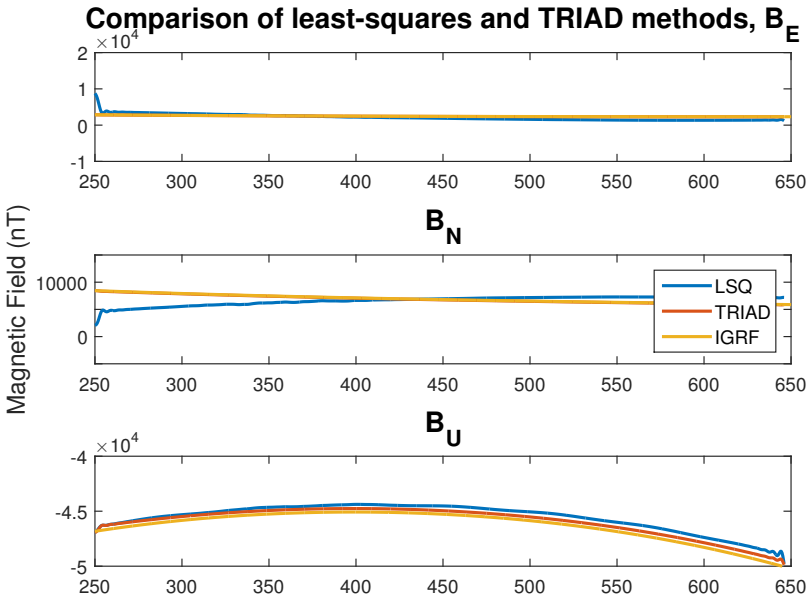

Fig. A.19: Subpayload #1 payload TRIAD method comparison

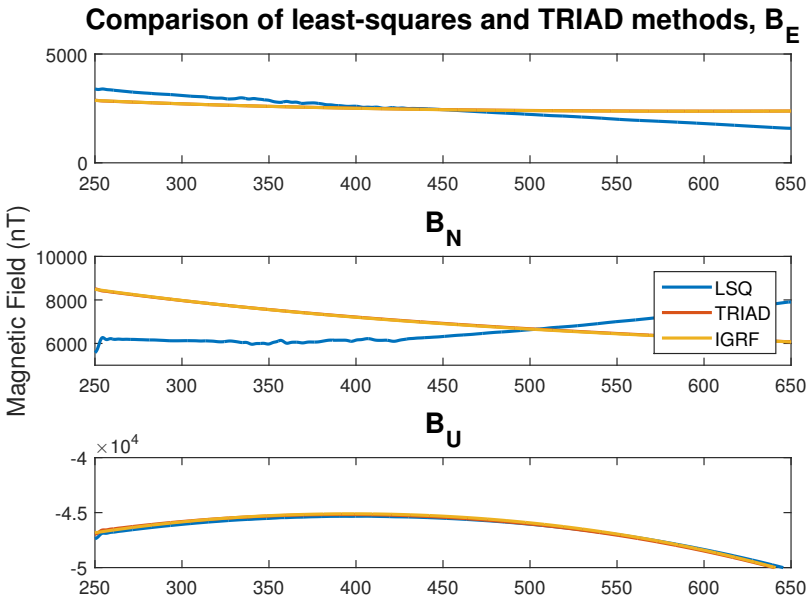

Fig. A.20: Subpayload #2 payload TRIAD method comparison

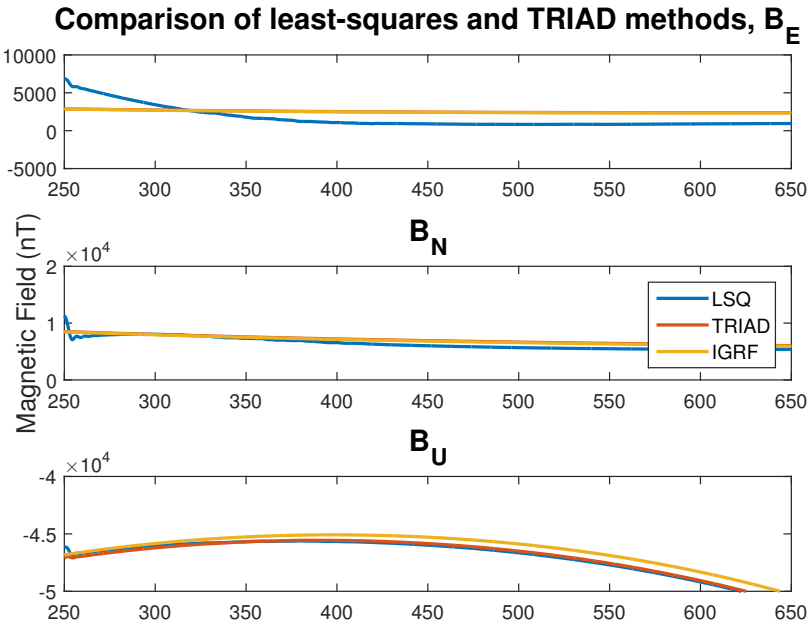

Fig. A.21: Subpayload #3 payload TRIAD method comparison

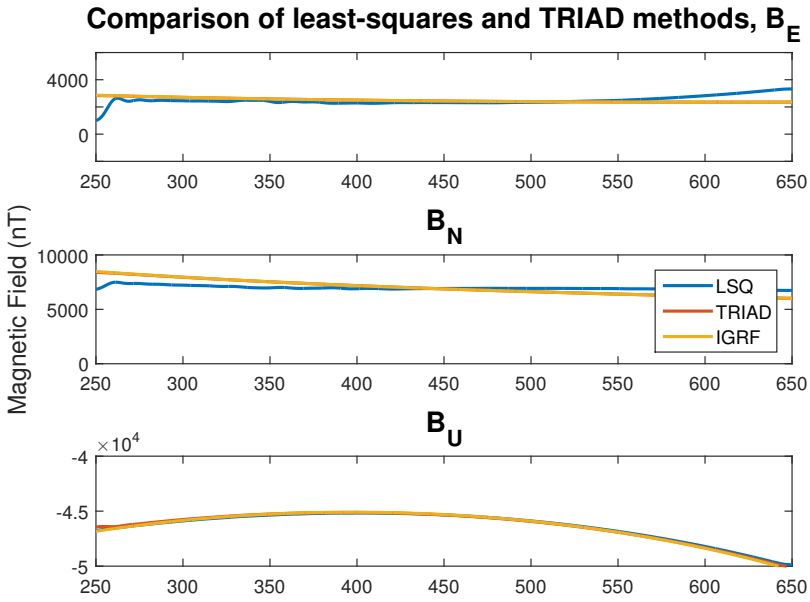

Fig. A.22: Subpayload #4 payload TRIAD method comparison

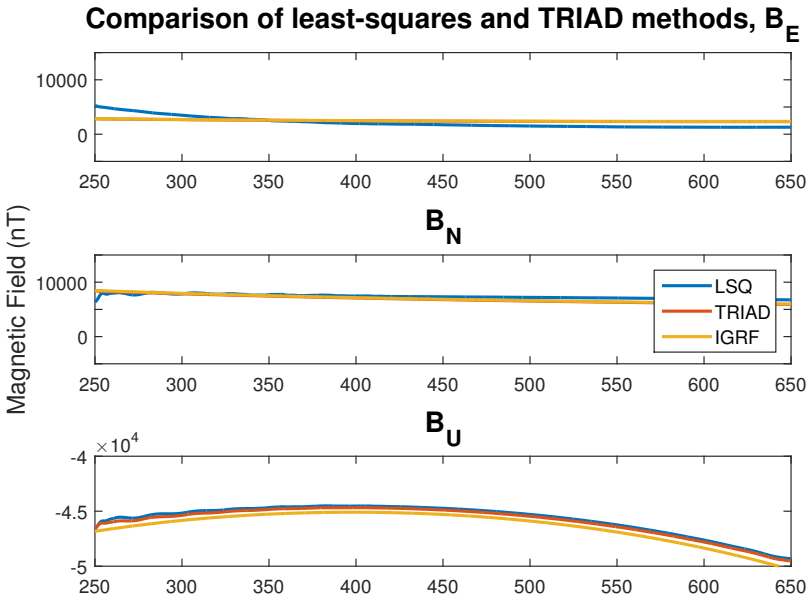

Fig. A.23: Subpayload #5 payload TRIAD method comparison

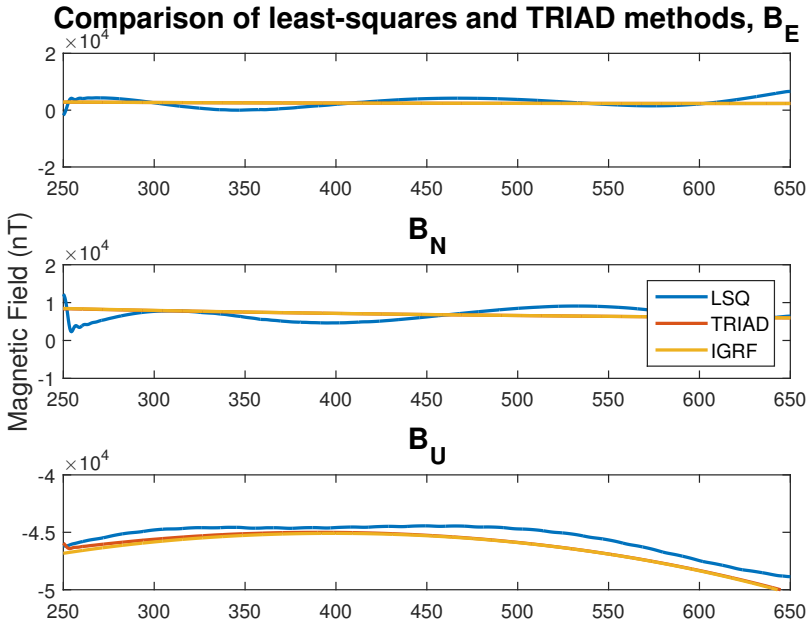

Fig. A.24: Subpayload #6 payload TRIAD method comparison

Electric Field

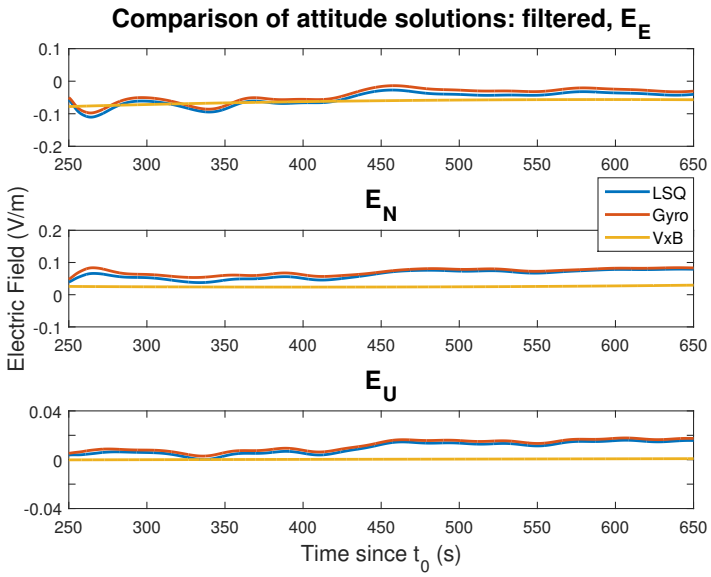

Fig. A.25: Main payload inertial attitude solution comparison

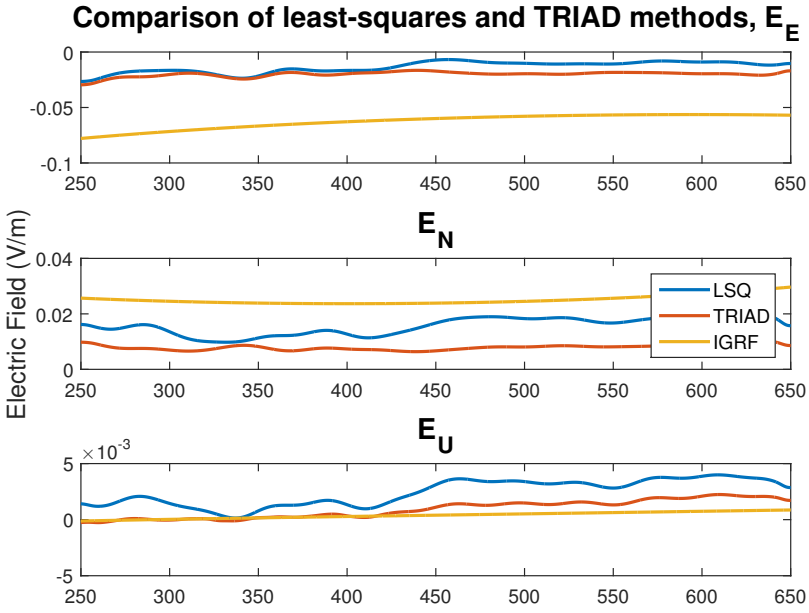

Fig. A.26: Main payload TRIAD method comparison

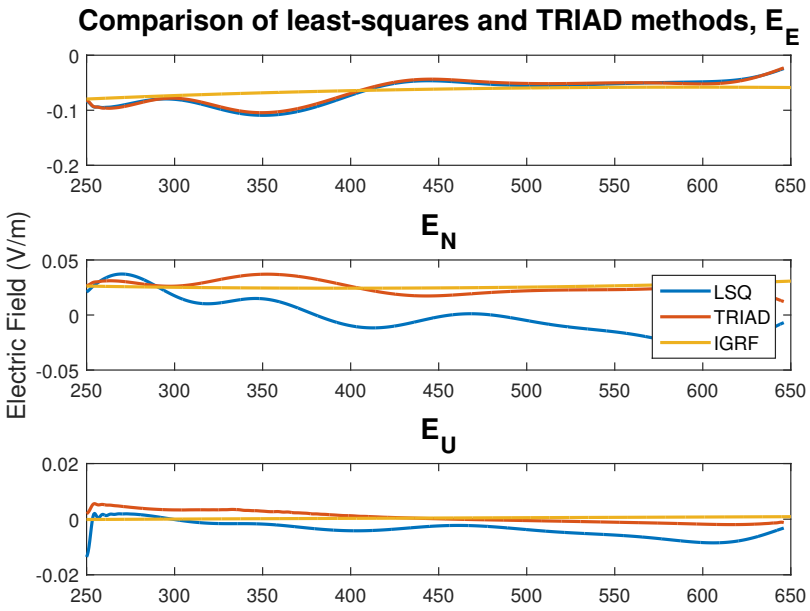

Fig. A.27: Subpayload #1 payload TRIAD method comparison

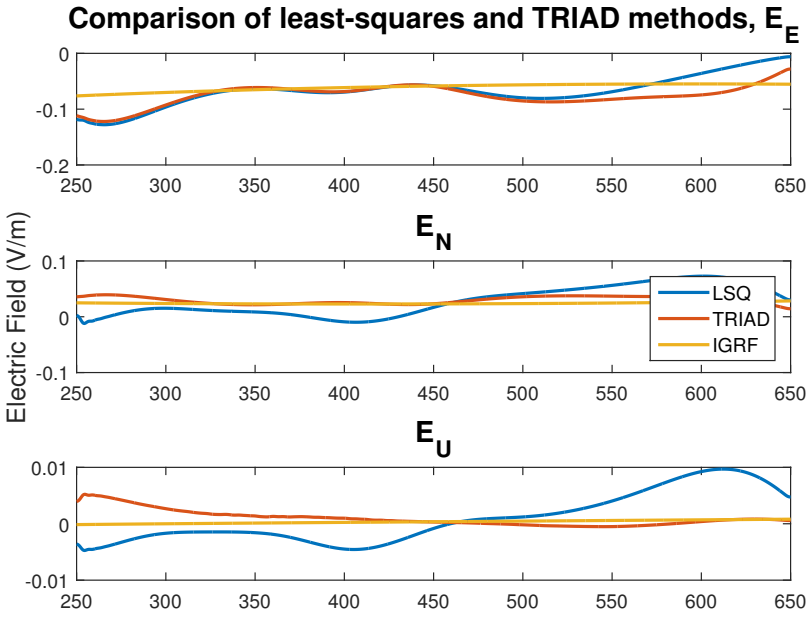

Fig. A.28: Subpayload #2 payload TRIAD method comparison

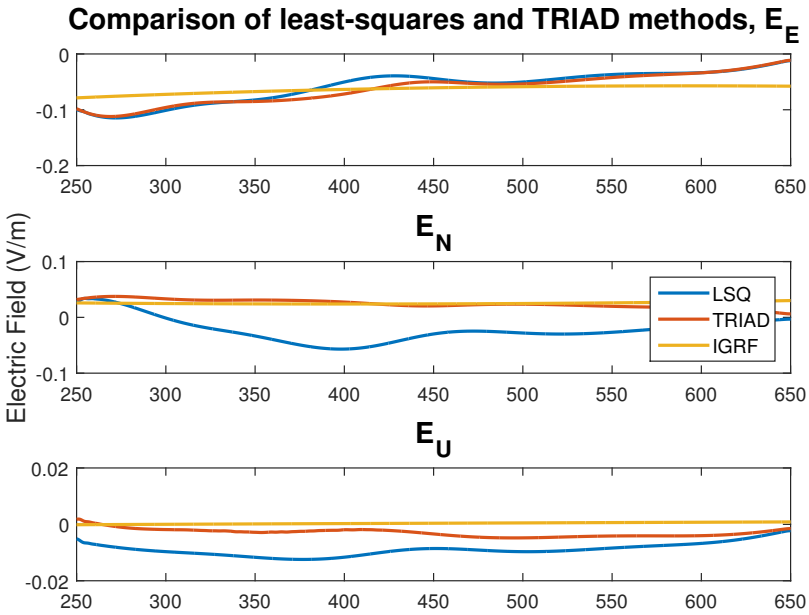

Fig. A.29: Subpayload #3 payload TRIAD method comparison

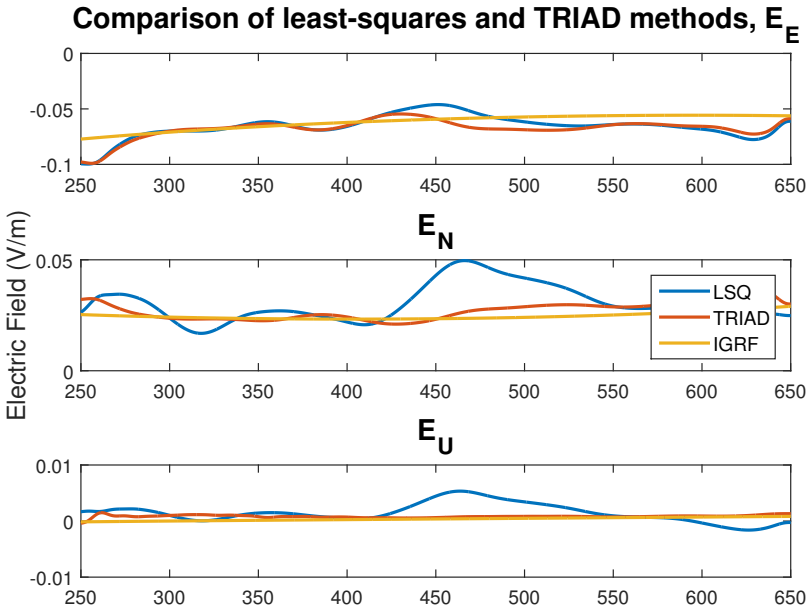

Fig. A.30: Subpayload #4 payload TRIAD method comparison

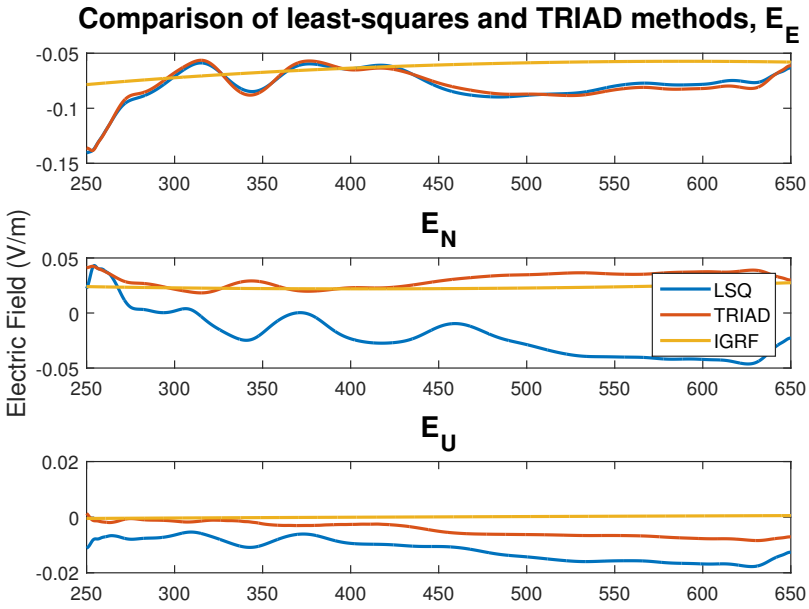

Fig. A.31: Subpayload #5 payload TRIAD method comparison

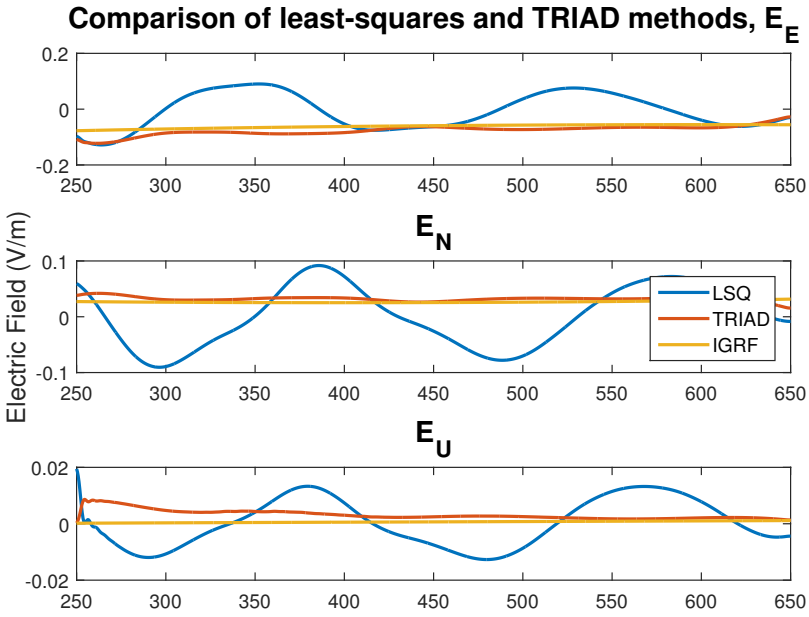

Fig. A.32: Subpayload #6 payload TRIAD method comparison

A.3 Euler Angle Comparisons

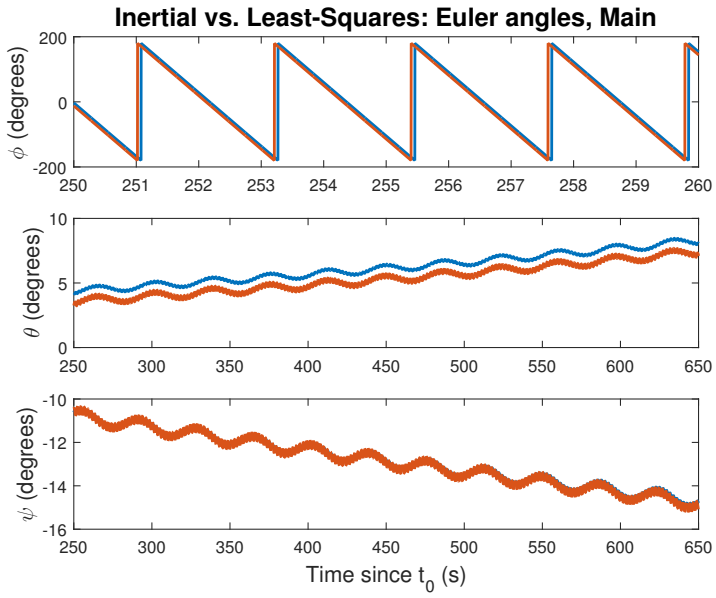

Fig. A.33: Main payload inertial attitude solution angle comparison

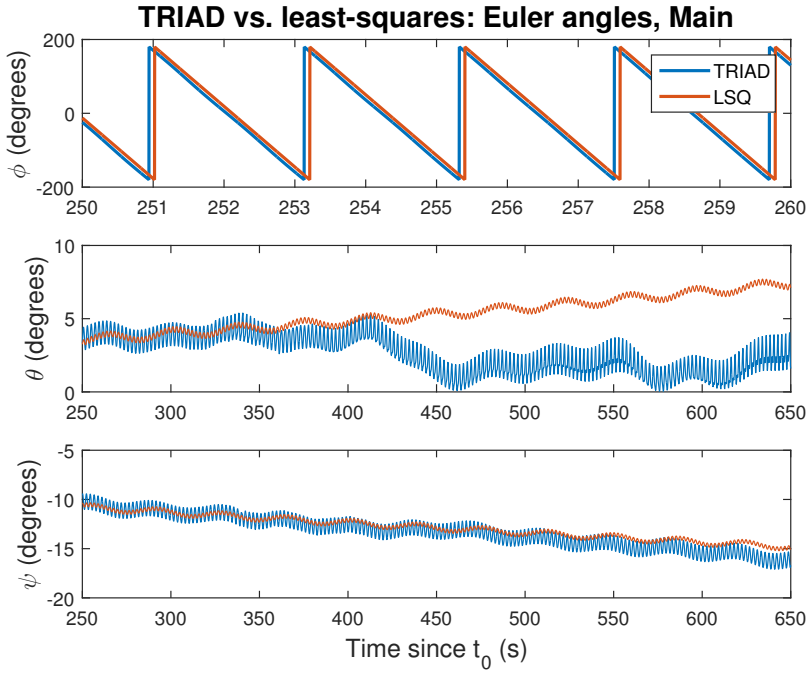

Fig. A.34: Main payload TRIAD method angle comparison

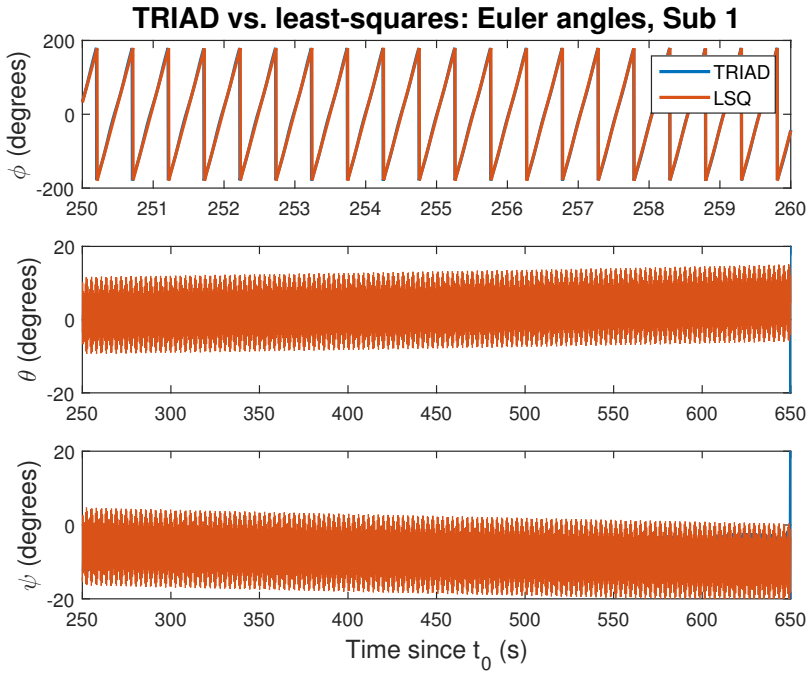

Fig. A.35: Subpayload #1 payload TRIAD method angle comparison

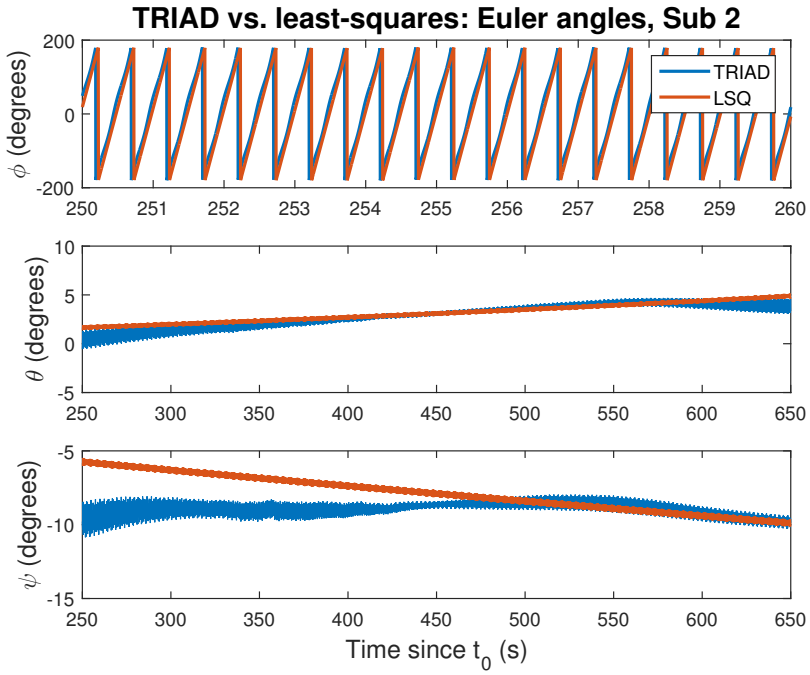

Fig. A.36: Subpayload #2 payload TRIAD method angle comparison

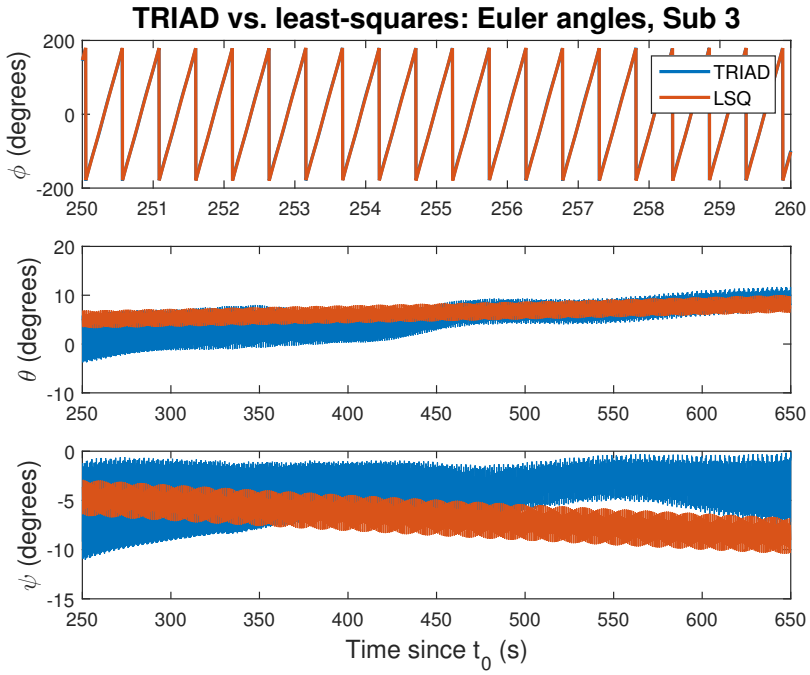

Fig. A.37: Subpayload #3 payload TRIAD method angle comparison

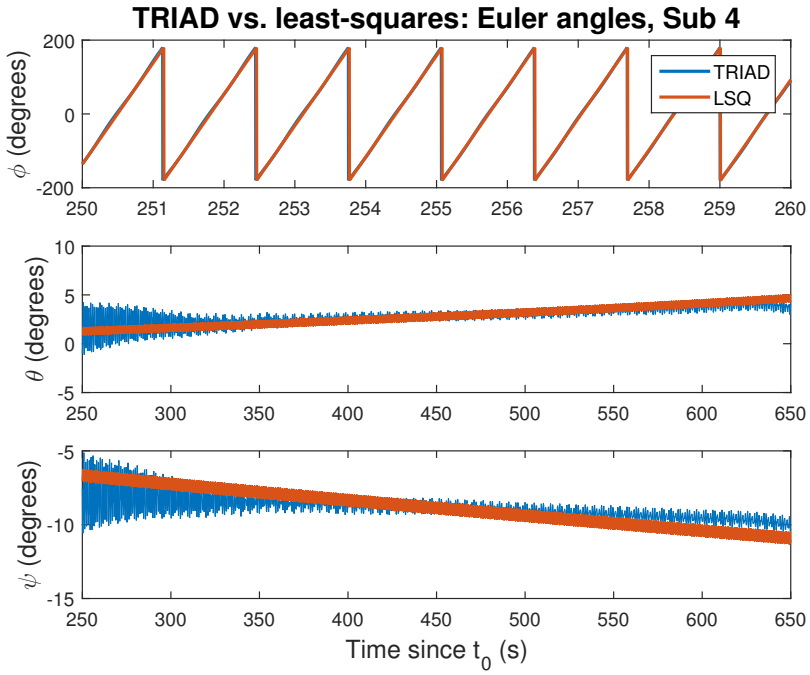

Fig. A.38: Subpayload #4 payload TRIAD method angle comparison

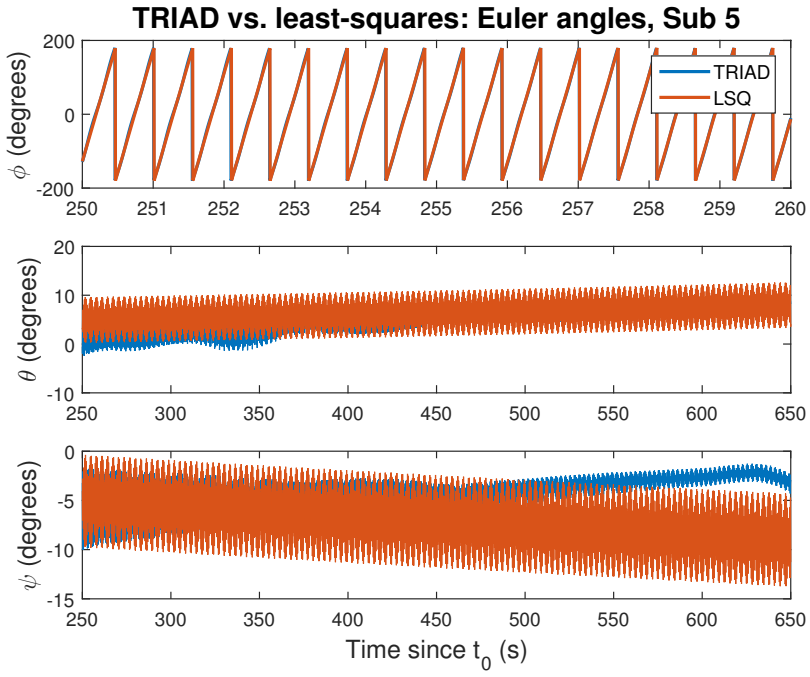

Fig. A.39: Subpayload #5 payload TRIAD method angle comparison

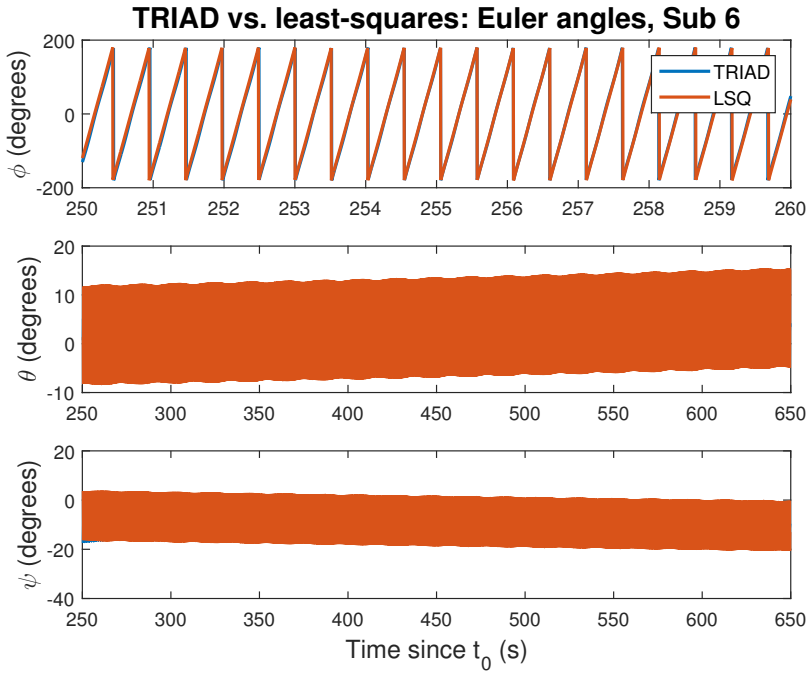

Fig. A.40: Subpayload #6 payload TRIAD method angle comparison

Euler Angle Differences

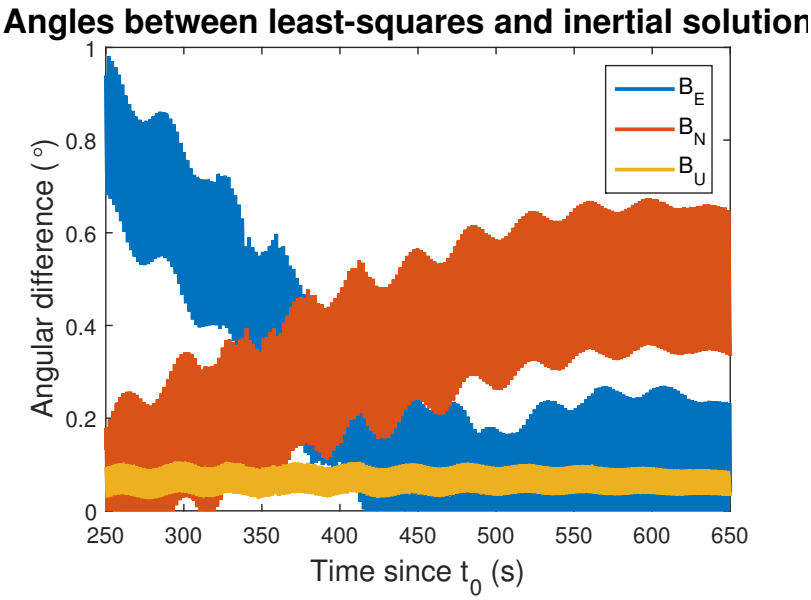

Fig. A.41: Main payload inertial attitude solution angle comparison

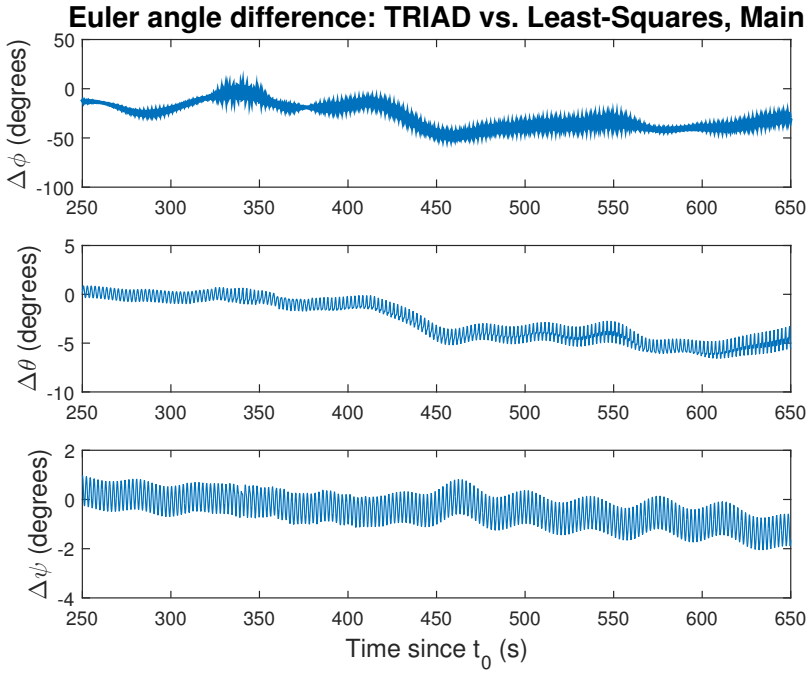

Fig. A.42: Main payload TRIAD method angle comparison

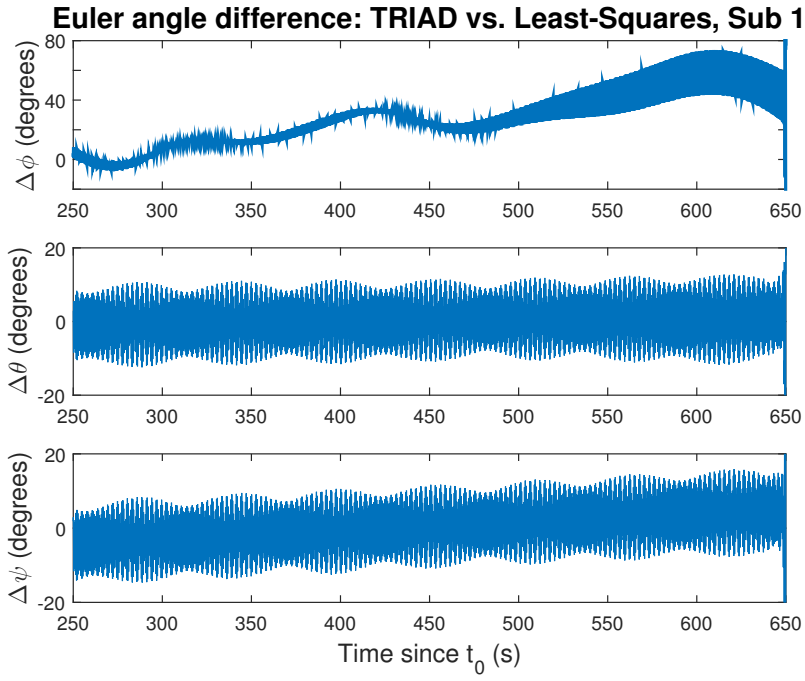

Fig. A.43: Subpayload #1 payload TRIAD method angle comparison

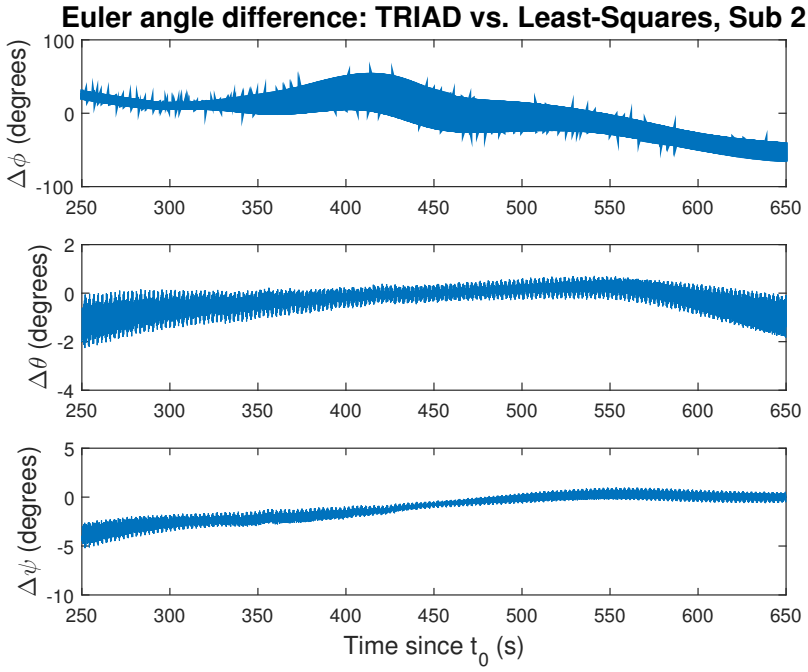

Fig. A.44: Subpayload #2 payload TRIAD method angle comparison

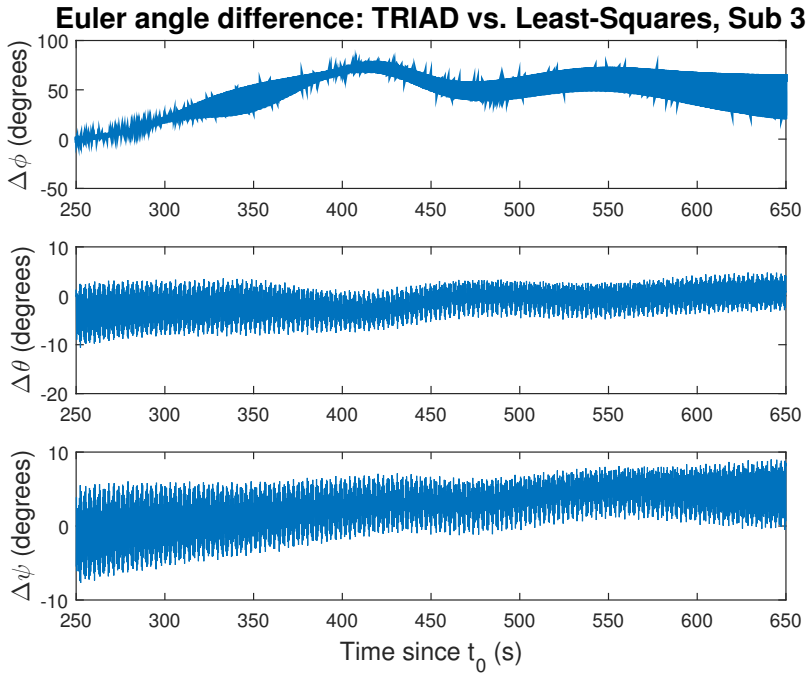

Fig. A.45: Subpayload #3 payload TRIAD method angle comparison

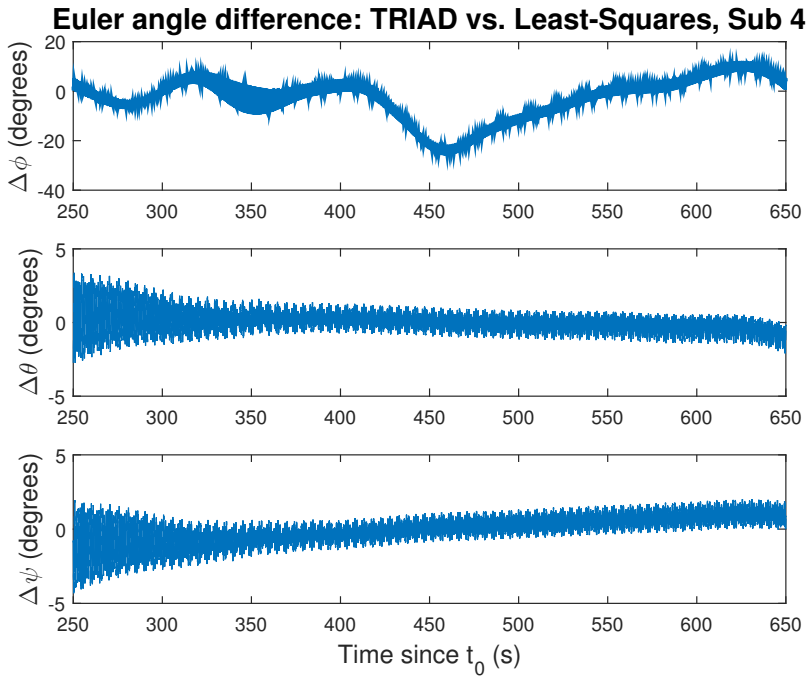

Fig. A.46: Subpayload #4 payload TRIAD method angle comparison

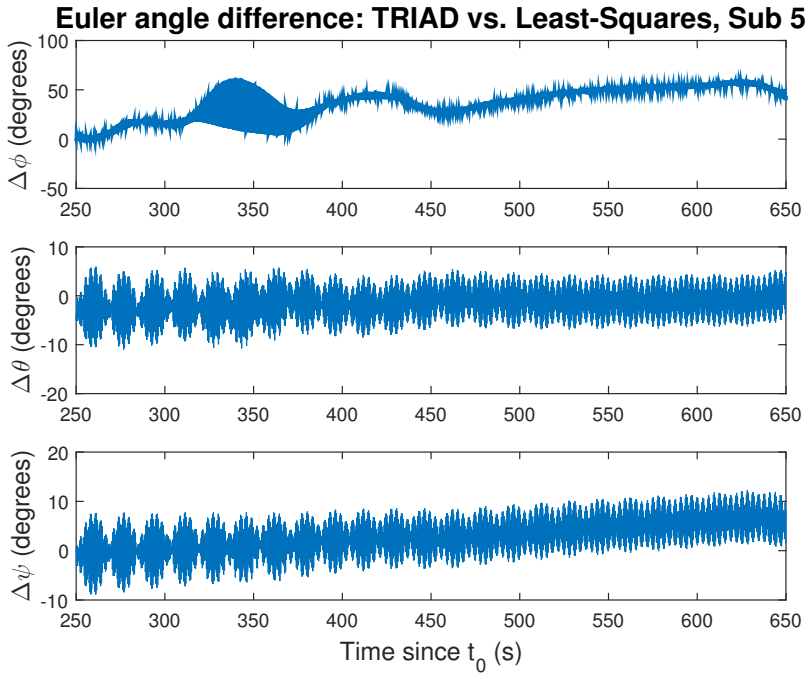

Fig. A.47: Subpayload #5 payload TRIAD method angle comparison

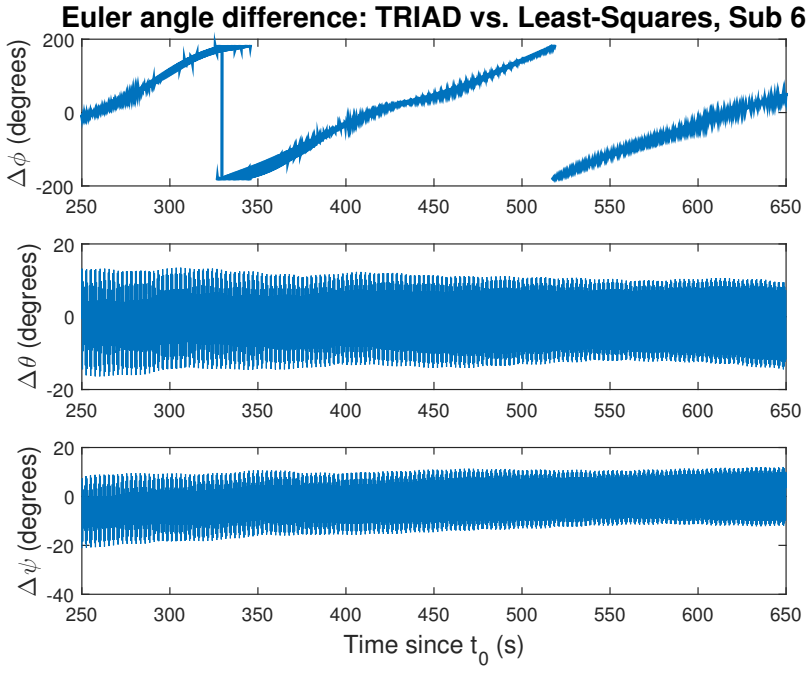

Fig. A.48: Subpayload #6 payload TRIAD method angle comparison

A.4 Spherical Angle Comparisons

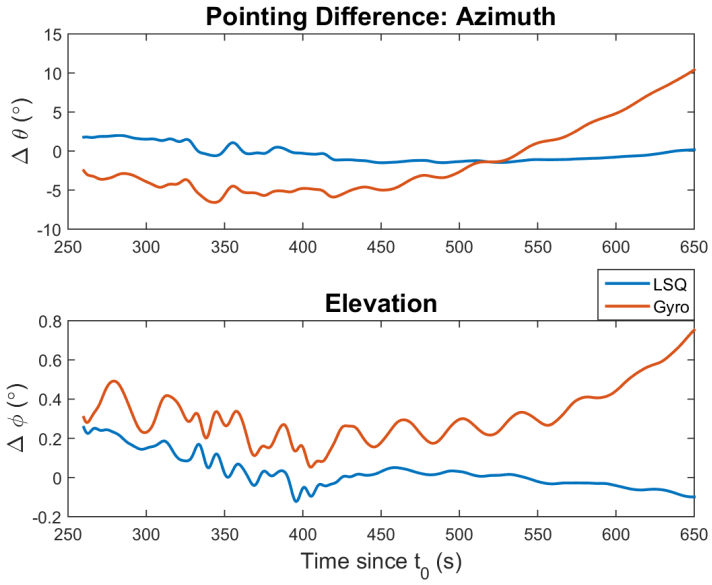

Fig. A.49: Main payload least-squares vs. inertial solution pointing error

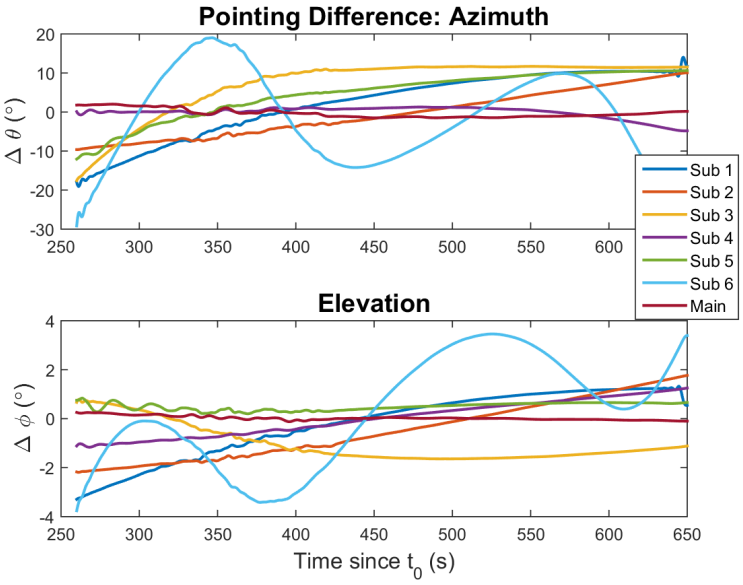

Fig. A.50: All payloads least-squares pointing error

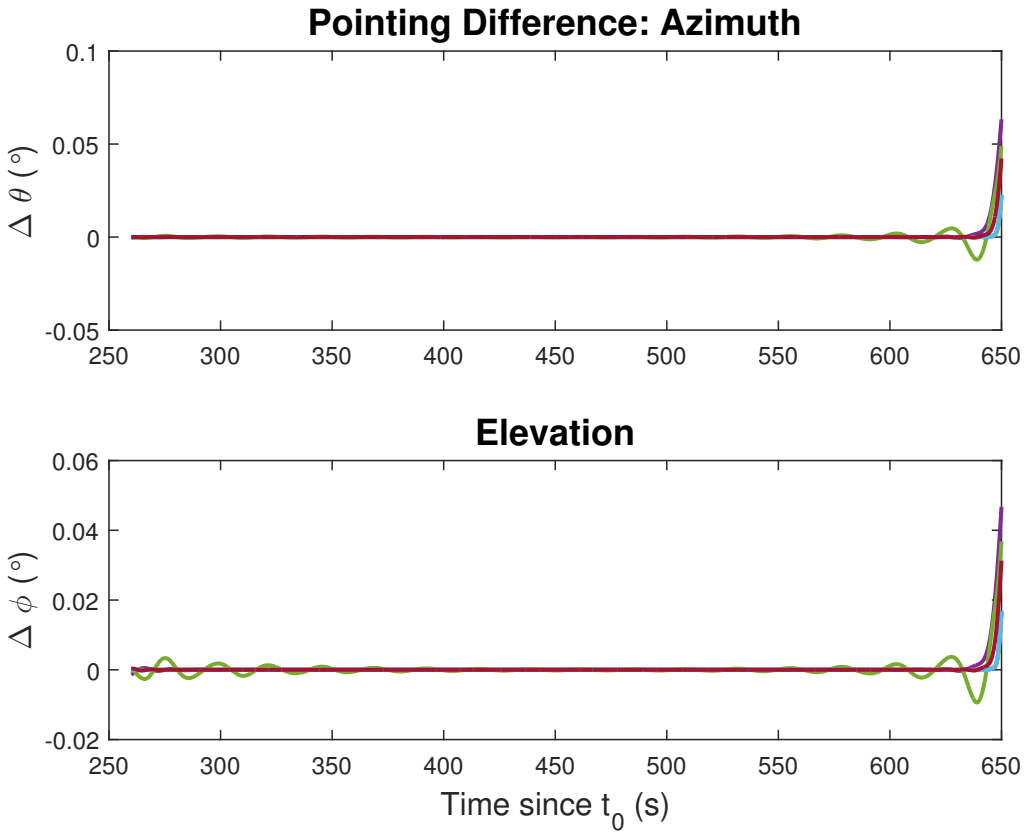

Fig. A.51: All payloads TRIAD pointing error

Appendix B

Calibrated Observations Measurements

B.1 Magnetic Field

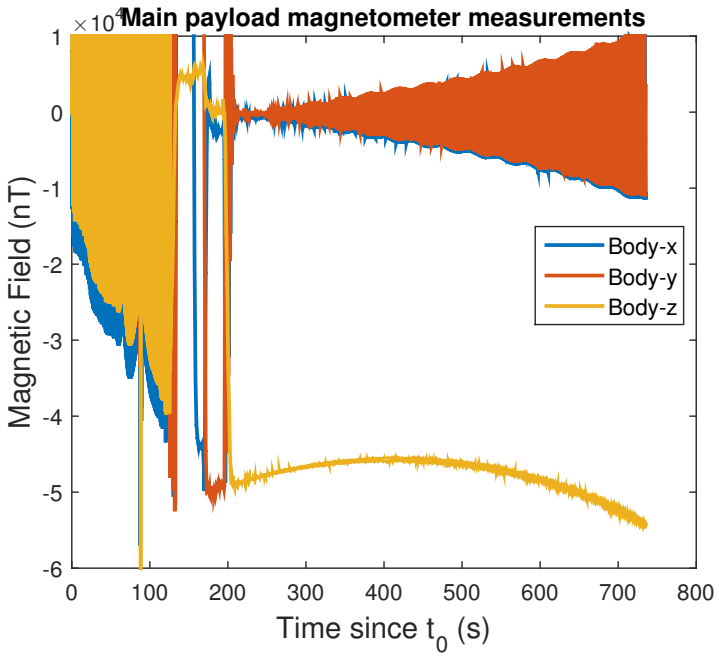

Fig. B.1: Main payload raw magnetometer observations

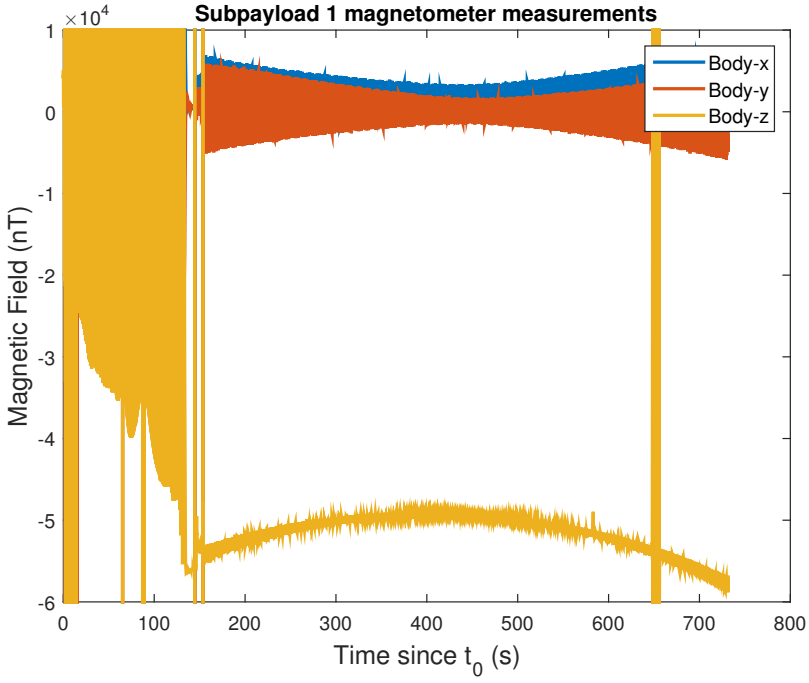

Fig. B.2: Subpayload #1 raw magnetometer observations

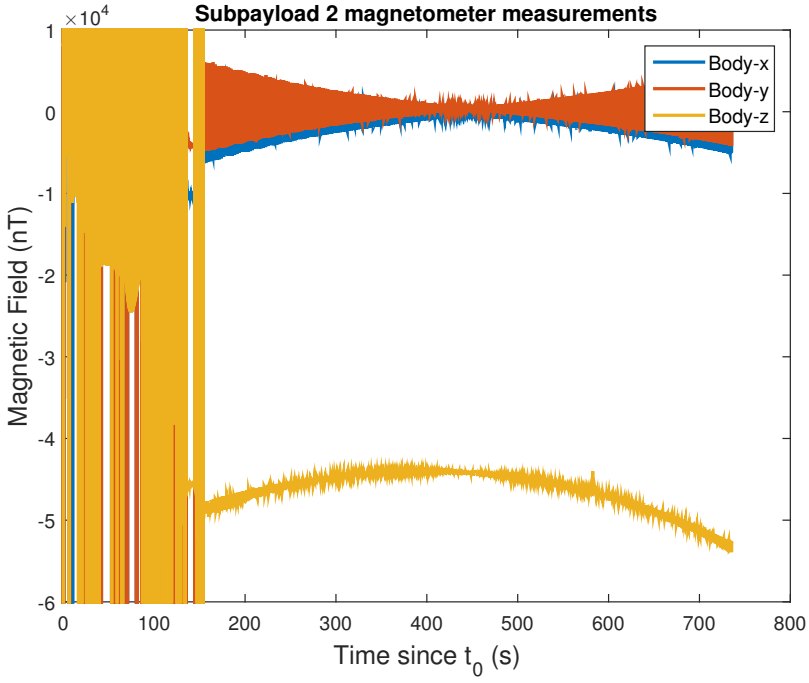

Fig. B.3: Subpayload #2 raw magnetometer observations

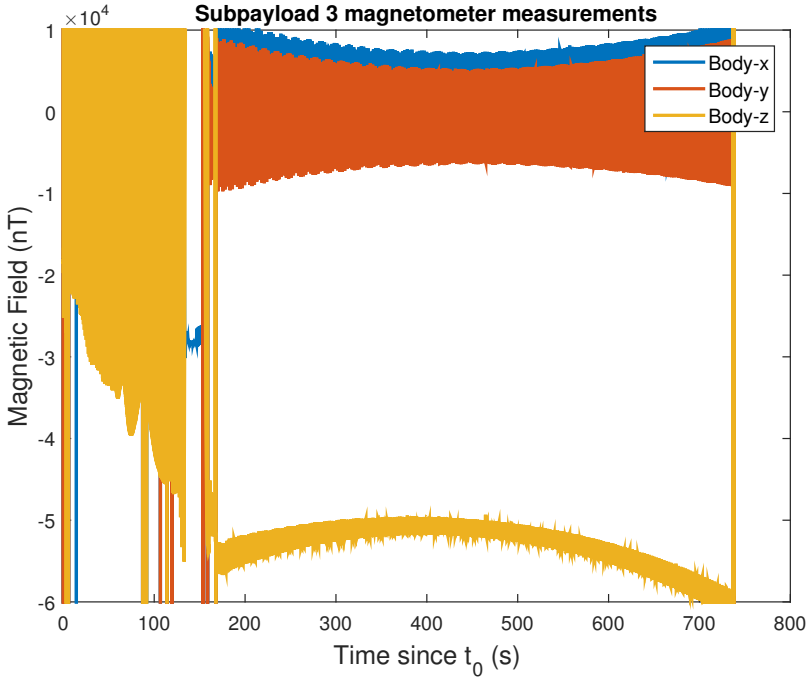

Fig. B.4: Subpayload #3 raw magnetometer observations

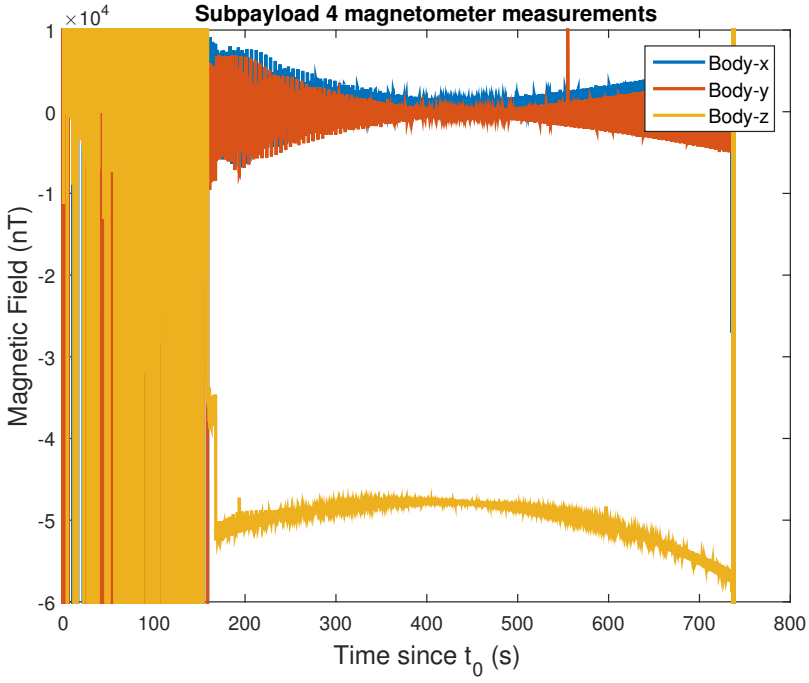

Fig. B.5: Subpayload #4 raw magnetometer observations

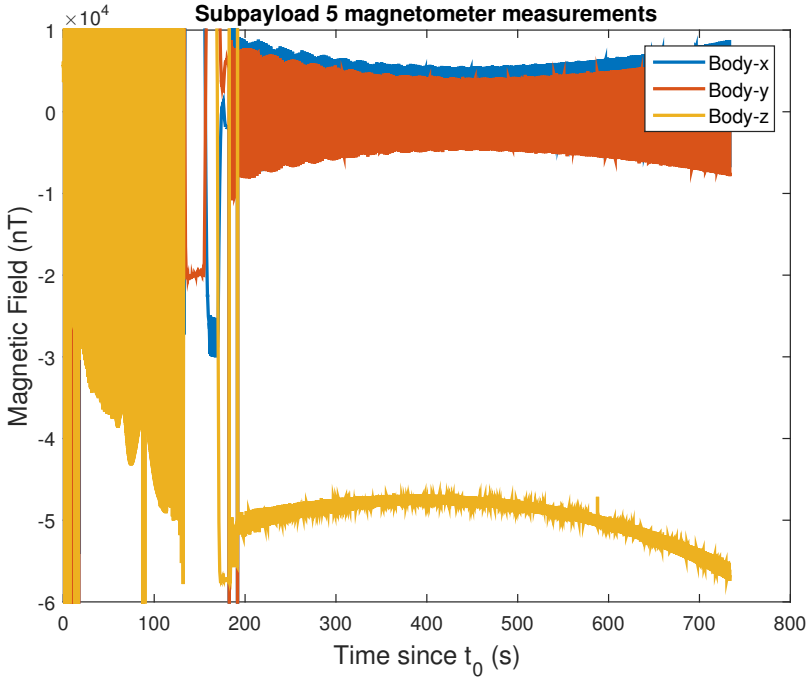

Fig. B.6: Subpayload #5 raw magnetometer observations

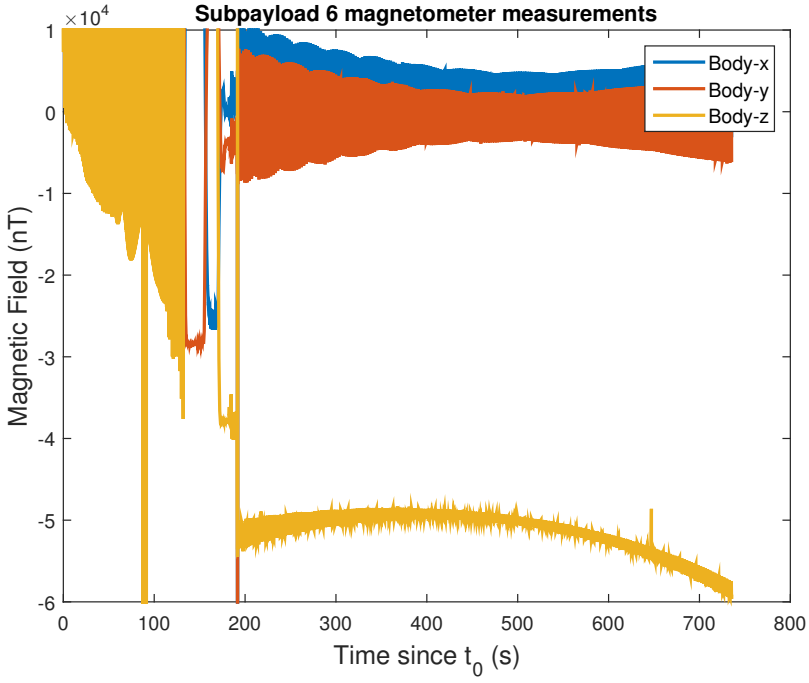

Fig. B.7: Subpayload #6 raw magnetometer observations

B.2 Electric Field

Note that the electric field plot for the main payload has units of volts per meter, while the subpayload plots have units of volts. This is due to lack of accurate knowledge of the deployed boom length on the subpayloads. If this becomes known, the electric field can be obtained by dividing the measurements shown by the length of the boom.

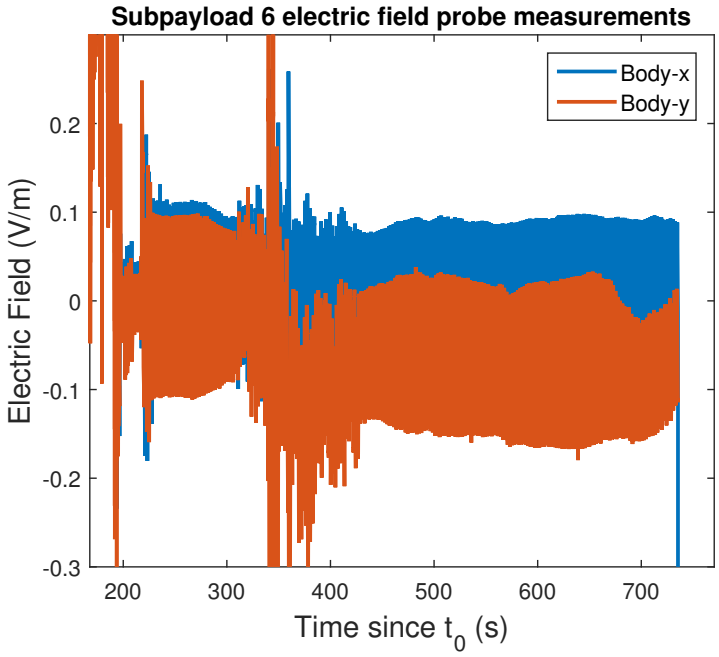

Fig. B.8: Main payload raw electric field probe observations

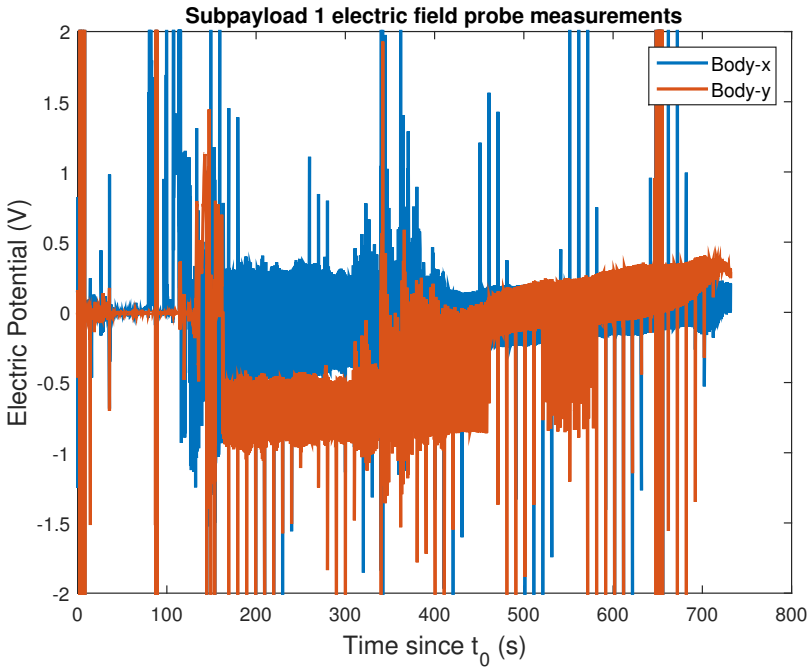

Fig. B.9: Subpayload #1 raw electric field probe observations

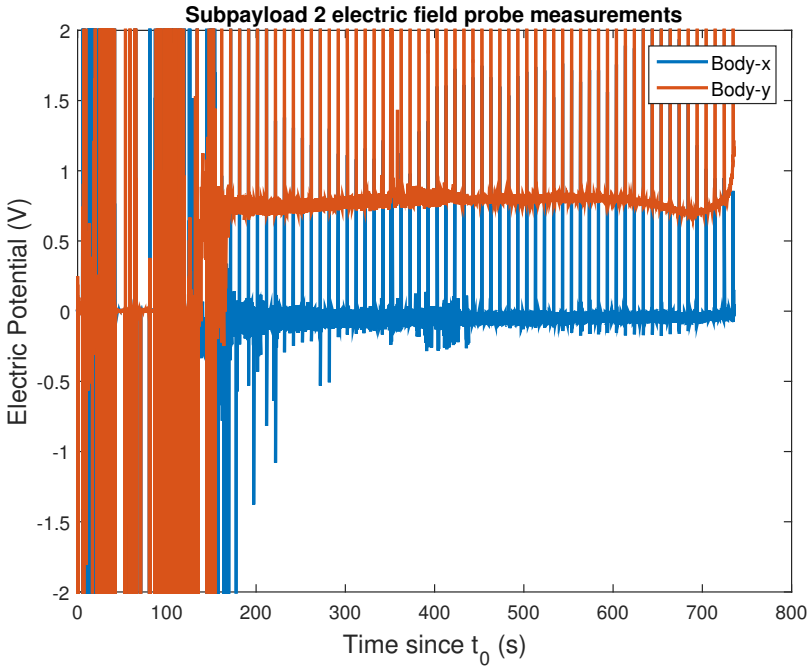

Fig. B.10: Subpayload #2 raw electric field probe observations

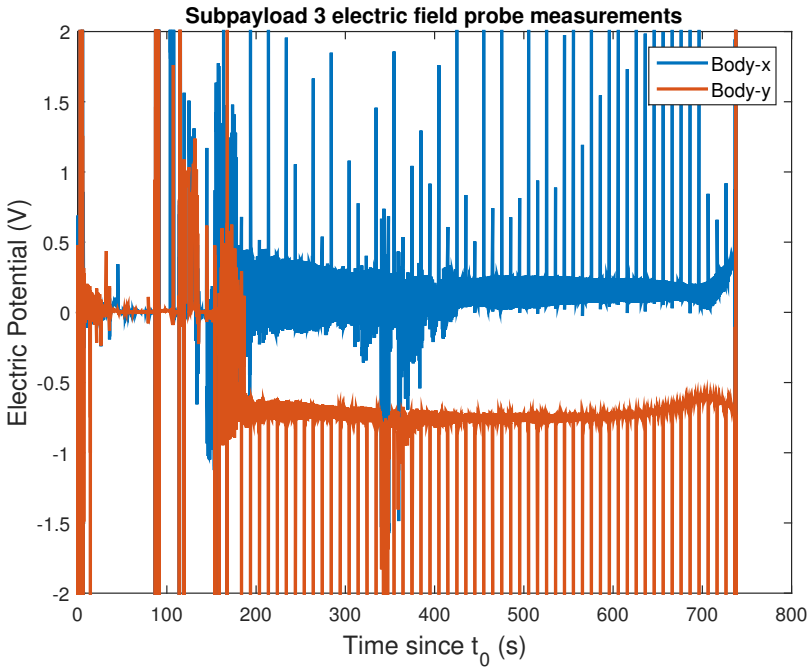

Fig. B.11: Subpayload #3 raw electric field probe observations

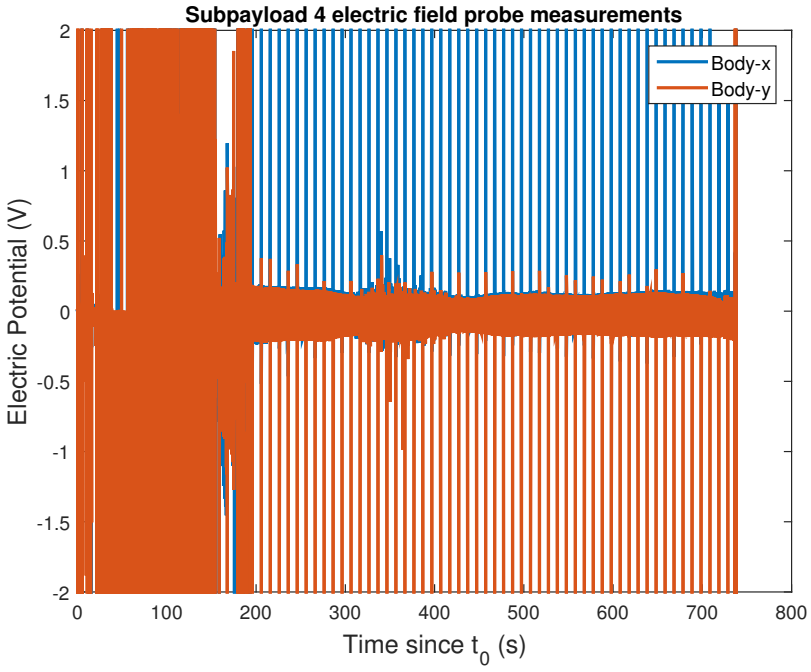

Fig. B.12: Subpayload #4 raw electric field probe observations

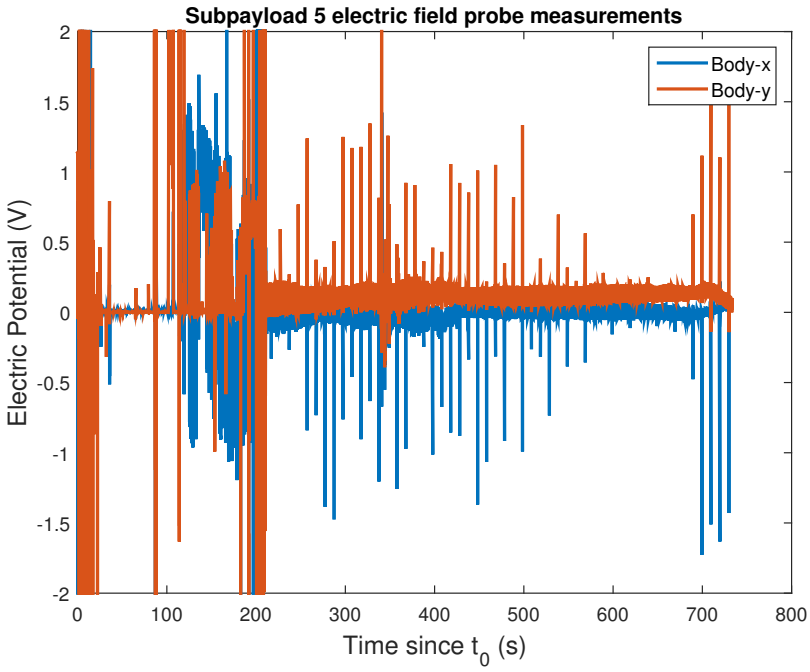

Fig. B.13: Subpayload #5 raw electric field probe observations

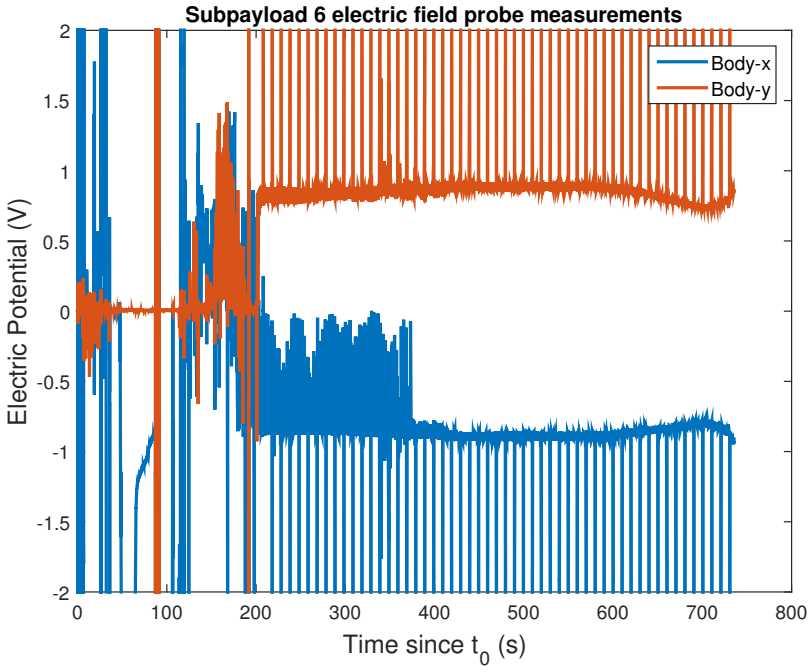

Fig. B.14: Subpayload #6 raw electric field probe observations

Appendix C

Parameter Estimates

C.1 Measured Inertias

Only two moments of inertia were reported for the main payload: about the spin axis, and about a perpendicular axis. Thus, I_{xx} and I_{yy} are assumed to be equal.

Parameter	Value	Units
I_{xx}	141.1	$\mathrm{kg\,m^2}$
I_{yy}	141.1	$\mathrm{kg\,m^2}$
I_{zz}	9.10	$\mathrm{kg\,m^2}$
I_{xy}	not measured	
I_{yz}	not measured	
I_{zx}	not measured	

Table C.1: Main payload measured inertia

Parameter	Value	Units
I_{xx}	0.011009	$\mathrm{kg\,m^2}$
I_{yy}	0.011023	$\mathrm{kg\,m^2}$
I_{zz}	0.012971	$\mathrm{kg\,m^2}$
I_{xy}	-0.000060	$\mathrm{kg\,m^2}$
I_{yz}	-0.000036	$\mathrm{kg\,m^2}$
I_{zx}	-0.000031	$\mathrm{kg\,m^2}$

Table C.2: Subpayload #1 measured inertia

C.2 Converged Least-Squares Parameter Estimates

Parameter	Value	Units
I_{xx}	0.010791	$\mathrm{kg\,m^2}$
I_{yy}	0.010663	$\mathrm{kg\,m^2}$
I_{zz}	0.012700	$\mathrm{kg\,m^2}$
I_{xy}	-0.000010	$\mathrm{kg\,m^2}$
I_{yz}	0.000134	$\mathrm{kg\,m^2}$
I_{zx}	0.000075	$\mathrm{kg\,m^2}$

Table C.3: Subpayload #2 measured inertia

Parameter	Value	Units
I_{xx}	0.010602	$\mathrm{kg\,m^2}$
I_{yy}	0.010528	$\mathrm{kg\,m^2}$
I_{zz}	0.012553	$\mathrm{kg\,m^2}$
I_{xy}	-0.000199	$\mathrm{kg\,m^2}$
I_{yz}	0.000055	$\mathrm{kg\,m^2}$
I_{zx}	0.000129	$\mathrm{kg\,m^2}$

Table C.4: Subpayload #3 measured inertia

Parameter	Value	Units
I_{xx}	0.010746	$\mathrm{kg\,m^2}$
I_{yy}	0.010662	$\mathrm{kg\,m^2}$
I_{zz}	0.012758	$\mathrm{kg\,m^2}$
I_{xy}	-0.000004	$\mathrm{kg\,m^2}$
I_{yz}	0.000089	$\mathrm{kg\,m^2}$
I_{zx}	0.000020	$\mathrm{kg\,m^2}$

Table C.5: Subpayload #4 measured inertia

Parameter	Value	Units
I_{xx}	0.010721	$\mathrm{kg\,m^2}$
I_{yy}	0.010662	$\mathrm{kg\,m^2}$
I_{zz}	0.012758	$\mathrm{kg\,m^2}$
I_{xy}	0.000016	$\mathrm{kg\,m^2}$
I_{yz}	0.000094	$\mathrm{kg\,m^2}$
I_{zx}	0.000019	$\mathrm{kg\,m^2}$

Table C.6: Subpayload #5 measured inertia

Parameter	Value	Units
I_{xx}	0.010497	$\mathrm{kg\,m^2}$
I_{yy}	0.010514	$\mathrm{kg\,m^2}$
I_{zz}	0.012625	$\mathrm{kg\,m^2}$
I_{xy}	0.000004	$\mathrm{kg\,m^2}$
I_{yz}	-0.000046	$\mathrm{kg\,m^2}$
I_{zx}	-0.000027	$\mathrm{kg\,m^2}$

Table C.7: Subpayload #6 measured inertia

Parameter	Value	Units
I_{xx}	138.408	$\mathrm{kg\,m^2}$
I_{yy}	140.019	$\mathrm{kg\,m^2}$
I_{zz}	8.293	$\mathrm{kg\,m^2}$
I_{xy}	0.067	$\mathrm{kg\,m^2}$
I_{yz}	0.359	$\mathrm{kg\,m^2}$
I_{zx}	0.277	$\mathrm{kg\,m^2}$
ψ	-0.524	rad
θ	-0.974	rad
ϕ	1.068	rad
$\dot{\psi}$	-0.007	$\mathrm{rad\,s^{-1}}$
$\dot{\theta}$	-0.008	$\mathrm{rad\,s^{-1}}$
$\dot{\phi}$	2.868	$\mathrm{rad\,s^{-1}}$
c_x	318.987	nT
c_y	381.933	nT
c_z	-90.332	nT

Table C.8: Main payload estimated parameters

Parameter	Value	Units
I_{xx}	0.011107	$\mathrm{kg\,m^2}$
I_{yy}	0.010256	$\mathrm{kg\,m^2}$
I_{zz}	0.012613	$\mathrm{kg\,m^2}$
I_{xy}	0.000231	$\mathrm{kg\,m^2}$
I_{yz}	0.000158	$\mathrm{kg\,m^2}$
I_{zx}	0.000219	$\mathrm{kg\,m^2}$
ψ	-0.973	rad
θ	0.938	rad
ϕ	1.834	rad
$\dot{\psi}$	1.855	$\mathrm{rad\,s^{-1}}$
$\dot{\theta}$	-1.124	$\mathrm{rad\,s^{-1}}$
$\dot{\phi}$	-12.245	$\mathrm{rad\,s^{-1}}$
c_x	-5657	nT
c_y	1406	nT
c_z	-48	nT

Table C.9: Subpayload #1 estimated parameters

Parameter	Value	Units
I_{xx}	0.011353	$\mathrm{kg\,m^2}$
I_{yy}	0.009869	$\mathrm{kg\,m^2}$
I_{zz}	0.012123	$\mathrm{kg\,m^2}$
I_{xy}	-0.000016	$\mathrm{kg\,m^2}$
I_{yz}	0.000001	$\mathrm{kg\,m^2}$
I_{zx}	0.000003	$\mathrm{kg\,m^2}$
ψ	0.531	rad
θ	2.017	rad
ϕ	0.060	rad
$\dot{\psi}$	0.053	$\mathrm{rad\,s^{-1}}$
$\dot{\theta}$	-0.004	$\mathrm{rad\,s^{-1}}$
$\dot{\phi}$	-12.520	$\mathrm{rad\,s^{-1}}$
c_x	-172	nT
c_y	62	nT
c_z	-67	nT

Table C.10: Subpayload #2 estimated parameters

Parameter	Value	Units
I_{xx}	0.010585	$\mathrm{kg\,m^2}$
I_{yy}	0.010568	$\mathrm{kg\,m^2}$
I_{zz}	0.016091	$\mathrm{kg\,m^2}$
I_{xy}	-0.000023	$\mathrm{kg\,m^2}$
I_{yz}	0.000102	$\mathrm{kg\,m^2}$
I_{zx}	0.000086	$\mathrm{kg\,m^2}$
ψ	0.583	rad
θ	0.263	rad
ϕ	-2.098	rad
$\dot{\psi}$	-0.051	$\mathrm{rad\,s^{-1}}$
$\dot{\theta}$	-0.169	$\mathrm{rad\,s^{-1}}$
$\dot{\phi}$	-12.131	$\mathrm{rad\,s^{-1}}$
c_x	1108	nT
c_y	1300	nT
c_z	-460	nT

Table C.11: Subpayload #3 estimated parameters

Parameter	Value	Units
I_{xx}	0.011062	$\mathrm{kg\,m^2}$
I_{yy}	0.011460	$\mathrm{kg\,m^2}$
I_{zz}	0.698217	$\mathrm{kg\,m^2}$
I_{xy}	-0.000277	$\mathrm{kg\,m^2}$
I_{yz}	-0.000973	$\mathrm{kg\,m^2}$
I_{zx}	-0.000603	$\mathrm{kg\,m^2}$
ψ	1.215	rad
θ	-3.103	rad
ϕ	1.243	rad
$\dot{\psi}$	1.346	$\mathrm{rad\,s^{-1}}$
$\dot{\theta}$	1.195	$\mathrm{rad\,s^{-1}}$
$\dot{\phi}$	-4.790	$\mathrm{rad\,s^{-1}}$
c_x	-182	nT
c_y	-266	nT
c_z	34	nT

Table C.12: Subpayload #4 estimated parameters

Parameter	Value	Units
I_{xx}	0.010292	$\mathrm{kg\,m^2}$
I_{yy}	0.010223	$\mathrm{kg\,m^2}$
I_{zz}	0.012044	$\mathrm{kg\,m^2}$
I_{xy}	0.000047	$\mathrm{kg\,m^2}$
I_{yz}	-0.000040	$\mathrm{kg\,m^2}$
I_{zx}	-0.000016	$\mathrm{kg\,m^2}$
ψ	2.815	rad
θ	-0.245	rad
ϕ	-3.006	rad
$\dot{\psi}$	-0.061	$\mathrm{rad\,s^{-1}}$
$\dot{\theta}$	-0.500	$\mathrm{rad\,s^{-1}}$
$\dot{\phi}$	-11.502	$\mathrm{rad\,s^{-1}}$
c_x	-707	nT
c_y	-1325	nT
c_z	108	nT

Table C.13: Subpayload #5 estimated parameters

Parameter	Value	Units
I_{xx}	0.009720	$\mathrm{kg\,m^2}$
I_{yy}	0.010580	$\mathrm{kg\,m^2}$
I_{zz}	0.010932	$\mathrm{kg\,m^2}$
I_{xy}	0.000671	$\mathrm{kg\,m^2}$
I_{yz}	0.000140	$\mathrm{kg\,m^2}$
I_{zx}	-0.000255	$\mathrm{kg\,m^2}$
ψ	0.244	rad
θ	2.971	rad
ϕ	0.771	rad
$\dot{\psi}$	1.784	$\mathrm{rad\,s^{-1}}$
$\dot{\theta}$	-1.122	$\mathrm{rad\,s^{-1}}$
$\dot{\phi}$	-12.033	$\mathrm{rad\,s^{-1}}$
c_x	-6926	nT
c_y	4354	nT
c_z	-932	nT

Table C.14: Subpayload #6 estimated parameters